

**Universidade de Lisboa**

Faculdade de Ciências

Departamento de Física



**Magnetic Resonance Elastography: Design and  
Implementation as a Clinical Tool**

Joana Rita Alves Loureiro

Dissertação

Mestrado Integrado em Engenharia Biomédica e Biofísica  
Perfil de Radiações em Diagnóstico e Terapia

2012



**Universidade de Lisboa**

Faculdade de Ciências

Departamento de Física



# **Magnetic Resonance Elastography: Design and Implementation as a Clinical Tool**

Joana Rita Alves Loureiro

Dissertação de Mestrado Integrado orientada pelo Professor Alexandre Andrade e pelo  
Professor Marius Mada

Dissertação

Mestrado Integrado em Engenharia Biomédica e Biofísica  
Perfil de Radiações em Diagnóstico e Terapia

2012







# Acknowledgements

First I would like to thank my supervisor Dr. Marius Mada, from WBIC for all the support, suggestions, and guidance during the ten months of internship. He has been an invaluable mentor. I learnt a lot working with him, not only about MR Elastography itself but also about the research process, from experiment design to the presentation of results in an appropriate manner. I have also to thank him for all the time that he spent helping me in the scanner and for his patience and precious advices during all phases of the project; it was definitely a huge source of motivation. I thank my internal supervisor Dr. Alexandre Andrade for his availability and for all the suggestions and help, for his support during all stages of the project and for his guidance and encouragement.

I thank Dr. Eduardo Ducla-Soares for his enthusiasm and guidance during the year of the project and for always supporting my ideas and believing in me.

I am deeply grateful to the MRE Edinburgh group for all the support, ideas, suggestions and availability; especially to Dr. Lauren Seal for her support, and guidance, giving always precious insights to carry on with my work in ABAQUS and for her encouragement; to Paul Kennedy and Evelyn Buchner for sharing their experience, critical ideas and enthusiasm with our group.

I would like to express my gratitude to the Charité group, Berlin, for designing and building the hardware set-up, for answering all my questions about the hardware principles and wave motion and for giving suggestions and advices to improve the hardware and our results.

I thank Dr. Guy Williams for providing me the opportunity and experience to make this thesis at the Wolfson Brain Imaging Centre at the Addenbrooke's Hospital in Cambridge and for his suggestions and availability.

This thesis would never been possible without the love and encouragement of my family and friends. Their confidence and support made me went through all the difficulties during all the process and kept me motivated to do always the best I could. I am especially grateful to Edgar Murphy and to my parents Conceição and Jorge for their love and patience during the internship.

I am grateful to my house mates and friends Rafael and Catarina for their suggestions and support.

Thanks are due to all the WBIC investigators to make me feel welcome for the institute and for providing a good environment during the ten months of internship.

Finally, I am thankful to LLP/Erasmus Programme for financial support of the ten months of internship in Cambridge.





# Resumo

A viscoelasticidade é uma propriedade física dos tecidos, que se altera quando estes sofrem modificações. Desta forma, esta característica é uma propriedade importante no diagnóstico de doenças que alteram as capacidades elásticas dos tecidos. A palpação manual é uma técnica milenar que é geralmente utilizada para identificar lesões, como por exemplo nódulos e quistos. No entanto, esta técnica depende fortemente da experiência do médico e da região onde se encontra a lesão. Deste modo, na última década tem havido um esforço acrescido para serem desenvolvidas novas técnicas de imagem médica que forneçam informação sobre a elasticidade dos tecidos de uma forma quantitativa. Surge assim a elastografia. Esta técnica é baseada na detecção da deformação do tecido provocada por stresses internos ou externos e tem sido fortemente utilizada, combinada com outras técnicas como a ultrassonografia e a ressonância magnética, no diagnóstico de doenças que influenciam as propriedades elásticas dos tecidos. Inicialmente, a técnica de elastografia começou por ser combinada apenas com ultrassons. Porém, esta técnica apresenta algumas desvantagens devido à sua baixa resolução espacial e devido a apresentar resultados apenas na direcção de propagação da onda. Estas limitações têm servido de incentivo à exploração de técnicas alternativas, como a Elastografia por Ressonância Magnética (MRE, do inglês “Magnetic Resonance Elastography”) e à sua aplicação ao diagnóstico de doenças como a cirrose hepática ou a detecção de tumores. A MRE é uma técnica não invasiva, capaz de detectar a propagação de ondas em tecidos sujeitos a estimulação mecânica, permitindo assim o cálculo do módulo de elasticidade dos tecidos *in vivo*. Nesta nova modalidade, é usado um sistema convencional de ressonância magnética, em simultâneo com um sistema de actuação que provoca vibrações no tecido de interesse. De modo a que seja possível medir o deslocamento sofrido pelos *spins* em movimento devido à vibração induzida, é adicionado um gradiente sensível ao movimento (MEG, do inglês “Motion Encoding Gradient”) a uma simples sequência *spin-echo EPI*. Por fim, esta técnica usa um algoritmo de inversão que se baseia nos deslocamentos medidos, para calcular os mapas de elasticidade do tecido de interesse. O desenvolvimento de equipamentos para MRE representa um desafio devido às inúmeras considerações e limitações que é necessário ter em conta. Por exemplo, o *hardware* tem de possuir um design que permita uma excitação mecânica dos tecidos, adequada, dentro do campo magnético do equipamento de ressonância magnética e tem

de ser confortável para o sujeito que está a ser submetido ao exame. Por outro lado, a optimização dos procedimentos de análise de dados é também uma questão crucial. É no âmbito do desenvolvimento de novas técnicas, métodos e equipamentos de MRE que surge o presente projecto.

Este projecto foi desenvolvido no Wolfson Brain Imaging Center (WBIC), no Hospital de Addenbrooke's, em Cambridge, e teve como objectivos o melhoramento de vários aspectos relacionados com o equipamento e os métodos de aquisição de imagens de um sistema de MRE de aquisição recente no WBIC. Estes melhoramentos traduziram-se em alterações ao nível do *hardware* e do *software*.

Ao longo dos anos têm sido desenvolvidos vários tipos de actuadores que permitem a excitação dos tecidos. Entre os mais usados estão os actuadores piezoeléctricos, os actuadores pneumáticos e os actuadores electromagnéticos. O actuador piezoeléctrico, produzido pelo grupo do Charité do Instituto de Informática Médica, da Universidade de Berlim, e adquirido pelo WBIC possui dois tipos de *set-up*; um para a excitação do cérebro e um para a excitação do fígado. Com vista a ter uma perspectiva geral das vantagens e desvantagens dos actuadores piezoeléctricos e dos actuadores pneumáticos, as características de cada um destes, foram criteriosamente estudadas, o que permitiu melhorar e optimizar o actuador piezoeléctrico. Assim, algumas das alterações que foram efectuadas neste sistema foram: alteração da *head cradle* (*set-up* do cérebro) para aumentar o conforto do paciente e a eficiência, e a alteração do controlo remoto do amplificador e gerador de ondas, de modo a não ser necessário o deslocamento do técnico na modificação dos parâmetros de MRE.

De modo a poder comparar os dois tipos de actuação nos tecidos, foi também um dos objectivos deste projecto desenvolver um sistema pneumático e comparar a sua performance com o equipamento piezoeléctrico comercial desenvolvido pela Mayo-Clinic, Mayo Foundation for Medical Education and Research, e com o actuador piezoeléctrico do WBIC. Com esse fim, foi desenvolvido um actuador pneumático de raiz, a custo reduzido, e o seu desempenho foi avaliado.

Para comparar os dois tipos de actuação, efectuaram-se testes de deflexão de movimento num fantoma de gelatina, através do uso de um acelerómetro comercial, para várias frequências de excitação. Três sistemas diferentes foram testados: o piezoeléctrico e dois sistemas pneumáticos: entre eles o actuador desenvolvido no WBIC e o actuador

pneumático comercial, desenvolvido na clínica Mayo. A utilização de dois tipos de actuadores pneumáticos permitiu testar se a propagação da onda nos tecidos depende somente do tipo de actuação utilizada (se é através de um actuador pneumático ou piezoeléctrico) ou se está também relacionada com características específicas de *hardware* de cada actuador. Com este estudo concluiu-se que, tal como seria esperado, o *set-up* desenhado para o fígado, do actuador piezoeléctrico, induziu um maior deslocamento nos tecidos do que qualquer um dos outros actuadores, quer para baixas frequências (20Hz), quer para altas frequências (80-100 Hz). No entanto, o *set-up* pneumático da Clínica Mayo induziu um maior deslocamento no fantoma do que o actuador piezoeléctrico para frequências entre os 30 e os 50 Hz. Estes resultados comprovaram a consistência e reprodutibilidade do actuador piezoeléctrico, bem como a sua precisão e controlo para altas frequências. O actuador pneumático desenvolvido no WBIC provou ter pouca potência e induziu um pequeno deslocamento no material comparativamente com os outros actuadores. Contudo, este sistema é de fácil aplicação e introdução no ambiente e na sala de Ressonância Magnética, a custo reduzido. O módulo de elasticidade para um fantoma de gelatina, para o fígado e para o cérebro, foi também calculado através de MRE, quer com o actuador piezoeléctrico quer com o actuador pneumático desenvolvido no WBIC. Concluiu-se que, apesar das desvantagens do actuador pneumático desenvolvido no WBIC, obtiveram-se valores de elasticidade, com este actuador, consistentes e na mesma ordem de grandeza que os valores obtidos com o actuador piezoeléctrico.

A literatura de MRE apresenta contradições em diversos estudos, sendo indicados diferentes valores do módulo da elasticidade para o mesmo tecido. Esta incongruência é em parte devida à grande variedade de parâmetros que influencia os resultados de MRE e às condicionantes e limitações do *hardware*. Desta forma, torna-se essencial a utilização de métodos de validação desta nova modalidade de diagnóstico médico. Neste projecto, foram utilizados modelos de elementos finitos (FEM, do inglês “Finite Element Modelling”) e foi efectuada uma análise dinâmica da elasticidade (DST, do inglês “Dynamic Shear Testing”) de modo a validar os resultados obtidos experimentalmente pela MRE. Identificaram-se dois tipos de parâmetros que influenciam os resultados de MRE: os parâmetros puramente computacionais e os parâmetros experimentais.

A validação através de FEMs foi dividida em dois estudos principais: um primeiro estudo que examinou a influência dos parâmetros puramente computacionais e um segundo

estudo que examinou a influência dos parâmetros experimentais nos resultados. Em ambos os estudos, desenvolveram-se modelos simétricos relativamente a um eixo e rectangulares prismáticos que representam uma secção semi-axial de um fantoma de gelatina cilíndrico. A face inferior dos modelos foi restringida na direcção  $y$  e aplicou-se uma análise dinâmica transiente.

O primeiro estudo de FEMs efectuado teve como principal objectivo estudar a influência dos parâmetros puramente computacionais e tentar eliminar a sua influência nos resultados obtidos pelos FEMs. Neste estudo, as condições de fronteira (BC: do inglês “Boundary Conditions”) e a densidade da malha de elementos finitos foram alterados. Para estudar as BC, foram criados dois modelos com dimensões diferentes (100x10 mm e 100x20 mm) e concluiu-se que o modelo com espessura de 20 mm apresentou resultados mais próximos da curva teórica do comprimento de onda em função do módulo de Young. Para estudar a densidade da malha de elementos finitos, foram também criados dois modelos com elementos de dimensões diferentes (1x1 mm e 2x2 mm). As imagens de propagação da onda, ao longo da direcção  $x$  do modelo, e o respectivo perfil de deslocamento ao longo da mesma direcção da face superior do fantoma, revelaram que o modelo com elementos de dimensões 2x2mm não foi capaz de detectar a propagação da onda, ao contrário do que aconteceu com o modelo com elementos de dimensões 1x1 mm. Este estudo comprovou a importância da escolha criteriosa quer das condições de fronteira, quer da densidade da malha na criação de modelos finitos, e mostrou que os resultados sofrem modificações importantes aquando da modificação destes dois parâmetros. As conclusões obtidas neste estudo foram aplicadas no segundo estudo com FEMs de modo a eliminar a influência dos parâmetros computacionais.

O segundo estudo de FEMs teve como principal objectivo estudar a influência dos parâmetros experimentais, como por exemplo a densidade do material. Para tal, foram criados modelos com diferentes densidades e módulos de Young. Com este estudo, concluiu-se que a propagação da onda nos tecidos (modelo de FEMs) e o correspondente comprimento de onda variam bastante consoante a densidade dos tecidos. Constatou-se que os resultados obtidos para o modelo com densidade de  $1\text{kg/mm}^3$  foram os que mais se aproximaram da curva teórica. Por fim, concluiu-se que a densidade dos tecidos altera grandemente os resultados obtidos.

A validação através da DST permitiu comparar os resultados obtidos através de MRE com os resultados obtidos através desta técnica de validação, para amostras de três

fantomas de gelatina com diferentes concentrações. A análise dinâmica da elasticidade já provou ser, em estudos anteriores, uma técnica capaz de medir o módulo de elasticidade dos tecidos de forma precisa e viável, apesar das suas limitações na vibração a elevadas frequências (frequências em que a MRE opera). Com ambas as técnicas (MRE e DST), obtiveram-se resultados do módulo da elasticidade com a mesma ordem de magnitude. No entanto, com MRE os valores obtidos foram significativamente mais elevados para os três fantomas de concentração de gel diferente. Este resultado deve-se à dependência de ambas as técnicas, relativamente a factores que dificilmente podem ser controlados, como sejam: a espessura das amostras e a sua não uniformidade no caso da DST; e, no caso da MRE, todos os parâmetros que foram descritos e avaliados ao longo deste projecto como as limitações do *hardware* e possíveis erros induzidos pelo algoritmo de inversão.

Em suma, é importante realçar a importância que este projecto teve no desenvolvimento da técnica de MRE no WBIC. É ainda de salientar que este trabalho representou um passo adicional no caminho da aprovação do projecto de MRE na prática clínica, pelo comité ético do hospital de Addenbrooke's, e uma contribuição para a aceitação desta técnica como método de diagnóstico em meio clínico.

**Palavras-chave:** Elastografia por Ressonância Magnética, *Hardware*, Método de Elementos Finitos, Análise Dinâmica de Elasticidade.

---



# Abstract

Palpation has been used for centuries to detect changes in elasticity in several body regions. However, this technique is clearly limited to regions that are accessible to physician's hands. Therefore, over the last decades there has been an attempt to develop methods for imaging tissue stiffness that are not hindered by this limitation, such as Magnetic Resonance Elastography (MRE). MRE is a non-invasive technique that can directly measure propagating strain waves due to harmonic mechanical excitation, hence allowing for the *in vivo* computation of the shear modulus of tissues.

One main issue with MRE is the design of an actuation system that enables adequate mechanical excitation within the magnetic field of the magnetic resonance scanner. Pneumatic, electromagnetic, and piezoelectric actuation systems have been employed for MRE examinations of the brain, and abdominal organs such as the liver. One of the goals of the current project was the comparison between the setup already in use at the host laboratory (based on a piezoelectric actuator, connected to a wave generator and a high voltage amplifier), a custom-made pneumatic device developed from scratch during the project and a commercial pneumatic actuator developed by Mayo-Clinic. The comparison involved motion deflection tests carried out in a gelatine phantom with a commercial accelerometer, and obtaining elasticity maps of the gelatine phantom, liver and brain. It was shown that the piezoelectric actuator is more powerful and enables a higher degree of control than the pneumatic actuator. Despite the disadvantages of the custom-made pneumatic system presented, shear elasticity measurements obtained with this system were consistent with the values for elasticity obtained with the piezoelectric set-up for phantom and liver experiments.

Another goal of the project was the validation and reliability test of MRE results using two different methods: Finite Element Modelling (FEM) and Dynamic Shear Testing (DST). In spite of the frequency limitations inherent to the DST technique, it was concluded that DST results can be extrapolated to higher frequencies and compared with experimental MRE. The results obtained with both techniques showed good agreement, confirming the validity of MRE for measuring tissue elasticity parameters.

This project was crucial in the development of the MRE technique at the host institution and represents a step further towards the acceptance of this new and promising diagnostic technique in clinical practice.

**Keywords:** Magnetic Resonance Elastography, Hardware, Finite-element method, Dynamic Shear Testing.

---





# Contents

<b>Acknowledgements .....</b>	<b>i</b>
<b>Resumo .....</b>	<b>iii</b>
<b>Abstract.....</b>	<b>ix</b>
<b>List of Abbreviations .....</b>	<b>xv</b>
<b>List of Figures.....</b>	<b>xvii</b>
<b>List of Tables .....</b>	<b>xxi</b>
<b>1. Introduction .....</b>	<b>1</b>
1.1 Motivation.....	1
1.2 Elastography Literature Review .....	2
1.3 Scope and Objectives .....	6
1.4 Thesis Structure .....	7
1.5 Contributions.....	8
<b>2. Background .....</b>	<b>11</b>
2.1 Elastic Properties of Tissue and Constitutive Equations .....	11
2.1.1 Stress and Strain .....	11
2.1.2 Mechanical Properties of Tissues .....	14
2.2 Magnetic Resonance Elastography .....	15
2.2.1 Induced mechanical excitation.....	17
2.2.1.1 Actuator system.....	18
2.2.2 Tissue displacement measurement.....	24
2.2.2.1 MREEPI Sequence.....	24
2.2.2.2 Phase difference calculation .....	30
2.2.3 Data processing .....	31
2.2.3.1 Phase Unwrapping.....	31

2.2.3.2	Filtering .....	32
2.2.4	Estimation of the Shear Modulus .....	33
2.2.4.1	Motion Equations.....	34
2.2.4.2	Inversion Techniques .....	36
<b>2.3</b>	<b>MRE clinical Applications .....</b>	<b>39</b>
2.2.1	Abdomen.....	39
2.2.2	Brain .....	40
2.2.3	Others .....	41
<b>3.</b>	<b>The Piezoelectric and the Pneumatic Actuators.....</b>	<b>43</b>
<b>3.1</b>	<b>Piezoelectric Actuator.....</b>	<b>43</b>
3.1.1	Piezoelectric Effect - Basic Principles .....	44
3.1.2	Hardware .....	44
3.1.2.1	Wave form generator and amplifier .....	47
3.1.2.2	Active Piezoelectric Actuator .....	50
3.1.2.3	Passive Actuators .....	52
<b>3.2</b>	<b>Pneumatic Actuator .....</b>	<b>56</b>
3.2.1	Acoustic Waves and MRE.....	57
3.2.2	Hardware .....	58
3.2.2.1	Pneumatic actuator 1.....	60
3.2.2.2	Pneumatic actuator 2.....	63
3.2.2.3	Pneumatic actuator 1 Vs Pneumatic actuator 2 .....	66
<b>3.3</b>	<b>Comparison between the Piezoelectric and the Pneumatic Actuator .....</b>	<b>68</b>
3.3.1	Motion Measurement.....	69
3.3.1.1	Phantoms .....	69
3.3.1.2	Instrumentation and Set-up.....	69
3.3.1.3	Accelerometer Results and Data Analysis.....	72
3.3.1.4	Double integration Process.....	72
3.3.1.5	Digital filtering for Double Integration.....	77
3.3.1.6	Accelerometer Results .....	81
3.3.2	Shear Elasticity measurements.....	86
3.3.2.1	Phantom study .....	86
3.3.2.2	Liver study .....	89
3.3.2.3	Brain study .....	91
<b>3.4</b>	<b>Conclusion .....</b>	<b>93</b>

<b>4. MRE Validation using DST and FEMs .....</b>	<b>95</b>
<b>4.1 MRE validation using FEMs.....</b>	<b>97</b>
4.1.1 Understanding Abaqus and its Analysis Steps.....	98
4.1.1.1 Part module .....	100
4.1.1.2 Property module.....	100
4.1.1.3 Assembly module .....	100
4.1.1.4 Step module .....	100
4.1.1.5 Interaction module .....	102
4.1.1.6 Load module .....	102
4.1.1.7 Mesh module.....	102
4.1.1.8 Job and Sketch module.....	103
4.1.2 FEM models – General Considerations .....	103
4.1.3 STUDY 1 - Examine the Influence of Purely Computational Parameters .....	104
4.1.4 STUDY 2 – Examine the influence of the experimental parameters: .....	108
<b>4.2 MRE validation using DST .....</b>	<b>109</b>
4.2.1 DST Instrumentation .....	110
4.2.1.1 Strain Rheometer .....	111
4.2.1.2 Stress Rheometer .....	111
4.2.2 Samples .....	112
4.2.3 Test Modes .....	113
4.2.3.1 Frequency sweep.....	113
4.2.3.2 Strain and stress sweep.....	113
4.2.4 Results and Discussion.....	114
<b>4.3 Conclusion .....</b>	<b>116</b>
<b>5. Conclusion and Final Remarks.....</b>	<b>119</b>
<b>5.1 Conclusion .....</b>	<b>119</b>
<b>5.2 Challenges.....</b>	<b>120</b>
<b>5.3 Future Plans .....</b>	<b>121</b>
<b>References.....</b>	<b>125</b>
<b>APPENDIX.....</b>	<b>137</b>
<b>APPENDIX A – Piezoelectric stack specifications.....</b>	<b>139</b>
<b>APPENDIX B – Commercial accelerometer Specifications.....</b>	<b>141</b>



# List of Abbreviations

AD	Alzheimer Disease
AIDE	Algebraic Inversion of Differential Equation
BC	Boundary Conditions
CRIC	Clinical Research Imaging Center
CT	Computed Tomography
DC	Direct Current
DST	Dynamic Shear Testing
EPI	Echo Planar Imaging
FE	Finite Element
FEG	Flow Encoding Gradient
FEM	Finite Element Method
FFT	Fast Fourier Transform
FIR	Finite Impulse Response
$f_{\text{mech}}$	Mechanical oscillation frequency
$f_{\text{MEG}}$	MEG Frequency
FOV	Field of View
IIR	Infinite Impulse Response
LFE	Local Frequency Estimation
MEG	Motion Encoding Gradient
MHRA	Medicines and Healthcare products Regulatory Agency
MR	Magnetic Resonance
MRE	Magnetic Resonance Elastography
MRI	Magnetic Resonance Imaging
MS	Multiple Sclerosis
$N_{\text{MEG}}$	Number of MEG cycles
SST	Static Shear Testing
TE	Echo-time
$T_{\text{mech}}$	Mechanical oscillation Period
$T_{\text{MEG}}$	Mechanical oscillation period
TR	Repetition Time
TTL	Transistor-Transistor Logic
WBIC	Wolfson Brain Imaging Center



# List of Figures

<i>Fig. 1.1 Dynamic Range of shear modulus and properties measured by the predominate imaging modalities of ultrasound, CT and MRI.....</i>	<i>2</i>
<i>Fig. 1.2 Schematic representation of current approaches to elastographic imaging: a) quasi-static Elastography; b) harmonic elastography and c) transient elastography. Adapted from [11] .....</i>	<i>4</i>
<i>Fig. 2.1 Stress principle. Adapted from [3].....</i>	<i>12</i>
<i>Fig. 2.2 Notations of stress components. Adapted from [3] .....</i>	<i>13</i>
<i>Fig. 2.3 Schematic representation of the main steps to obtain an elastogram in MRE. ....</i>	<i>16</i>
<i>Fig. 2.4 MRE system applied to the liver developed by Talwalker et al [34].....</i>	<i>18</i>
<i>Fig. 2.5 MRE system applied to the brain using a remote vibrator generator and a head rocker developed by Sack et al. [33].....</i>	<i>19</i>
<i>Fig. 2.6 MRE system applied to the liver using a remote vibrator generator connected to a wood rod developed by Sack et al [36].....</i>	<i>19</i>
<i>Fig. 2.7 Schematic diagram of the experimental set-up developed by Lewa et al [37].....</i>	<i>20</i>
<i>Fig. 2.8 Schematic diagram of an the MRE device used for phantom studies with quasi-static compression developed by Bishop et al [38].....</i>	<i>20</i>
<i>Fig. 2.9 MRE system developed by Plewes et al to study quasi-static deformation of breast tissue [39]. ....</i>	<i>21</i>
<i>Fig. 2.10 Electromagnetic actuator developed by Braun et al. Adapted from [40] .....</i>	<i>22</i>
<i>Fig. 2.11 Piezoelectric actuator developed by Dooley et al [43]. ....</i>	<i>23</i>
<i>Fig. 2.12 Piezoelectric system developed by Uffmann et al. [42] . ....</i>	<i>23</i>
<i>Fig. 2.13 Representation of a bipolar gradient. Adapted from [44] .....</i>	<i>25</i>
<i>Fig. 2.14 Sequence timing diagram of the MREEPI sequence. The timing corresponds to the acquisition of one time step of a single slice. ....</i>	<i>28</i>
<i>Fig. 2.15 Screenshot of the sequence special card to configure the MEG- specific parameters. ....</i>	<i>28</i>
<i>Fig. 2.16 A phase wrapped image of propagating shear waves in the brain and the image after is the same image after phase unwrapping and masking. [10].....</i>	<i>32</i>
<i>Fig. 2.17 Representation of different rheological models. [35] .....</i>	<i>36</i>
<i>Fig. 2.18 Slice from 3-D/3-axis abdominal MRE of healthy volunteer. [57] .....</i>	<i>40</i>
<i>Fig. 2.19 MRE results from two different volunteers. Differences between white matter and grey matter. a)anatomical image; b)wave propagation image; c) shear stiffness map; d) shear map overlaid on anatomical image. [20] .....</i>	<i>41</i>
<i>Fig. 3.1 Schematic representation of the main components of the MRE system used in this project. ....</i>	<i>45</i>

Fig. 3.2 Schematic representation of the MRE system used in this project in two different set-ups (liver set-up on the top and brain set-up on the bottom).	46
Fig. 3.3 3D models of the MRE system configuration for: a) liver imaging and b) brain imaging.	47
Fig. 3.4 Photography of the amplifier HV- PA550-2D from CGC Instruments currently in use [66].	47
Fig. 3.5 Connection between the waveform generator and the piezoelectric actuator. a) Wave form generator connected to the filter plate that has direct contact with the MR room; b) view of the filter plate from the magnet room and cables connection (high voltage cable identified), between the filter plate (connected to the wave form generator) and the piezoelectric actuator.	48
Fig. 3.6 CAD representation of the piezoelectric actuator used: a) configuration require to induce excitation in the brain; b) configuration required to induce excitation in the liver.	50
Fig. 3.7 Measurement of the actual displacement generated in the lever pin. The piezoceramic stack induces a displacement of 0.13 mm when a voltage is applied to it. The dimension of the lever that is installed at the moment is $225+9=234$ mm, so the displacement generated in the lever pin is of $a=3.3$ mm (amplification of 25 times the displacement produced in the piezoelectric stack). In the future a lever with $400+9=409$ mm will be installed and the displacement generated the piezoelectric actuator will be amplified 44 times instead of 25 times.	51
Fig. 3.8 Liver set-up. a) all set-up; identification of the wood paddle used to induce vibrations in the liver; b)wood stick separately.	52
Fig. 3.9 Brain set-up. Identification of the carbon fibre rod and of the head cradle.	53
Fig. 3.10 End of the carbon-fibre rod that connects to the active piezoelectric actuator: design of the carbon-fibre rod improved – with a pivot-type joint that enables some free movement in the direction of excitation.	54
Fig. 3.11 The head cradle (represented as a cylinder) sits on two pins attach to a base plate that allows it to rotate inside the head coil.	54
Fig. 3.12 Photographs of the old head cradle a) front view; b) side view.	55
Fig. 3.13 New head cradle used for the brain set-up of the piezoelectric system. a) Photographs of front and side view of the head cradle. The inflatable plastic for better coupling is highlighted; b) 3D modelling of the head cradle; c) dimensions of the head cradle at different views.	56
Fig. 3.14 3D general representation of a pneumatic device based on Ehman's design (also presented in Fig. 2.4).	59
Fig. 3.15 Pneumatic system 1 set-up. Identification of the components of the set-up.	60
Fig. 3.16 Schematic representation of the custom-made pneumatic subwoofer. Adapted from [74]	61
Fig. 3.17 Passive actuator (similar to the Mayo one) built to replace the plastic hand gel bottle. a) Photographs of the flexible membrane of the passive actuator (back view) (on the left), of the rigid wall (front view) (on the centre), and of the side view (on the right); b) 3D modelling of the new passive actuator; c) dimensions of the passive actuator at different views.	62
Fig. 3.18 Components of the commercial pneumatic system from Mayo Clinic that are places outside the magnet room a)active driver; b) connection of the plastic tube with the magnet room; c)electronics plate that makes the connection of the active actuator with the magnet room and MRI system.	63
Fig. 3.19 Representation of a subwoofer with an air compression system. Adapted from [74]	64



Fig. 3.20 a) side view and b) front view of the passive actuator from Mayo Clinic, coupled to the plastic tube.....	65
Fig. 3.21 Gelatine phantom attached to the accelerometer used to perform the motion deflection tests. ....	69
Fig. 3.22 Pneumatic actuator 2 set-up for motion measurement. Identification of different components of the set-up. ....	71
Fig. 3.23 Schematic representation of the different set-ups used to measure acceleration with the piezoelectric system in the liver set-up (a)) and in the brain set-up (b)) and with the pneumatic systems (pneumatic actuator 1: c) and pneumatic actuator 2: d)) .....	71
Fig. 3.24 Acceleration signal obtained using the piezoelectric system at 20Hz of vibration frequency.....	73
Fig. 3.25 Integration errors due to drift effect: a) after first integration of acceleration signal (velocity); b) after second integration of acceleration signal (position). ....	74
Fig. 3.26 Acceleration measured with the gravity effect. ....	75
Fig. 3.27 Integration errors due to gravity effect: a) after first integration of acceleration signal (velocity); b) after second integration of acceleration signal (position). ....	75
Fig. 3.28 Acceleration without gravity effect. ....	76
Fig. 3.29 Integration errors due to lack of initial conditions: a) after first integration of acceleration signal (velocity); b) after second integration of acceleration signal (position). ....	76
Fig. 3.30 Double integration errors corrected by using filtering. ....	77
Fig. 3.31 Block diagram of the double integration process. ....	77
Fig. 3.32 Frequency response of the high-pass FIR filter proposed [77]. ....	79
Fig. 3.33 Integration error when a FIR filter is used. [77] .....	79
Fig. 3.34 Acceleration signals obtained with three different setups: a) the piezoelectric liver set-up; b) the pneumatic custom-made set-up; and c) the commercial Mayo Clinic pneumatic set-up, at 5 different vibration frequencies (20, 40, 50, 80 and 100Hz). ....	83
Fig. 3.35 Magnitude peak-to-peak displacement values for both set-ups of the piezoelectric actuator (liver and brain set-up) with different waveform amplitudes (40% and 75%) for the custom-made pneumatic actuator and for the commercial Mayo Clinic pneumatic actuator at five different vibration frequencies (20, 40, 50, 80 and 100Hz). ....	84
Fig. 3.36 Magnitude peak-to-peak displacement values for the custom-made pneumatic actuator at five different vibration frequencies (20, 40, 50, 80 and 100Hz). ....	85
Fig. 3.37 Images of the set-up used to test the piezoelectric and the pneumatic actuator. The piezoelectric actuator was either tested with the brain and with the liver set-up. ....	87
Fig. 3.38 MRE data obtained for phantom with: a) and b) the piezoelectric system and c) and d) the custom-made pneumatic actuator. a) and c) are displacement wave images for 50, 100 and 200Hz and b) and d) are the corresponding shear stiffness maps. In the table below are presented the mean shear stiffness values for each one of the actuators for each frequency. ....	89
Fig. 3.39 MRE data obtained for liver with: a) and b) the piezoelectric system and c) and d) the custom-made pneumatic actuator. a) and c) are displacement wave images for 50, 62.5 and 75Hz and b) and d) are	

the corresponding shear stiffness maps. In the table below are presented the mean shear stiffness values for each one of the actuators for each frequency. .... 91

Fig. 3.40 MRE data obtained for brain with: a) and b) the piezoelectric system and c) and d) the custom-made pneumatic actuator. a) and c) are displacement wave images for 25Hz and b) and d) are the corresponding shear stiffness maps. .... 93

Fig. 4.1 Schematic diagram of the different modulus in Abaqus. .... 99

Fig. 4.2 Geometry representation of the 2D FE model representing a semi-axial cross section of the cylindrical MRE phantom. The bottom surface of the model was constrained in the vertical direction and a sinusoidal load was applied in the middle of the top surface (A). .... 104

Fig. 4.3 Shear wavelength ( $\lambda'$ ) as a function of the Young's Modulus ( $E$ ) from two models with different thickness. The crosses correspond to the model of 10 mm thickness and the dots symbols correspond to the model of 20mm thickness. The dashed line corresponds to the theoretical relationship between  $E$  and  $\lambda'$  (equation(2.8)). A density of  $1 \times 10^3 \text{ kg/m}^3$  was considered. .... 106

Fig. 4.4 Effect of the elements size on the shear wave propagation throughout the FEM and correspondent displacement profile measured at the top edge represented in a dashed line in the figure. The black arrow at the top edge in the corner represents the sinusoidal load applied to the model. Two models were created, both axisymmetric rectangular prism models representing a semi-axial cross section of the cylindrical gel phantom. The bottom edge of the prism was always constrained in the y-direction both have the same dimensions (100x20 mm) and differ on the elements size: a) elements size of 2x2 mm; b) elements size of 1x1 mm. Each image represents the time frame 80 for different Young's values (30, 60, 90 and 120 KPa) for both models. .... 107

Fig. 4.5 Shear wavelength ( $\lambda'$ ) as function of Young's Modulus ( $E$ ) with 150Hz of excitation frequency and at different densities of material. The dashed curves represent the three theoretical relationships between  $E$  and  $\lambda'$  for three different densities ( $0.5 \times 10^3 \text{ kg/m}^3$ ;  $1 \times 10^3 \text{ kg/m}^3$  and  $2 \times 10^3 \text{ kg/m}^3$ ). .... 108

Fig. 4.6 Particle motion in shear and extensional flows. [97] .... 110

Fig. 4.7 Photographs of the strain rheometer used in this study. .... 111

Fig. 4.8 Photographs of the stress rheometer used in this study. .... 112

Fig. 4.9 Image of the circular containers where the samples were poured to dry. .... 112

Fig. 4.10 Amplitude strain sweep of 3 gelatine phantoms with concentrations of 1:1; 1:2 and 1:3 (gel:water). The dashed line marks the limit of the linear viscoelastic limit. .... 114

Fig. 4.11 Storage modulus of the shear moduli versus frequency, for rotational rheometric data. Frequency sweep test of the three gelatine phantoms (concentrations of 1:1; 1:2; 2:3 (gel:water)). .... 115

Fig. 5.1 Schematic diagram of the process of MRE validation using FEMs: Images created with FE modeling mimicking MRE images are introduced in the inversion algorithm and the resulting shear modulus is compared with the shear modulus obtained for comparable images obtained experimentally with MRE. The values must be the same or very similar. .... 122

# List of Tables

<i>Table 3.1 Technical specifications of the three main components of the custom-made pneumatic actuator developed at the WBIC. ....</i>	<i>62</i>
<i>Table 3.2 Technical specifications of the three main components of the commercial pneumatic actuator developed in Mayo Clinic. ....</i>	<i>66</i>
<i>Table 3.3 Comparison of some important technical specification of the pneumatic actuator 1 and 2. ....</i>	<i>68</i>
<i>Table 4.1 Purely experimental parameters that affect MRE in-vivo results during the three different step of the MRE process discussed in section 2.2. ....</i>	<i>96</i>
<i>Table 4.2 Purely computational parameters that affect FEM results and parameters that affect both: the computational and the experimental results. ....</i>	<i>97</i>



# **1. Introduction**

## **1.1 MOTIVATION**

Elasticity is one of the most important physical properties of the human tissues and can be markedly affected by a variety of diseases such as cancer. For this reason, a technique or method that is able to detect abnormalities in tissue stiffness is definitely a valuable diagnostic tool. Palpation is a long-standing, standard medical practice, which is used to access stiffness variations in accessible regions of the body, allowing physicians to get more information about the elasticity of tissues. However, this technique is highly subjective because the examiner must rely on qualitative estimates and is clearly limited to regions that are accessible to physician's hands [1] [2].

Mechanical testing methods for biological tissues have been adopted from traditional material testing methods, for instance Dynamic Shear Testing (DST) and uniaxial or biaxial tension tests [3] [4]. Although these methods are a valuable tool and provide a wealth of information into the complex load-stretch response of biological tissues, they still have several limitations that will be discussed in detail in later sections of this dissertation. To overcome the limitations of the traditional shear testing of materials, there has been an increasing widespread availability of the latest imaging modalities such as ultrasound, Computed Tomography (CT) and Magnetic Resonance Imaging (MRI), that allowed unprecedented views into the body to distinguish tissue types and diseases states. Nonetheless, the dynamic range available in these modalities is dwarfed by the range of the tissue mechanical property of shear modulus. In Fig. 1.1 the ranges of measured parameters are illustrated for different imaging techniques. Ultrasound, for instance, provides contrast between tissue types via the bulk modulus (material resistance to a uniform compression) of the underlying tissues. However, while bone has a bulk modulus that is easily distinguished by the bulk modulus of soft tissue all soft tissues have similar bulk modulus, which is a disadvantage of this technique. Using standard MRI there is also a very narrow range of values within the organs. On the other hand, the shear modulus varies over several orders of magnitude and so, it has a vastly range of values for a variety of tissues. Therefore, the appeal of elastography is to make the most of the two great advantages of this long-standing technique: high level of specificity for mechanical property changes due to disease, and the inherently large underlying range of mechanical

properties. For those reasons, over the last decade, the recognition of the potential diagnostic value of characterizing mechanical properties, has led to the development of new and more precise techniques for imaging tissue elasticity using elastography. Elastography is based on the detection of tissue strain, produced by defined internal or external stresses and it has been used combined with conventional imaging techniques, like ultrasound imaging and MRI [5].

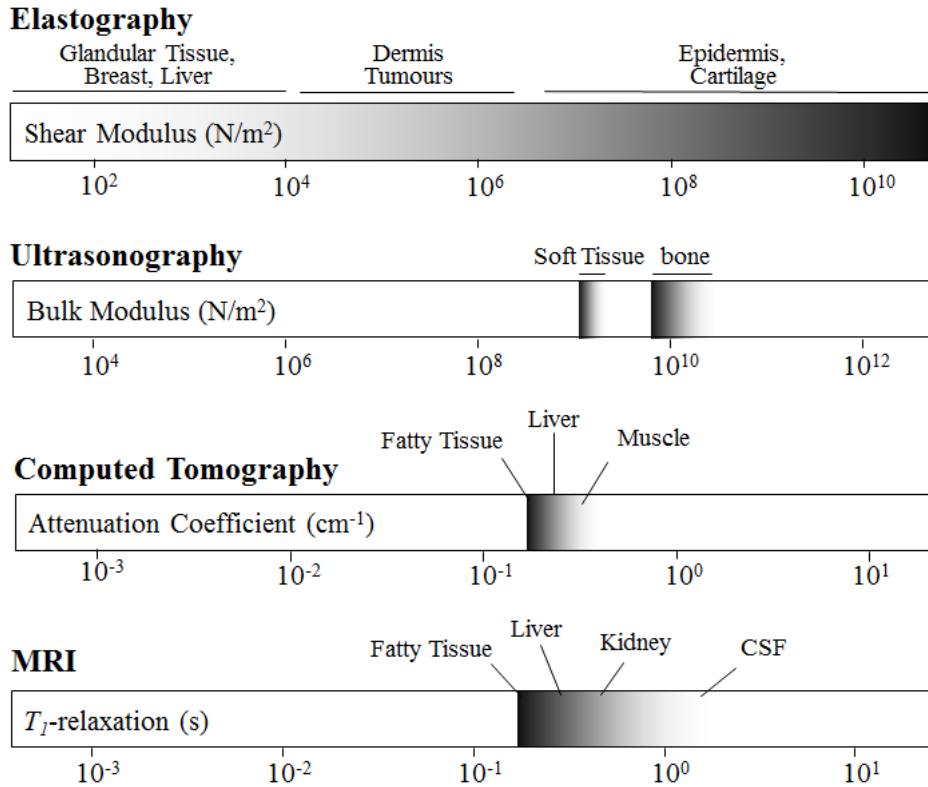


**Fig. 1.1** Dynamic Range of shear modulus and properties measured by the predominate imaging modalities of ultrasound, CT and MRI.

## 1.2 ELASTOGRAPHY LITERATURE REVIEW

Extensive research has been conducted over the past 15 years to develop and apply elastography methods. Elastography is an emerging imaging modality that is based on the transmission of low-frequency mechanical waves across the tissue of interest and exploits differences in the biomechanical properties of normal and diseased tissues. It was developed in the late 1980s to early 1990s to improve the diagnostic value of ultrasonic imaging. Nevertheless, this technique is strongly limited because only the displacement component in the direction of propagation beam can accurately be measured. Furthermore, it has inherent lack of lateral resolution and limited axial resolution when

compared with other clinically available imaging modalities [6]. Consequently, in the past few years, there has been an attempt to develop elastography systems based on other imaging modalities such as; optical coherence tomography [7] and MRI [8]. The imaging modality that makes use of MRI to measure the tissue displacements is called, Magnetic Resonance Elastography (MRE) and is one of the most promising techniques for in-vivo elasticity measurements. In MRE a conventional MRI system is used with an additional motion-encoding gradient imposed along a specific direction, switched in polarity at some adjustable frequency. Finally, this technique uses an inversion algorithm based on the measured displacements to calculate the shear modulus distribution in the tissue. One of the advantages of using MRI instead of ultrasonic imaging is that all three spatial components of the induced internal tissue displacements can be measured with high precision. Moreover, MRI sensitivity is higher [9].

From a classical point of view, for obtaining elastic properties of tissues a known stress is applied and then the resulting strain is measured [10]. Regardless of the method that is used to obtain the elastic properties there are three main principles of Elastography based methods that are stated as follows:

- (1) perturb the tissue using a quasi-static, harmonic or transient mechanical source;
- (2) measure the internal tissue displacements using a suitable ultrasound, optical or magnetic resonance displacement estimation method and;
- (3) infer about the mechanical properties of tissue from the measured mechanical response, using either a simplified or mechanical model.

Much of the pioneering work in elasticity imaging was done using a quasi-static model, a transient model or a dynamic model (Fig. 1.2).

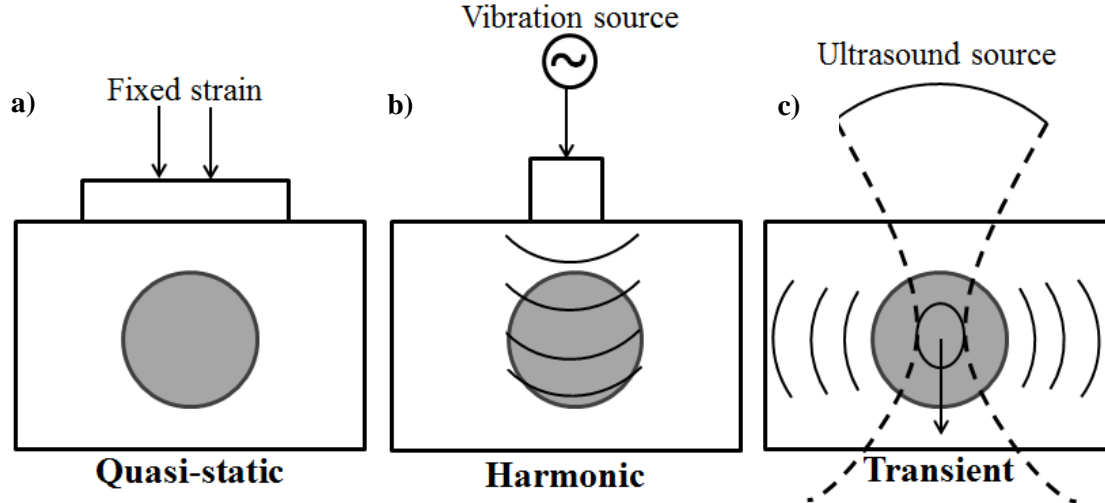


**Fig. 1.2** Schematic representation of current approaches to elastographic imaging: a) quasi-static Elastography; b) harmonic elastography and c) transient elastography. Adapted from [11]

In the **quasi-static elastography** (Fig. 1.2a)) approach a compression is applied to the target tissue at very low frequencies, around 1 Hz. The compression changes in each period of imaging acquisition, so it is assumed that the tissue is under approximately constant stress in each cycle, and the wave propagation is assumed to be negligible [12]. The first approaches of these types of images were with the use of ultrasound [13] but a magnetic resonance (MR) analogue was later described [14]. In this approach to Elastography a small axial compression is applied to tissue with a quasi-static mechanical source; the axial component of the internal tissue displacement is measured at each location and the longitudinal strain distribution is revealed. This quantity is a relative measure of elasticity as it depends on the magnitude of the force applied to it and on the elastic modulus of the material. Therefore, the images obtained provide a qualitative analysis about the elastic properties of the materials. A quantitative map of these images, of regional elastic modulus, can also be computed. This calculation requires an estimate of local stress distribution, which requires knowledge about the applied stress distribution. In quasi-static Elastography, soft tissues are typically approximated as a series of one-dimensional springs that are arranged in a simple fashion and so it follows Hooke's law that is described in more detail in section 2.1 of this dissertation.

**Harmonic elastography** (Fig. 1.2b)) consists mainly in two parts. The first part includes the transmission of mechanical waves through the tissue, and the second includes the analysis of the wave propagation and tissue deformation [6]. As in quasi-static Elastography, this approach was first proposed to be used combined with ultrasound



imaging and it was further extended to be used with MRI. Harmonic elastography combined with MRI is now the most used and prevailing method of MRE. In general, in harmonic elastography a sinusoidal mechanical source generates and transmits a low-frequency acoustic wave within the tissue. The phase and amplitude of the propagating waves are visualized using colour Doppler imaging or phase-contrast MRI [11]. The equations underlying the estimation of the velocity of the shear wave are described in section 2.1 of this dissertation. This shear-modulus estimation is relatively insensitive to noise, however the spatial resolution of the modulus elastograms is limited. Moreover, there is a further weakness of this technique because when waves are reflected from internal tissue boundaries, they can interfere constructively and destructively and influence the shear modulus calculation. [15]

Finally, the **transient elastography** (Fig. 1.2c)) approach is a method that was first developed [16] to overcome the limitation of harmonic elastography, where the waves attenuate rapidly in the tissue. The transient approach is a one-dimensional method that uses the acoustic radiation force of an ultrasound transducer to perturb tissue locally. Similar to what happen in the other two approaches, this approach was further developed to be used with MRI instead of ultrasound [17] [18]. In transient Elastography (one-dimensional problem) the source produces a vibration of low amplitude and frequency, which generates a shear wave that passes through the skin and tissue of interest. The propagation of the shear wave through the tissue is then accessed with the ultrasound or the MR technique. As in harmonic Elastography, local estimates of shear modulus are calculated from local estimates of wavelength. In this method, one can infer about the elastic properties of the tissue, owing to the fact that structures with higher elastic modulus tend to have lower vibrational amplitudes than the surrounding softer tissues [9] [11].

In this project, the shear modulus of tissues was accessed using harmonic elastography with MRI and thus, this approach to elastography will be further detailed in later sections of this dissertation. A detailed description of the other methods is beyond the scope of this work.

The data collected by elastography methods represent the displacement or the velocity maps of the underlying tissue. A lot of effort has been put in these techniques to convert the acquired images into representations of mechanical properties of the tissue, mostly into the Young's modulus or into the shear modulus. Different methods have been

developed and those that have been used in the analysis of the acquired images are described and detailed in section 2.2.4.2.

The use of imaging modalities with elastography has attracted considerable attention due to its potential ability to provide a novel and quantitative contrast mechanism relevant to the detection and tracking of tissue elasticity parameters and tissue disease. Elastography methods have been applied to different tissues, but in particular on the detection of tumours or nodules. Among all the applications of elastography the most popular include intravascular elastography [19], brain [20], heart [21], liver [22] [23], kidney [24], and muscle [25]. Different applications of MRE are going to be presented and discussed in section 2.3 of this report.

### **1.3 SCOPE AND OBJECTIVES**

Although MRE has benefited from over a decade of research by several groups around the world, it is still a relatively uncommon technique with a lot to explore and to improve. Therefore, applying this new modality to a specific application involves both technical and scientific development.

Recently, a new actuation MRE device was installed at the Wolfson Brain Imaging Center (WBIC) to apply to both brain and liver. First of all, it is important to learn more about MRE in general and its hardware and software. Furthermore, a lot of developments and improvements in the new system installed are needed. In order to fulfil these requirements, the current project can be divided in three major goals:

1. implement in clinical practice the MRE system developed at the WBIC;
2. understand the advantages and disadvantages of the piezoelectric actuation system and compared it with the other types of actuation devices, especially with the pneumatic system.

The aforementioned general goals of the present project can be split in more specific objectives that will integrate the chapters of this dissertation. In particular, to achieve the implementation of the piezoelectric system in clinical practise (topic 1), 5 different steps/objectives were kept in mind during the project:

improve and guaranty the safety of the piezoelectric actuator;

- 1.2) improve the performance of the actuator;

- 1.3) change the hardware to be more user-friendly by improving the design of some of the system's components;
- 1.4) change the hardware properties to increase patient comfort and;
- 1.5) obtain consistency and meaning of the results:
  - implement Finite Element Methods (FEM) to investigate the effect of different parameters such as excitation frequency material properties and boundary conditions on shear modulus and shear viscosity, before MRE can become a useful diagnostic tool;
  - validation of the MRE data obtained in-vivo using DST.

In order to understand the advantages and disadvantages of the piezoelectric actuator (topic 2), two main objectives are considered:

- 2.1) develop from scratch and implement a pneumatic actuator device;
- 2.2) compare the pneumatic system with the piezoelectric device by performing:
  - motion deflection tests with a commercial accelerometer and;
  - comparing shear elasticity modulus obtained using MRE in phantom, liver and brain, for both set-ups.

All the objectives enumerated above will be introduced in the chapters of this dissertation. To clarify the structure of this thesis, it is important to mention that the objectives related with the hardware of both set-ups (piezoelectric and pneumatic) and the comparison tests performed for both systems are described in chapter 3. In chapter 4, the validation tests using FEMs and DST are described and discussed. The structure of the this thesis will be further detailed next.

## **1.4 THESIS STRUCTURE**

This dissertation is divided in five main chapters: (1) Introduction; (2) Background; (3) The Piezoelectric and the Pneumatic Actuators; (4) MRE Validation using FEMs and DST; and (5) Conclusions, Challenges and Future Work. In the second and the third chapters the studies performed in the current project are presented as well as all the methodology used results obtained and their discussion and main conclusions.

Chapter 1 the Introduction chapter is particular important to give a brief overview and introduction to the state of the art, presenting literature review about elastography, scope and objectives of the project and thesis structure and contributions.

## **Chapter 1 - Introduction**

Chapter 0, the Background chapter is divided in three main sections: Elastic Properties and the constitutive equations, where an insight about the elasticity theory and equations is given; Magnetic Resonance Elastography, which is divided in the four main steps of the MRE process and finally; an overview about the clinical applications of MRE is given.

After the Background chapter, comes the Piezoelectric and the Pneumatic actuators chapter (chapter 3), where the project itself starts. In this chapter, all the methods used to implement, develop and improve both the pneumatic and the piezoelectric actuators are described. Furthermore, the methods used to compare both actuators are specified and the results are discussed. Finally, there is an overall conclusion of this first study.

The MRE validation using FEMs and DST chapter (chapter 4) is divided in two main sections: The first one, where the FEMs validation process is described and explained, and the second one, where the DST validation process is described. In the MRE validation using FEMs and investigation of parameters' influence; all the parameters that affect the MRE process either computational or experimental parameters are described and their influence in the MRE results is studied. In the MRE validation using DST the methods are explained and results of the DST study are presented and discussed. At the end there is a conclusion about validation techniques in particular about FEMs and DST processes.

Finally, in the chapter 0 of this dissertation the; Conclusions, Challenges and Future work are presented.

### **1.5 CONTRIBUTIONS**

This project was developed with the contributions, support and partnership of the Charité group, Berlin and of the Clinical Research Imaging Centre (CRIC), from the University of Edinburgh. The Charité group developed the MRE system that we have currently at the WBIC and provided all the material and MRI sequencing code to use the equipment in Cambridge. We visited their installations and we were part of one of their studies of liver and brain MRE. All the improvements and changes that were implemented to the hardware and software were performed with their advice and counselling. We also visited CRIC and familiarized with the pneumatic system that they are currently using for liver and muscle. We also took part on some of their MRE studies and discussed some ideas

about the project with them. These contributions and partnerships were crucial in the development of this project. Moreover, it was a great experience, personally but essentially professionally to visit their research centres and keep up to date with the projects in development in two of the most prestigious centres in MRE research. At the WBIC, the MRE project in general is supervised by Professor Marius Mada (my external supervisor) and during the year of my masters internship the MRE project was developed by Professor Marius Mada, PhD; Catarina Rua, MSc and myself, Joana Loureiro, MSc..



## **2. Background**

### **2.1 ELASTIC PROPERTIES OF TISSUE AND CONSTITUTIVE EQUATIONS**

All structural materials possess to a certain extent the property of elasticity. In other words, if external forces, producing deformation of a structure, do not exceed a certain limit, the deformation disappears after the stress that caused the deformation is no longer applied [26]. The properties of each material and its elastic behaviour are specified by constitutive equations. A wide variety of materials exists. Thus, it is not surprising that there is a huge variety of constitutive equations describing an infinite variety of materials. However, most of the materials that we deal with in the day-to-day life can be described by three simple, idealized, stress-strain relationships: the nonviscous fluid, the Newtonian viscous fluid and the Hookean elastic solid. [11] [3]

In most of the elasticity reconstruction approaches used in MRE, the mechanical behaviour of soft tissues is modelled based on the theory of linear elasticity following the Hooke's law, assuming that the soft tissue undergoing the action of external forces are perfectly elastic, homogeneous and isotropic (elastic properties are the same in all directions). However, it is well known that soft tissues are viscoelastic, exhibiting both fluid-like and elastic mechanical behaviour. These materials deviate from Hooke's law in various ways. Nonetheless, using the viscoelastic correspondence principle it is possible to generalize the purely linear-elastic equations to analogous viscoelastic equations [27] [28] [29] as it is going to be discussed later in section 2.2.4.

To have a better understanding of the different types of MRE reconstruction methods currently in use, in this section, stress and strain meanings are going to be described as well as the constitutive equations that describe linear elastic Hookean solids. The constitutive equations that describe materials with a different mechanical behaviour are not going to be presented because they are not applied in MRE reconstruction methods, thus are out of the scope of this project.

#### **2.1.1 Stress and Strain**

The stress-strain relationship is the key to extract elastic properties in the MRE process and is the basis of the reconstruction methods used to determine elastic parameters. This relationship is described next.

Stress is the force per unit area acting on a surface separating two sets of material particles on the two sides of the surface. In other words, stress is defined by the limit of the ratio  $\Delta T / \Delta S$ , where  $\Delta T$  is the force due to particles on the positive side of the surface area of  $\Delta S$  acting on the particles of the negative side of the surface. More generally, the concept of stress represents the interaction of the material in one part of the body on another. In Fig. 2.1 the stress principle is illustrated. Let's consider a material continuum  $B$  occupying a spatial region  $V$ , and a small element of area  $\Delta S$ . Drawing a unit vector  $v$  normal to  $\Delta S$ , it is possible to distinguish the two sides of  $\Delta S$  according to the direction of the unit vector  $v$ . Considering the positive side the side to which the normal vector points; the part of the material lying on the positive side exerts a force  $\Delta F$  on the other part, which is lying on the negative side of the normal. This force is dependent on the location and size of the area and the orientation of the normal.

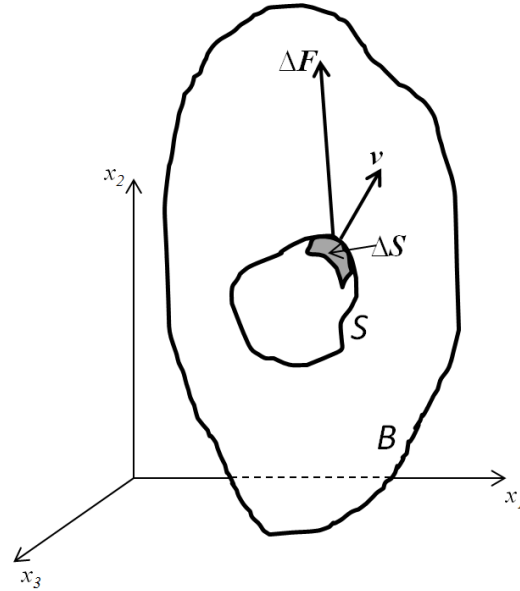


**Fig. 2.1** Stress principle. Adapted from [3]

From Fig. 2.2 we see that for each pair of parallel sides of a cubic element, one symbol is needed to denote the normal component of stress and two more symbols to denote the two components of shearing stress. Thus, to describe the stresses acting on the six sides of a cubic element the symbols;  $\tau_{11}, \tau_{22}, \tau_{33}$ , represent normal stresses and the symbols;  $\tau_{12}, \tau_{13}, \tau_{23}, \tau_{32}, \tau_{21}, \tau_{31}$  represent shearing stresses.



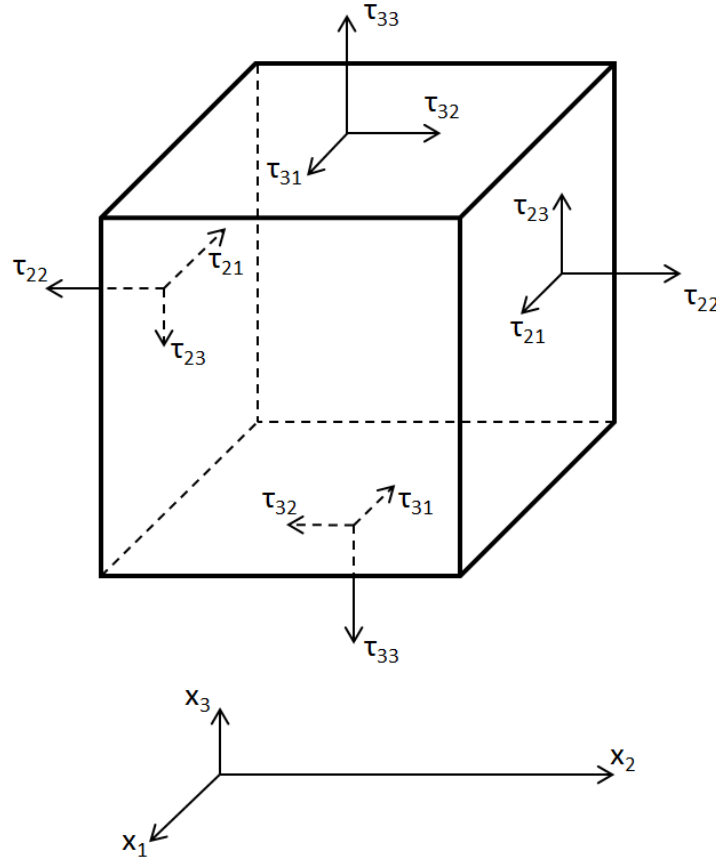


**Fig. 2.2** Notations of stress components. Adapted from [3]

Strain is considered to be the deformation of a solid that can be related to stresses. For instance, when a circular cylindrical shaft is twisted, the elements in the shaft are distorted and in this case the angle of distortion would be taken as a strain measure. It is also common to take the tangent of the distortion angle as the shear strain. The selection of proper strain measures is dictated by the stress-strain relationship (by the constitutive equation of the material) and normally this relationship is presented as a curve of the tensile stress  $\sigma$  plotted against the strain,  $e$ . [26] [3]

The stress-strain relationship is unique for each material and is found by recording the amount of deformation (strain) at distinct intervals of tensile or compressive loading (stress). These curves reveal many of the properties of a material such as Young's modulus ( $E$ ). Depending on the change of strain rate versus stress inside a material, the viscosity can be categorized as having a linear, non-linear, or plastic response. When a material exhibits a linear response the stress is linearly proportional to the strain rate; whereas Viscoelastic materials are those for which the relationship between stress and strain depends on time.

Depending on the relationship between stress and strain different constitutive equations can be created, each describing a material with different physical properties. The constitutive equations must be independent from any particular set of coordinates of reference with respect to which the components of various physical quantities are resolved. Therefore, a constitutive equation must be a tensor equation. In the next two sections the constitutive equations for linear elastic and viscoelastic solids are going to be described.

### 2.1.2 Mechanical Properties of Tissues

For infinitesimal deformations, one can assume that materials exhibit linear elastic behaviour and so they obey Hooke's law. Hooke's law states that the stress tensor ( $\sigma_{ij}$ ) is linearly proportional to the strain tensor ( $\epsilon_{kl}$ ) as follows:

$$\sigma_{ij} = C_{ijkl}e_{kl} \quad (2.1)$$

where the tensor  $C$  is the Cristoffel rank-four tensor consisting of 21 independent elastic constants. However, it is not certainly easy to develop methods to estimate 21 elastic parameters. Therefore, some assumptions must be made to reduce the number of independent elastic constants. The first assumption to be made is that the tissue exhibits purely elastic isotropic mechanical behaviour. Making this assumption the independent constants that are required to describe the mechanical behaviour of soft tissues are reduced to two: the first Lamé constant,  $\lambda$  and the shear modulus,  $\mu$  that normally is written as  $G$ . Nevertheless, this assumption is not valid for some tissues as it is going to be described later in this section. For linear isotropic elastic materials, the constitutive relation that describes the relationship between stress and strain is given by Eq. (2.2).

$$\sigma_{ij} = \lambda e_{\alpha\alpha}\delta_{ij} + 2\mu e_{ij} \quad (2.2)$$

where  $\delta_{ij}$  is the Kronecker delta,.

Inverting equation (2.2) to be solved for  $\sigma_{ij}$  instead of  $e_{ij}$ , and writing it we obtain equation (2.3).

$$e_{ij} = \frac{1+\nu}{E}\sigma_{ij} - \frac{\nu}{E}\sigma_{kk}\delta_{ij} \quad (2.3)$$

The constants  $E$ ,  $\nu$  and  $G$  are related to the Lamé constants;  $\lambda$  and  $\mu$  (or  $G$ ). Where;  $E$  is called Young's modulus,  $\nu$  is called Poisson's ratio, and  $G$  is called the modulus of elasticity in shear, or shear modulus. These constants can be written out as follows [30]:

$$\lambda = \frac{2G\nu}{1-2\nu} = \frac{G(E-2G)}{3G-E} = \frac{\nu E}{(1+\nu)(1-2\nu)} \quad (2.4)$$

$$\mu = \frac{\lambda(1-2\nu)}{2\nu} = \frac{E}{2(1+\nu)} \quad (2.5)$$

$$\nu = \frac{\lambda}{2(\lambda+G)} = \frac{\lambda}{3(K-\lambda)} = \frac{E}{2G} - 1 \quad (2.6)$$

$$E = \frac{G(3\lambda+2G)}{\lambda+G} = \frac{\lambda(1+\nu)(1-2\nu)}{\nu} = 2G(1+\nu) \quad (2.7)$$

As mentioned earlier, elastic properties of tissues, such as Young's modulus and Poisson's ratio, provide useful clinical information and consequently have become a subject of increasing research efforts [5] [31]. From equations (2.4) and (2.5), if the frequency of excitation,  $f$ , is known, it is possible to obtain further information about the propagation of the waves in the tissue, for instance, the velocity of the wave ( $c$ ) and the corresponding wavelength ( $\lambda'$ ) (equation (2.8)), and thus about the tissue itself.

$$c = \sqrt{\frac{G}{\rho}} \Rightarrow \lambda' = \frac{1}{f} \sqrt{\frac{G}{\rho}} \quad (2.8)$$

## 2.2 MAGNETIC RESONANCE ELASTOGRAPHY

Harmonic MRE is a non-invasive technique that can directly visualize and measure propagating acoustic strain waves in tissue-like materials subjected to harmonic mechanical excitation [8]. Fig. 2.3 illustrates a schematic representation of the main steps of an MRE exam necessary to obtain the elastograms of the tissue of interest.

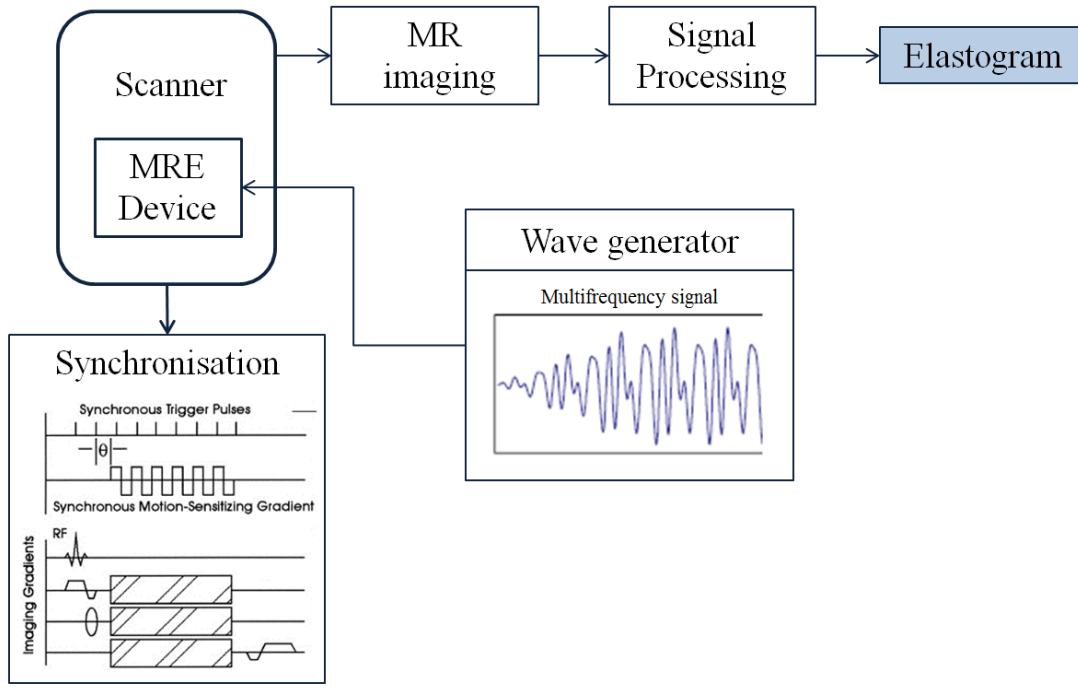


**Fig. 2.3** Schematic representation of the main steps to obtain an elastogram in MRE.

A conventional MRI system is used with an additional Motion Encoding Gradient (MEG), and a vibration device is used to mechanically excite the tissue. A vibration actuator creates shear or compression waves in the object at the same frequency as the MEG. Synchronisation is achieved by triggering the actuation device from the image sequence [32] [4]. Any cyclic motion in the presence of the MEG generates a phase shift in the signal from which it is possible to calculate the displacement at each voxel and directly image the acoustic waves within the tissue of interest. The phase MEG measures the mechanical vibration and the magnetic resonance image data is post-processed so that the phase and the amplitude of vibration can be acquired. Finally, an inversion algorithm based on measured displacements is applied to calculate the shear modulus distribution of the tissue.

In summary, it is considered that there are three main steps to obtain an elastogram (shear-modulus images) in MRE:

- (1) Apply an external mechanical stimulus. The internal displacement is dependent, not only on external and internal boundary, but also on tissue elastic properties.
- (2) Measure the displacement caused by the mechanical stimulation in tissue, by employing MRI.

- (3) Data processing and Estimation of the shear modulus within tissue from the measured displacements by applying an inversion technique.

The following three sections will describe in more detail each of the three abovementioned steps (Induced mechanical excitation; Tissue displacement measurements and; Inversion techniques).

### **2.2.1 Induced mechanical excitation**

When a mechanical wave is transmitted in the tissue medium, part of the kinetic energy is lost in the viscosity and thus the wave amplitude is gradually damped out with the depth of travelling. Therefore, attenuation is a function of travelling frequency excitation and the tissue property itself. The higher the frequency of excitation the more attenuation exists and the higher the damping coefficient is. Shear waves at frequencies in the 50-100 Hz range are ideal to use as a probe because they are much less attenuated than at higher frequencies. It should also be considered that excitation through fatty tissue is difficult because the mechanical waves are highly attenuated.

To generate mechanical waves, some form of an actuator is needed, or in other words, an oscillator that fulfils all the conditions and criteria listed is needed. Furthermore, the actuator should allow the variation of the frequency, amplitude and type of excitation depending on the tissue that it is going to be imaged.

The materials of the device must also be chosen carefully to be MR compatible since components that contain metal materials are likely to suffer induction of eddy currents under the varying gradient and interference with RF pulses, which can damage the device. Therefore, in MRE all the electronic equipment must be placed at least 1-2 m away from the scanner, and have all input/output cables filtered by low-pass filters, unless they are properly shielded. To ensure the normal activity of the devices and its safety in the MR environment, further testing must be done in five different ways: (1) Artefact tests; (2) SNR reduction measurements; (3) Geometrical distortion tests; (4) Magnetically induced force and torque tests and; (5) Thermal tests.

During the last decade, different types of devices have been developed depending upon the type of tissue that is being imaged and on the location. It is also important to consider the frequency of vibration.

To completely understand mechanical excitation in a MRE system, the hardware used in different MRE systems will be further described.

### *2.2.1.1 Actuator system*

Among the MRE devices developed to induce the mechanical excitation, there are generally three different approaches to guarantee the MR compatibility of the design:

**Type 1** - Remote actuation with long transmission;

**Type 2** - Electromagnetic coil with the main field and;

**Type 3** - Active actuation device near tissue of interest.

These three main approaches are going to be described next.

#### *Type1 - Remote actuation with long transmission:*

In this type of actuation a passive wave generator is placed near the magnetic isocentre. Then the actuation is transmitted from an actuation system located far away from the scanner through a long transmission system, such as a pneumatic mechanism or a long rod. In this case the active actuation system does not need to be strictly MR compatible [33].

Talwalker et al. [34] developed a liver MRE system consisting of; a loudspeaker (generates vibration) that is placed outside the magnet room to avoid EM interference and a passive actuator placed in patient's body over the liver as it is shown in Fig. 2.4. This was one of the systems used in this project and further details about this design and its advantages and disadvantages will be given in section 3.2 of this dissertation.

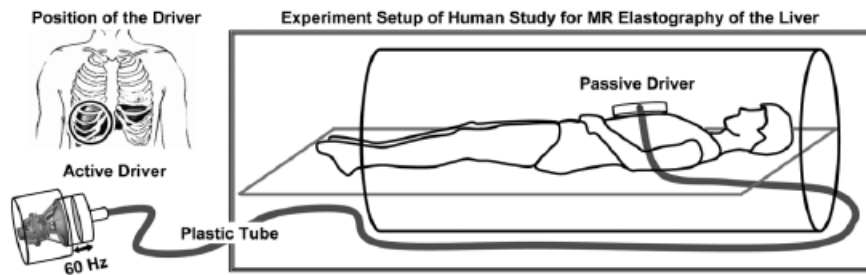


**Fig. 2.4** MRE system applied to the liver developed by Talwalker et al [34].

To have a better control on the vibration applied to the imaging tissue Sack et al [33] developed a design based on a loudspeaker connected to a long rigid carbon fibre rod of 2.8 m used for transmission. A head rocker unit is connected to the other end of the

carbon fibre rod introducing vibrations in the head and assisting the synchronization issue. The head rocker is designed to be adaptable to a standard MRI head coil. This system is represented in Fig. 2.5. Using a rigid fibre rod the phase lag introduced by the MRE acoustic system is eliminated. Nevertheless, the rigidity of the head cradle makes it less flexible, which means that the system just works on specific directions. The loudspeaker and all the electronics of this system need to be placed inside the magnet room (but far from the isocentre) potentially inducing EM interference and though SNR degradation.

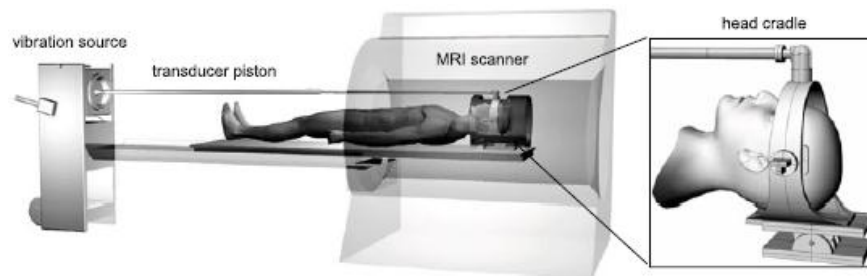


**Fig. 2.5** MRE system applied to the brain using a remote vibrator generator and a head rocker developed by Sack et al. [33]

Sack et al [35] have also developed a system similar to the MRE system described above but using a wood rod instead of the carbon fibre rod to vibrate the region of the liver as it is shown in Fig. 2.6.

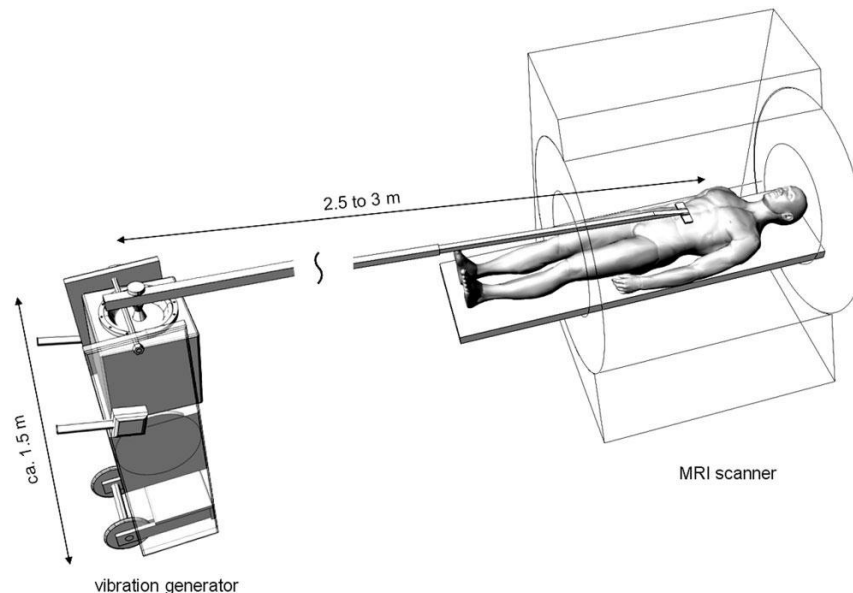


**Fig. 2.6** MRE system applied to the liver using a remote vibrator generator connected to a wood rod developed by Sack et al [36].

Sack et al. at the Charité, Berlin adapted these two set-ups and designs for brain and liver and developed a piezoelectric actuator to replace the acoustic actuator in the two systems described above. This piezoelectric system was adapted and was used in this project as it is going to be described in more detail in section 3.1 of this report. The pneumatic actuator developed by Talwalker et al. was later commercialized by Mayo clinic and this system was also used in this project (section 3.2). Moreover, this commercial system was adapted and a custom-made pneumatic system based on the Mayo-clinic system was developed in this project also in section 3.2.

Lewa et al [37] developed a commercial vibration generator connected to a long Plexiglas rod to vibrate a phantom. This device contains a permanent magnet and therefore it has to be far enough from the MR scanner to avoid EM interference. This system is represented in Fig. 2.7.

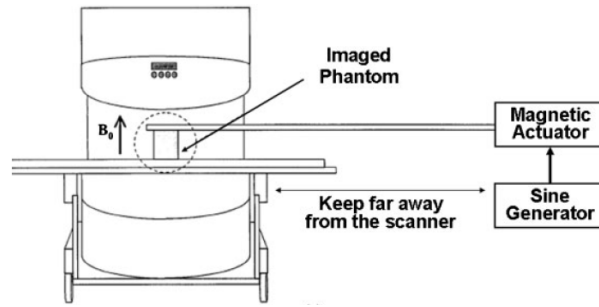


**Fig. 2.7** Schematic diagram of the experimental set-up developed by Lewa et al [37].

Systems that use ultrasound motors (type of electric motor powered by the ultrasonic vibration of a component) were also developed. Bishop et al [38] developed a system for delivering quasi-static compression for elastography as represented in Fig. 2.8.

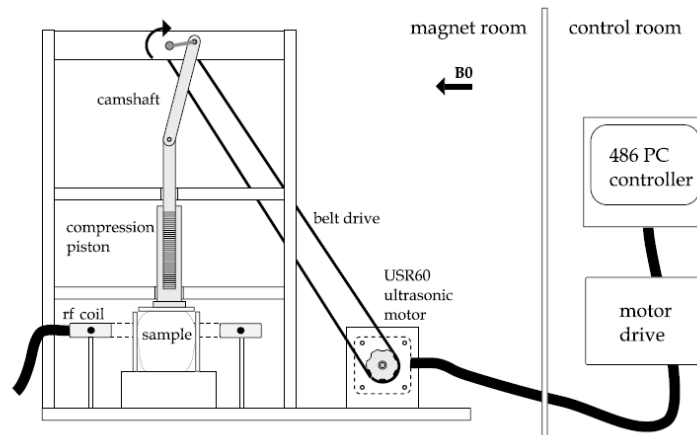


**Fig. 2.8** Schematic diagram of an the MRE device used for phantom studies with quasi-static compression developed by Bishop et al [38].



This device is based on an ultrasonic motor USR60 (Shinsei Corporation Inc) which is MR compatible. In this system rotatory motion is converted in a linear motion with frequencies of 1-2Hz and amplitudes up to 5 mm.

Plewes et al [39] modified the system developed by Bishop et al for breast elastography as shown in Fig. 2.9. In this system the vibrator is attached to the side of the commercial phased-array breast coil. An ultrasound motor is placed around 30 cm away from the target tissue and connected to the moving plate via a driveshaft.

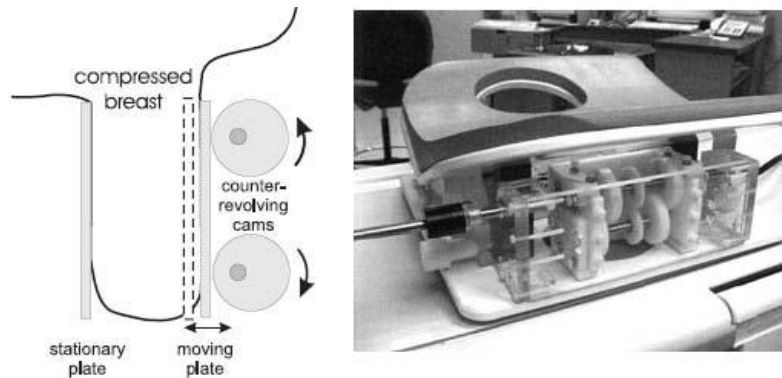


**Fig. 2.9** MRE system developed by Plewes et al to study quasi-static deformation of breast tissue [39].

### ***Type2 - Electromagnetic coil with the main field***

In this type of actuators, electromagnetic coils are used by making use of the main field  $B_0$  to generate alternative movement. More precisely, the electromagnetic actuators consist of a coil with several windings through which a sinusoidal current can be fed. The alternating current will induce an alternating torque which causes a periodic mechanical rotation of the coil and the rotatory motion generated can be used to excite the tissue according to Lorentz law of actuation. To minimize the EM interference and the effect of the uneven magnetic field due to the switching gradients, the number of turns in a coil should be optimized [40] [41]. These type of actuators have the advantage of being able to achieve high excitation amplitudes (on the order of 1mm), that can be easily obtained even with low power requirements of the amplifier. Moreover, these systems are generally inexpensive and comparatively simple in terms of design. Nevertheless, they are inflexible in terms of the device position as the vibration amplitude is dependent on the coil position and orientation. Another disadvantage of these systems is that the images can have artefacts because the currents in the coil can disturb the main field.

Braun et al. [40] developed an electromagnetic actuator for generating variably oriented shear waves, represented in Fig. 2.10. In this system oscillatory movement is induced along the z axis, when a current is applied to the actuating coil. To choose the direction of excitation a redirection plate is used between the excitation plate and the coil. Inserting the excitation plate at different holes different directions will be chosen.

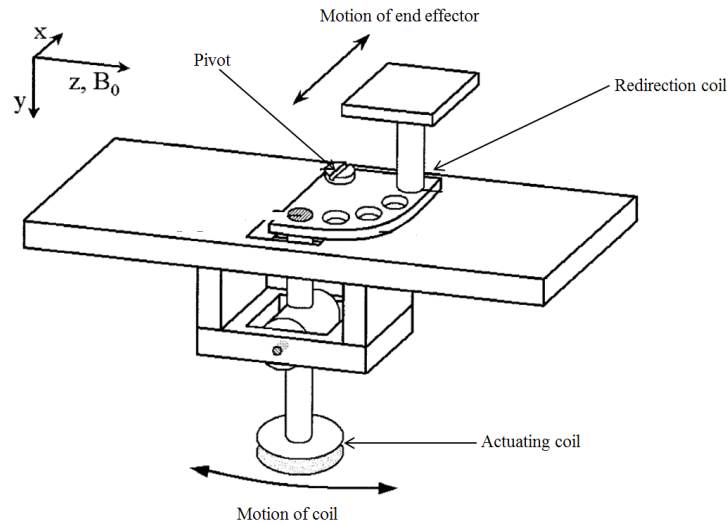


**Fig. 2.10** Electromagnetic actuator developed by Braun et al. Adapted from [40]

### ***Type3 - Active actuation device near to the image of interest***

In this case an active actuation system is placed near to the target tissue. To prevent elevated force or torque induced by the magnetic field, the end effector must be MR compatible. Furthermore, all the active components, like piezoelectric materials, have to be properly shielded with signal cables and filtered by low pass filters to avoid EM interference with the scanner [42]. Piezoelectric actuators can generate high forces which allow amplifying the amplitude and make it reach a level that will lead to an amplitude of excitation almost independent of the coupling resistance of tissue. This is a huge advantage of these systems; however, a piezoelectric system is expensive and requires a much greater design effort than the electromagnetic actuators and acoustic actuators [41].

Doyley et al [43] developed a piezoelectric system which consists of a wave driver applied inside the diameter spherical imaging volume. A maximum displacement of 40 $\mu$ m is achieved which is a disadvantage of this device. This system is represented in Fig. 2.11.

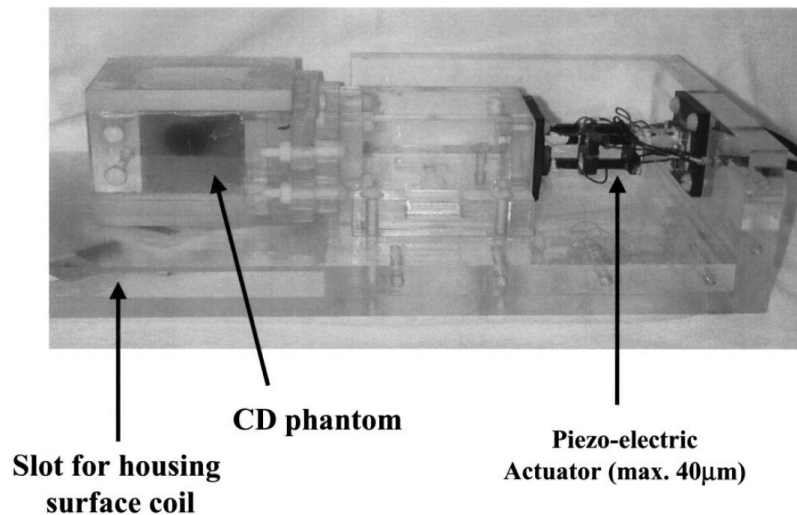


**Fig. 2.11** Piezoelectric actuator developed by Doyley et al [43].

Higher displacements can be achieved by increasing the number of elements in the piezoelectric stack. Based on this information Uffmann et al. [42] developed a system which can generate amplitudes of up to 1mm and is capable of operating at an excitation frequency of up to 500Hz. The piezoelectric stack has 247 mm of length and 18.5 mm of diameter. This mechanism generates a 200  $\mu\text{m}$  displacement. To amplify this displacement to a ratio of 1:5 a lever is attached to this mechanism. This system is presented in Fig. 2.12.

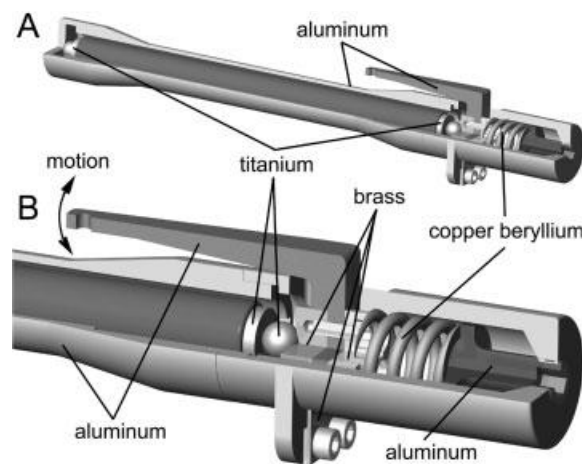


**Fig. 2.12** Piezoelectric system developed by Uffmann et al. [42] .

In summary, in this project three different actuation systems of type 1 were used, in which two of them are pneumatic and the other is piezoelectric. One of the pneumatic actuators used was custom-made and the other two actuation systems were adapted from the Mayo clinic set-up and from the Charité group piezoelectric set-up.

### **2.2.2 Tissue displacement measurement**

In MRE it is the addition of a MEG to the MRI sequence that enables the measurement of the displacement generated by the mechanical excitation. Therefore in order to understand this step of the MRE process the sequence and the MEG added to the sequence will be further detailed. Moreover, motion equations are important to determine motion parameters of the propagating waves in the tissue and therefore, they will also be described in this section.

#### **2.2.2.1 MREEPI Sequence**

In this section the MREEPI pulse sequence is a specific sequence used for Siemens scanners (used in this project) that is going to be further illustrated. The meaning of the individual special parameters will be explained.

The MREEPI sequence is based on a standard spin-echo EPI sequence and is equipped with an additional motion encoding gradients (MEGs) to make the sequence sensitive to spin motion.

#### ***MREEPI Working Principle***

To understand the sequence itself it is important to first understand the working principles of the MEG. The MEG is one type of Flow-Encoding Gradient (FEG). This type of gradient is a wave form that encodes information about macroscopic flow or coherent motion into the phase of the MR signal. With FE gradients the three logical axes (readout, phase encoding, and slice selection) are treated independently. Consequently, FEG can be added to a single axis, to any two or to all three axes during a given pulse sequence. In addition, with these gradients, information about velocity, acceleration or higher derivatives of motion can be obtained.

In the specific case of a Spin echo sequence, a  $180^\circ$  pulse is added after the  $90^\circ$  pulse which forms an echo by spin rephasing [44]. This echo can be measured by a second gradient applied. This second gradient produces a negative phase shift. Therefore, if the area under the two gradients is the same, then, the net phase of the stationary spins is zero and is different of zero for moving spins. This extra phase shift, generated for moving spins, provides quantitative information about them.

Amongst all the FEG the most common is a bipolar velocity-encoding gradient, which is comprised of two lobes of equal area and opposite polarity (Fig. 2.13). Owing to the fact

that the net area under the bipolar gradient is 0, no net phase accumulation is produced for stationary spins. On the other hand, for spins moving along the direction of the gradient the bipolar gradient produces a phase accumulation that is proportional to their velocity.

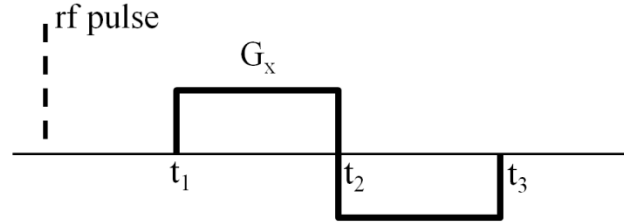


**Fig. 2.13** Representation of a bipolar gradient. Adapted from [44]

Specifically, the MEG is a gradient waveform that consists of a long train of small bipolar elements. Therefore, although any single bipolar element produces only a small phase accumulation, the net effect of all the elements together is easily measurable. In the MREEPI sequence, different waveforms, according to 0th, 1st and 2nd order gradient moment nulling are available to achieve different levels of suppression of non-harmonic motion components.

In MRE, the set of elements is synchronized to the oscillation of the mechanical actuator that induces the shear waves in the target tissue. It is because of that synchronization that wave motion with amplitudes on the order of hundreds of nanometres or less can be mapped, hence allowing non-invasive measurement of the shear modulus of the object. The synchronization of the scanning sequence and the vibration of excitation are extremely important, because any phase lag between the scanner image acquisition and mechanical vibration will produce a cumulative error in the measurement of the wavelength [44]. Specifically for the MREEPI sequence, it starts by sending an external trigger pulse to the vibration generator and thus initiates excitation of mechanical vibrations. After a certain delay, to allow for wave propagation into the region of interest, the usual imaging procedure occurs, comprising a sequence of  $90^\circ$  excitation pulse, motion encoding gradients,  $180^\circ$  refocusing pulse and the full k-space readout in the standard EPI fashion.

The measurement is repeated several times, with the delay between the initial trigger pulse and the onset of the MEG increasing stepwise by an integer fraction of the mechanical vibration period. This leads to the acquisition of several phases of wave propagation and allows for the extraction of the oscillation component at the excited

frequency by means of temporal Fourier transform. Since the MEG only encodes the projection of spin displacement onto the direction of the MEG, three sets of measurements have to be performed, each with the MEG played out along one of the three Cartesian axes, so that full 3D information about the displacement vector field becomes available. [45]

In summary, the MEG causes a cyclic motion on the spins that generates a measurable phase shift in the received nuclear magnetic resonance signal. From this measurable phase shift it is possible to calculate the displacement at each voxel, and directly image the acoustic waves within the tissue.

### *Nomenclature and Symbols*

In this section the main terms and symbols of the MREEPI sequence will be defined.

- **MEG frequency,  $f_{\text{MEG}}$ :** The frequency of the motion encoding gradient.
- **MEG period  $T_{\text{MEG}}$ :** The duration of one cycle of the motion encoding gradient, according to  $f_{\text{MEG}} = 1/T_{\text{MEG}}$ .
- **Number of MEG cycles,  $N_{\text{MEG}}$ :** The number of cycles in the MEG waveform. If  $N_{\text{MEG}} > 1$ , the MEG waveforms comprises a repetition of one MEG period, thus the total duration of all motion encoding gradients is  $T_{\text{total}} = N_{\text{MEG}} \cdot T_{\text{MEG}}$ . Note that for 2nd order gradient moment nulling an even number of MEG cycles is required.
- **Mechanical oscillation frequency  $f_{\text{mech}}$ :** The frequency of the mechanical vibration. Usually a sinusoidal waveform is employed. Note that this quantity is in general independent of the MEG frequency.
- **Mechanical oscillation period  $T_{\text{mech}}$ :** The period of one oscillation of the mechanical vibration, according to  $f_{\text{mech}} = 1/T_{\text{mech}}$ .
- **Trigger delay  $\tau$ :** The temporal separation between the initial trigger pulse and the start of the MEG waveform. This delay allows for wave propagation into the region of interest.

### *Timing of the MREEPI sequence*

Fig. 2.14 illustrates the sequence timing for the acquisition of one image of a slice.

In the MREEPI sequence, the echo time TE (defined as the interval between the 90° RF pulse and the center of the readout block, when the baseline in k-space is sampled), is

evenly divided in two halves. In the same figure two green vertical lines are seen that demarcate the interval in the first half of the TE in which no imaging-specific events occur. This interval is the maximum encoding time, which can be used for motion encoding and will be referred to as encoding slot. This parameter cannot be changed and is shown on the sequence special card as immutable (Fig. 2.15). The goal is to fit as many MEG cycles as possible (at a specific MEG frequency specified before) into the encoding slot. The first MEG starts at the beginning of the encoding slot and if the MEG waveforms do not fill the slot entirely, a delay between the end of the MEG and the 180° pulse will be inserted.

$\tau$  represents the temporal separation of the initial trigger pulse (red line) and the start of the MEG. It incorporates the fat saturation pulse, the 90° excitation, acquisition of EPI calibration scans and dephasing/rephasing gradients.

Finally, it should be mentioned that, for trapezoidal gradients the durations of ram-up, the flattop and the ram-down need to be multiples of 10  $\mu$ s, which will interfere with the MEG period and frequency. Therefore, the values on the sequence special card will be updated automatically, so that only parameters that will lead to a valid sequence timing can be configured.

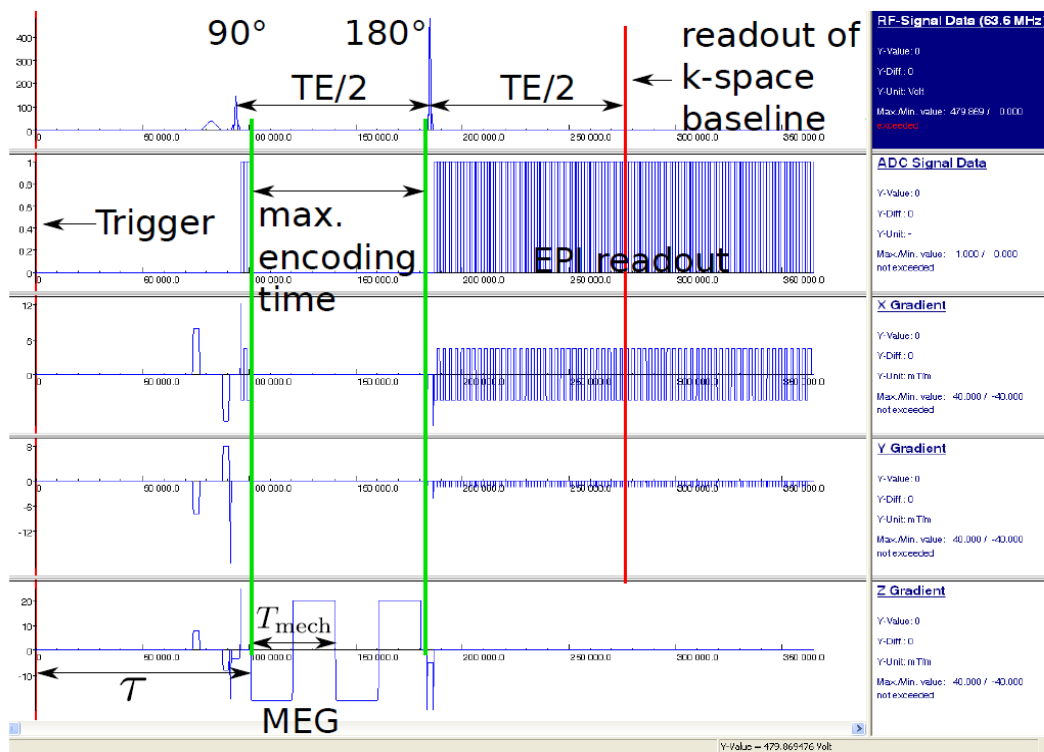


**Fig. 2.14** Sequence timing diagram of the MREEPI sequence. The timing corresponds to the acquisition of one time step of a single slice.

### *Sequence Special Card Parameters*

Fig. 2.15 shows a screenshot of the sequence special card. Each one of the parameters shown in the figure will be further described.

The screenshot displays the 'Special' tab of a sequence configuration interface. At the top, a status bar shows: TA: 0.4 s, PM: REF, PAT: Off, Voxel size: 3.9×3.9×5.0 mm, Rel. SNR: 1.00, and : epse. Below this, the 'Special' tab is active, showing a grid of parameters. On the left, parameters include MEG frequency (50.0 Hz), Amplitude (20 mT/m), Slewrate (100 mT/m/r), Encoding direction (SS), Gradient moment nulling (0th), MEG polarity (UP-DOWN), and Mechanical frequency (50.0 Hz). On the right, parameters include time steps (1), Trigger forerun (100000 μs), Max. encoding time (82610 μs), and Trigger mode (One pulse). At the bottom, a row of tabs includes Routine, Contrast, Resolution, Geometry, System, Physio, Inline, and Sequence.

**Fig. 2.15** Screenshot of the sequence special card to configure the MEG- specific parameters.

In Fig. 2.15 a screenshot of the sequence card is illustrated.

- **MEG frequency:** The frequency of the motion encoding gradient ( $f_{\text{MEG}}$ ) in Hertz.
- **Amplitude:** The amplitude of the motion encoding gradient. The unit is mT/m.
- **Slewrate:** The MEG slewrate, i.e. the steepness of the gradient lobes. The unit is mT/(m· ms). Using excessively high values can lead to failure in running the sequence due to safety limits or hardware restrictions.
- **Encoding directions:** The gradient axis/axes on which the MEG will be played out. This parameter is internally linked to the number of repetitions, i.e. selecting all 3 instead of a single direction will triple the total measurement time.
- **Gradient moment nulling:** The order of gradient moment nulling. Possible values are *0th*, *1st* and *2nd*. 0th moment nulling corresponds to a MEG waveform of a rectangular sine (as shown in Fig. 2.14). 1st moment nulling approximates a rectangular cosine. It has the advantage of being insensitive to constant-velocity spin motion, e.g. laminar flow. 2nd moment nulling has a more complex



waveform. Only even numbers of gradient cycles are feasible. A train of 2 cycles comprises 4 trapezoidal gradient lobes with duration of  $T_{\text{MEG}}/2$  each. If the number of MEG cycles that could potentially fit into the encoding timeslot is odd, that number will be reduced by 1 to ensure that the number of cycles is even. 2nd moment nulling is insensitive towards spin motion at constant velocity and constant acceleration, with a generally reduced sensitivity at low vibration frequencies.

- **MEG polarity:** The (relative) polarity of the gradient waveform. Possible values are *UP-DOWN* and *DOWN-UP*, which correspond to mutually inverse waveforms.
- **Mechanical frequency:** The frequency of the external vibration ( $f_{\text{mech}}$ ). This parameter does not necessarily match the MEG frequency. If more than one MEG cycle is employed, one should be attentive, since in that case the motion encoding sensitivity may have nulls for certain vibration frequencies, in which case no motion can be detected. The minimum value is determined by the sequence timing, most notably the trigger forerun parameter. If the trigger forerun is increased, lower mechanical frequencies will be allowed.
- **Time steps:** The number of points with which one wave period  $T_{\text{mech}}$  is sampled. At least two points are necessary to extract information about the vibration amplitude. Higher numbers are advisable to facilitate temporal phase unwrapping and to increase the spectral resolution of a temporal Fourier transform.
- **Trigger forerun:** The trigger delay ( $\tau$ ) discussed above, i.e. the temporal separation between the trigger that initiates the vibration and the start of the MEG, measured in microseconds. A value of 100,000  $\mu\text{s}$  is considered sufficient; if too small values are used, probably the wave has not fully propagated into the region of interest when the image acquisition starts. Increasing the value might necessitate increasing the repetition time  $TR$ .
- **Max. encoding time:** The length of the encoding slot, i.e. the maximum time that can be used for motion encoding. The sequence tries to fit as many cycles of the MEG frequency as possible into that time slot. The maximum encoding time is determined by many sequence parameters, the easiest way to change it is to change the  $TE$ .

- **Trigger mode:** Possible values are *One pulse* and *Two pulses*. *One pulse* causes the scanner to send a single optical pulse of duration  $10\ \mu\text{s}$  for every trigger event. One pulse might switch the output from 0 to 1, the next pulse causes a transition from 1 to 0 and so on. In the *two pulses* mode, two optical pulses of temporal of duration  $10\ \mu\text{s}$  and spacing  $20\ \mu\text{s}$  are sent, so that the output will be activated by the first pulse, only to be deactivated by the second pulse  $20\ \mu\text{s}$  later.

### 2.2.2.2 Phase difference calculation

As it was described before, phase contrast MRI is based on the premise that the phase changes will appear when, in the presence of a magnetic field gradient, the protons will move and so the net phase change,  $\phi(t)$ , can be measured. This net phase change is given by equation (2.9), and occurs over a time  $t$  from 0 to  $T$  when a spin with position vector  $r(t)$  is in the presence of gradient  $G(t)$  and  $\gamma$  is the gyromagnetic ratio for the spin.

$$\phi(t) = \gamma \int_0^T G(t) \cdot r(t) dt \quad (2.9)$$

The spins are subjected to a uniform velocity  $v(t)$ , their position is given by the following equation:

$$r(t) = r_0 + v(t) \quad (2.10)$$

Where  $r_0$  is the location of the spin at  $t=0$ . If equation (2.10) is substituted in equation (2.9), the following equation is obtained:

$$\phi = \gamma \int_0^T G(t) \cdot r_0 dt + \int_0^T G(t) \cdot v(t) dt \quad (2.11)$$

Analysing equation (2.11) it is interesting to note that not only the moving spins but also the stationary spins will contribute to the phase accumulation. In a normal MRI sequence the stationary spins will be used, however, in MRE only the phase accumulation that occurs due to the moving spins is of interest. Therefore, to eliminate the contribution of the stationary spins the MEG is added and the net phase is calculated from the average of two acquisitions that are obtained with opposite MEG, as it was explained in the previous section. To a better understanding, one could say that the gradient is switched in polarity to cancel the voxels that are in steady-state and reveal the moving tissue. This technique is highly sensitive only to motion that is precisely synchronized with the sensitizing gradients and so it is much less sensitive to physiologic motion than in a conventional gradient echo sequence.

Considering a specific case in which the spins are undergoing simple harmonic motion about their mean position  $r$  the following equation is obtained:

$$\zeta(r, \theta) = r_0 + \zeta_0 \cos(k_r r - \omega t + \theta) \quad (2.12)$$

Where  $\zeta_0$  is the amplitude of vibration and  $\omega$  is the angular frequency of vibration;  $k_r$  is the wave number; and  $\theta$  is the initial phase offset between the motion encoding gradient and the mechanical excitation.

If sinusoids are chosen to be the gradient function (  $G(t) = G_0 \cos(\omega t)$ ;  $t \in [0, NT]$  ),

where  $N$  is the number of gradient cycles and  $T=2\pi/\omega$ ; the phase shift caused by a propagating mechanical wave vector  $k$  within a medium at a given frequency ( $1/T$ ) in the presence of this cyclic motion-encoding gradient is given by equation (2.13) [8]:

$$\phi(\vec{r}, \theta) = \frac{\gamma NT (\vec{G}_0 \cdot \vec{\zeta}_0)}{2} \cos(\vec{k} \cdot \vec{r} + \theta) \quad (2.13)$$

The phase shift is proportional to the scalar product of the displacement amplitude vector  $\vec{\zeta}_0$  and the motion sensitizing gradient vector  $\vec{G}_0$ , and the relative phase  $\theta$  of the mechanical and magnetic oscillations. Analysing equation (2.13) it is clear that particles whose component of motion along the gradient vector are exactly in phase or out of phase with the magnetic oscillation, have maximum phase shifts of opposing polarities. In contrast, particles whose component of motion along the gradient vector is  $90^\circ$  out of phase with it have no net phase shift [1]. This method provides extreme sensitivity to small amplitude synchronous motion, since the response is also proportional to  $N$  and  $T$ , and so the phase shifts can be accumulated over multiple cycles of mechanical excitation and the MEG waveform.

### 2.2.3 Data processing

To remove unwanted contributions to the phase raw data obtained directly from the MRI scanner the data are processed and treated. Processing algorithms to analyse the obtained data include phase unwrapping, removal of concomitant gradient field effects, and directional filtering to enhance the accuracy of the elastograms.

#### 2.2.3.1 Phase Unwrapping

Shear waves attenuate quickly in soft tissue and therefore large amplitudes of vibration may be required to make the waves propagate in deeper regions. However, if the

amplitude is too high, phase wrap can occur. In other words, if there is enough amplitude to cause phase shifts outside the range from 0 to  $2\pi$  or from  $-\pi$  to  $\pi$  there will be phase wrap and the process of measuring the total accumulated phase is called phase unwrapping (Fig. 2.16). To overcome this issue, algorithms to phase unwrap MRE images have been developed [46] [47].

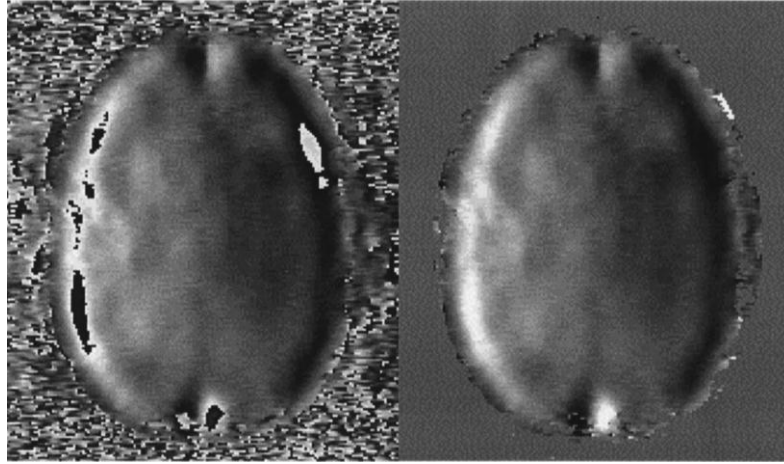


**Fig. 2.16** A phase wrapped image of propagating shear waves in the brain and the image after is the same image after phase unwrapping and masking. [10]

As it is not the main subject of this project, the unwrapping algorithms are not going to be detailed here, it is though, just essential to understand the importance of these algorithms in the process of obtaining the elastograms of the target tissue.

In the next section the importance of filtering will be discussed.

#### 2.2.3.2 Filtering

The most common inversion techniques (described in the next section) are based on the fundamental equation of motion and depend only on the presence of motion in a determined region of the tissue being imaged. However, these methods are highly influenced by complex interference patterns as reflexion and refraction which represent a problem for inversion algorithms since they create areas of low displacement amplitude and hence low SNR. For this reason filtering MRE data is an important step before applying the inversion technique to the images.

Different types of filters can be used to improve the elastograms maps such as Gaussian and Butterworth filters (Low Pass, Band Pass and High Pass). The cut off frequencies have a huge influence on the final results, and they should be chosen carefully.

Manduca et al. [48] used the approach of spatio-temporal directional filtering to improve the inversion of MRE images. These filters are designed in frequency space to select the portions of the wave field propagating in a specific direction. These filters are a product of radial and spatially directional components and also oriented in time. First data is converted into 3D frequency space (two spatial directions and one temporal). The radial components are Butterworth band pass filters, which are useful in removing high frequencies (noise) and low frequencies (bulk motion). The radial component is then multiplied with the spatial directional component and the result is applied to the temporal frequency plane. Best results can be achieved by applying the filter in the direction of the traveling wave. Directional filtering reduces the effects of interfering waves and produces smoother wave fields which are helpful in the inversion of MRE data to elasticity maps. Combining the shear modulus data, acquired by applying the directional filters in more than one direction yield additional improvement in the elasticity maps.

#### **2.2.4 Estimation of the Shear Modulus**

The inversion algorithms themselves can be performed using; measures of the phase gradient or spatial frequency content, direct inversions of the differential equations of motion, or iterative methods involving finite element models. These methods will be described in more detail in this section.

There are two different types of elastographic images. The images of quantities directly obtained from the tissue displacements measurements and its derivatives, like strain, displacement amplitude and vibration phase, and the images that are indirectly obtained from the displacement measurements, by using the governing equations that relate the tissue motion and the elastic properties of tissues. Although the first type of images is easier to obtain, as the images come directly from the measured displacements, the second type is more informative concerning the elastic properties of the tissue, and can reveal pathologies that are related to changes in elasticity. This type of images is obtained by estimating the wavelength of the strain waves from the acquired MRE images and elasticity parameters can be determined using an inversion algorithm.

As mentioned in section 2.1 the mechanical quantities we wish to characterize are those that relate the shear to stress (Young's modulus,  $E$ ; and the shear modulus,  $\mu$ ). To obtain these values it is important to relate them with the equation of motion.

### 2.2.4.1 Motion Equations

Stress cannot be measured in vivo and thus it is normally eliminated from the equilibrium equations. Using equation (2.2) and equation (2.3) and substituting these into the equation of motion we obtain the resulting equation of equilibrium that is given by equation (2.14).

$$\nabla \cdot \mu \nabla u + \nabla(\lambda + \mu) \nabla \cdot u = \rho \frac{\partial^2 u}{\partial t^2} \quad (2.14)$$

where  $\rho$  is the density of the material, and  $t$  is time and  $\nabla$  is a differential operator.

For harmonic deformations, which is the case used in this project, the displacement field is assumed to have a time harmonic form that is represented by a sine function as in equation (2.15).

$$u = u_0 \sin \omega t \quad (2.15)$$

where  $\omega$  is the angular frequency of mechanical motion. Substituting equation (2.15) into equation (2.14), equation (2.16) is obtained. If the medium is isotropic, equation (2.16) is transformed into equation (2.17).

$$\nabla \cdot \mu \nabla u + \nabla(\lambda + \mu) \nabla \cdot u = \rho \frac{\partial^2 u_0 \sin \omega t}{\partial t^2} \quad (2.16)$$

$$\nabla \cdot \mu \nabla u + \nabla(\lambda + \mu) \nabla \cdot u = -\rho \omega^2 u \quad (2.17)$$

Longitudinal waves contribute less for the displacement caused by the harmonic excitation so they are negligible and so  $\lambda(\nabla \cdot u) = 0$ , which simplifies equation (2.17) into equation (2.18).

$$[\nabla(\nabla \cdot u) \nabla^2 u] \mu = -\rho \omega^2 u \quad (2.18)$$

Assuming incompressibility ( $\nabla \cdot u = 0$ ) equation (2.18) simplifies to equation (2.19).

$$\mu \nabla^2 u = -\rho \omega^2 u \quad (2.19)$$

The correspondence principle states that the purely elastic equations of motion can be transformed into analogous viscoelastic equations via Laplace or Fourier transforms. Invoking this principle allows the real elastic moduli to be replaced with the corresponding complex viscoelastic parameters. In an isotropic model the real part of the shear modulus is then transformed into its complex viscoelastic analogues as follows:

$$\mu \rightarrow G^*(i\omega) = G' + iG''$$

Using the aforementioned principle we have a complex shear modulus represented by equation (2.20) in the frequency domain.

$$G(\omega) = \frac{\rho\omega^2 U}{\Delta U} \quad (2.20)$$

The complex modulus can be related to elasticity and viscosity using various rheological models. Next are described the models that are normally considered:

Voigt Model	$G(\omega) = \mu + i\omega\eta$
Maxwell Model	$G(\omega) = \frac{i\omega\eta\mu}{\mu + i\omega\eta}$
Zener Model	$G(\omega) = \frac{\mu_1\mu_2 + i\omega\eta(\mu_1 + \mu_2)}{\mu_2 + i\omega\eta}$
Jeffreys Model	$G(\omega) = -\omega\eta_1 \frac{\omega\eta_2 - i\mu}{\mu + i\omega(\eta_1 + \eta_2)}$
Fractional Zener Model	$G(\omega) = \mu_1 + \frac{\mu_2 \left(\frac{i\omega\eta}{\mu_2}\right)^\alpha}{1 + \left(\frac{i\omega\eta}{\mu_2}\right)^\alpha}$

(2.21)

They are represented by series-parallel models shown in Fig. 2.17. The higher the complexity of the model the more parameters it has. As it can be seen in the figure, while Voigt and Maxwell models require only one shear modulus ( $\mu$ ) and one shear viscosity ( $\eta$ ), the Zener and the Jeffreys model have an extra shear modulus. The fractional Zener model is an extension of the Zener model, where the dashpot component is replaced by a springpot component. A springpot represents an interpolation between purely elastic and purely viscous behaviors where  $\alpha$  is between 0 (to a spring) and 1 (to a dashpot) [35].

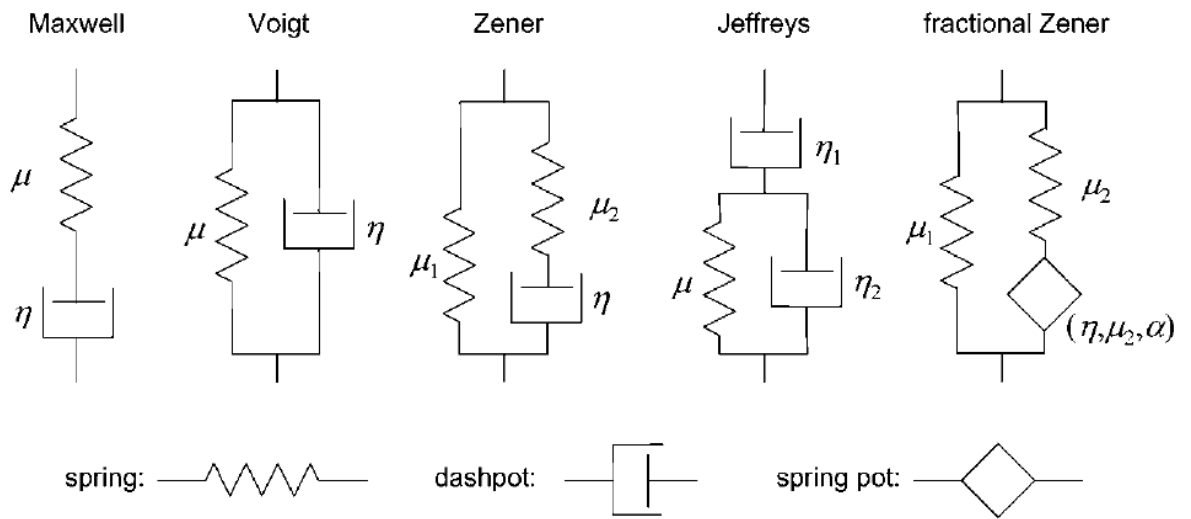


**Fig. 2.17** Representation of different rheological models. [35]

Considering that the complex shear modulus is given by the Voigt model, and if there is attenuation, the wave speed and the attenuation are given by the following equations:

$$v_s^2 = \frac{2(c^2 + \omega^2 \eta^2)}{c + (c^2 + \omega^2 \eta^2)^{1/2}} \quad (2.22)$$

$$\alpha^2 = \frac{\omega^2}{2} \frac{(c^2 + \omega^2 \eta^2)^{1/2} - c}{c^2 + \omega^2 \eta^2} \quad (2.23)$$

where  $\alpha$  is the attenuation in the direction of propagation  $k$ .

#### 2.2.4.2 *Inversion Techniques*

Some of the inversion techniques determine only the local wavelength and do not calculate the attenuation while others calculate both the real part and the imaginary part of the complex shear modulus, which can then be converted in the wave speed and attenuation. A brief review of different inversion techniques is presented below.

##### ***Local Frequency Estimation (LFE)***

This technique estimates the local spatial frequency of the shear wave propagation pattern using an algorithm that combines local estimative of the instantaneous frequency over different scales using filters. This approach considers local homogeneity, incompressibility and no attenuation and with these assumptions solves the Helmholtz equation [10]. The LFE algorithm has proven to be relatively insensitive to noise and is easily extended to 3D. However, this algorithm has limited resolution; at sharp boundaries the estimate is blurred and it is not very precise and accurate.

##### ***Phase Gradient***

The harmonic oscillation at each pixel is characterized by amplitude and a phase. If the motion is simple shear wave the quantity that is important to determine is the gradient of this phase. In other words, this method determines the change in phase per pixel that is easily convertible to a local frequency and thus to shear stiffness.

This method can have very high resolution but is very sensitive to noise. Moreover this technique is not accurate when two or more waves are superimposed or when the motion is complex. The LFE and the Algebraic Inversion of the differential equation (AIDE) methods do not suffer from this drawback as they are based on the equation of motion.



### ***Variational Method***

This method uses equation (2.14) and chooses appropriate test functions to estimate Young's modulus and the shear modulus. This algorithm avoids derivatives calculations by integrating smooth test functions over local windows in product with the data obtained. This method assumes constant  $\mu/\rho$ .

Next, the AIDE method, which was applied in the current project, will be described.

### ***Algebraic Inversion of the differential equation (AIDE)***

This algorithm uses direct inversion of the motion equations assuming local homogeneity. These equations can be solved separately using data from a local neighbourhood to estimate local derivatives at each pixel. To use the AIDE method all the components of motion are required and so equation (2.19) has to be transformed into algebraic equation:

$$A \begin{bmatrix} E + G \\ G \end{bmatrix} = -\rho\omega^2 \begin{bmatrix} u_1 \\ u_2 \\ u_3 \end{bmatrix}$$

where,

$$A = \begin{bmatrix} A_{11} & A_{12} \\ A_{21} & A_{22} \\ A_{31} & A_{32} \end{bmatrix} = \begin{bmatrix} u_{i,i1} & u_{1,ii} \\ u_{i,i2} & u_{2,ii} \\ u_{i,i3} & u_{3,ii} \end{bmatrix} \quad (2.24)$$

The Solution of equation (2.24) is given by the following equation:

$$\begin{bmatrix} E + G \\ G \end{bmatrix} = -\rho\omega^2 (A^* A)^{-1} A^* \begin{bmatrix} u_1 \\ u_2 \\ u_3 \end{bmatrix} \quad (2.25)$$

where  $A^*$  is the conjugate transpose of the matrix  $A$  and the density is assumed to be 1 for all soft tissues.

Assuming that the longitudinal pressure varies slowly, the term  $E$  can be ignored and assuming that it is an incompressible material equation (2.25) can be simplified to the Helmholtz equation which allows the determination of the shear modulus by the following equation:

$$G(\omega) = -\rho\omega^2 \frac{u_i}{\nabla^2 u_i} \quad (2.26)$$

Currently the data obtained is 2D and so, to use this method it is useful to have a 2D version of this algorithm and modify equation (2.24), setting all the derivatives in the  $z$  direction to zero.

As discussed before, the AIDE method returns the ratio of stiffness to density. Therefore, the real and the imaginary parts of this ratio can be used to determine shear wave speed and attenuation with equations (2.22) and (2.23) [49] [50].

This inversion algorithm does not depend on planar shear wave propagation, but simply on the presence of motion in the region of interest. Therefore, interference patterns like reflection and diffraction don't influence the algorithm and do not pose difficulties.

### *Solving the inhomogeneous differential equation*

In the methods specified above there are always two different assumptions to simplify the equation of motion. These assumptions are that the gradient of the hydrostatic stress is negligible and that local homogeneity exists. This simplification implies inaccurate results at or near the boundaries between regions and a limit to resolution on the order of the local window size. To overcome these problems there is the possibility of not making these assumptions and solve equation (2.14) directly, allowing the mechanical properties to vary in the physical model. This solution has two consequences: the first is that the equation remains a differential equation and not an algebraic one, and second, the fact that homogeneity is not considered does not decouple the equation of motion for shear modulus. Therefore, this approach is computationally more challenging but theoretically can more accurately model the physics of motion [51]. One of the methods used to solve the inhomogeneous differential equation is with FEM.

Van Houten et al. [52] was the first to present a FEM for solving the inversion problem of Elastography by using a least-squares minimization of the difference between measured displacement data from the MR and computed displacement solutions. The model optimization is performed on small overlapping subzones of the total tissue region of interest that are processed in a hierarchical order determined by progressive error minimization [52]. Other groups have used FE modelling of wave propagation, for example to examine the influences of shear modulus, density, Poisson's ratio and excitation frequency on shear wavelength in a gel function and also to investigate the effect of excitation frequencies and boundary conditions on shear modulus and shear viscosity in viscoelastic media [51] [53].

In this section the three main steps of the MRE process to obtain elastograms maps of the tissue were detailed including; different types of actuation devices, the physics underlying

motion measurement using MRI and the estimation of shear modulus. Finally, different inversion methods, to obtain the shear maps, used in MRE were described. Having in mind the details of each step, it is now important to give a brief overview of the clinical applications of MRE.

## **2.3 MRE CLINICAL APPLICATIONS**

Since the beginning of the MRE technique that different researchers from all over the world have been using this new imaging modality to image the elastic properties of biomaterials, engineered tissue constructs, tissue specimens and different organs (mice and humans). MRE has already been applied to brain, liver, breast, muscles, thyroid, heart, lung and spleen among other regions, and has proven to be particularly successful in the diagnosis of liver diseases. Each clinical area has its own challenge and so the MRE process will differ depending on the application. Therefore, the excitation frequency varies depending on the tissue and its location. For instance; in abdomen MRE it is common to use frequencies between 20Hz and 200Hz, in the brain frequencies in the range of 20Hz to 100Hz, in breast frequencies between 75Hz and 300Hz are used, in the lung 150Hz, in muscle 90 Hz to 150Hz, in prostate 65Hz and in thyroid 80Hz to 100Hz are typically used. In this section special emphasis to clinical application of MRE in abdomen and brain, is given and finally it will be given a brief description of other clinical applications of MRE. [54] [55]

### **2.2.1 Abdomen**

MRE was found to be very helpful in identifying abdominal diseases like hepatic fibrosis and portal hypertension. However, it is important to emphasize that liver MRE has been widely used (more than the other abdomen applications). The liver can respond to direct or indirect injury with the development of inflammation and fibrosis, which can eventually develop into cirrhosis. Liver cirrhosis is characterized by a loss of liver function as it becomes very firm and nodular. There are numerous causes of liver fibrosis including fatty liver disease, chronic viral infections, alcohol abuse, and autoimmune disorders. Studies have shown that patients with various liver diseases can reverse the impact of the disease on the liver with treatment, so, monitoring the changes of the liver is important, not only for fibrosis and inflammation staging, but also for gauging the success of treatment. Currently, liver biopsy is one of the most often used techniques to access

liver disease. Nevertheless, it is invasive. Therefore, several non-invasive imaging techniques have been developed to help diagnose and stage hepatic fibrosis. Amongst these techniques is MRE. MRE has shown a correlation between liver stiffness and the degree of hepatic fibrosis. [36] [35] [23] [56]

Yin et al. [57] [58] not only applied MRE to liver but also to other organs of the abdomen (kidney, spleen and pancreas). Fig. 2.18 shows the MRI 3-D image, the displacement data acquired in the three encoding directions X, Y and Z and lastly the elastograms reconstructed from this data. The elastogram clearly shows different elastic measurements in different regions of abdomen.

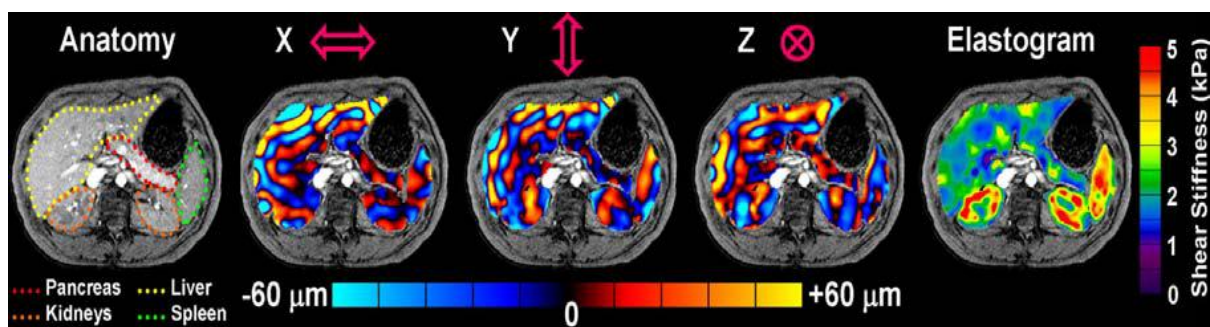


**Fig. 2.18** Slice from 3-D/3-axis abdominal MRE of healthy volunteer. [57]

Talwalker et al. [59] performed MRE on spleen and liver and found a correlation between the liver and spleen stiffness, which indicates that the mean spleen stiffness is higher in patients with liver fibrosis compared to healthy volunteers. Other groups used MRE to access liver viscoelastic properties and showed that it can clearly differentiate between normal and cirrhotic liver. [23] [35]

### **2.2.2 Brain**

Another promising recent development for MRE is the assessment of brain tissue viscoelastic properties. This knowledge is important for understanding the mechanics of brain injury, development, and pathophysiology and could provide insight to a wide variety of brain conditions. Actually, MRE can improve our understanding of diseases such as Multiple Sclerosis (MS) and Alzheimer's Disease (AD), as it gives more information about the mechanical changes of the tissue that accompany the neurodegeneration and demyelination that occur during the onset and progression of these diseases. Measuring and monitoring the mechanical properties of tumours and the surrounding brain tissue could also provide valuable information about the tumours and

their response to treatment. Despite the difficulty of penetrating the skull, different groups all over the world have already performed brain MRE and showed that is possible to measure the shear stiffness of intracranial tissues. [35] [60] [20]

Sack et al. demonstrated that the viscoelastic properties of the brain measured using MRE can be used to diagnose diffuse cerebral diseases such as AD [33] and MS [61]. They also studied patients with normal pressure hydrocephalus [62] [60]. This same group also used MRE to access and to study the impact of age and gender on brain viscoelasticity and in this study was clear that elastic properties change with age [63].

Other studies comparing the grey and the white matter stiffness have also been performed. Ehman and his group for example preformed brain MRE on 25 healthy volunteers and results indicated that white matter is significantly stiffer than grey matter as it is illustrated in Fig. 2.19 [20].

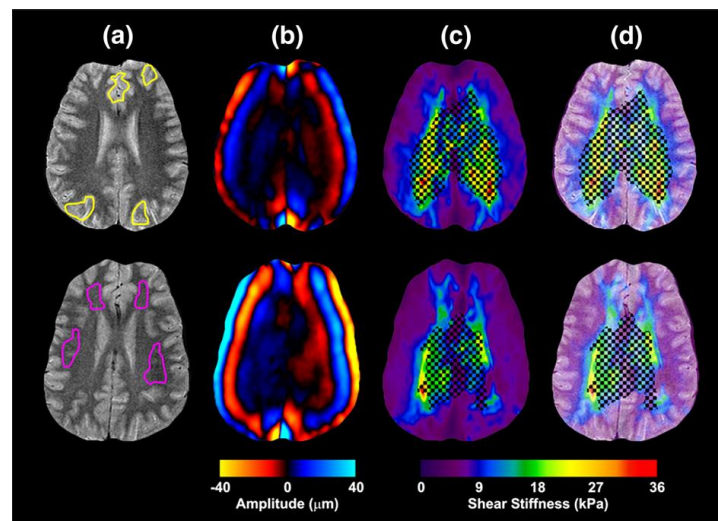


**Fig. 2.19** MRE results from two different volunteers. Differences between white matter and grey matter. a)anatomical image; b)wave propagation image; c) shear stiffness map; d) shear map overlaid on anatomical image. [20]

### 2.2.3 Others

MRE was also applied in other regions of the body as referenced before.

For instance, in breast, some studies have shown that MRE is a useful tool, diagnosing breast diseases such as cancer [54], and others showed that it is possible to separate benign from malignant lesions on the basis of their shear modulus.

On cardiac MRE Thomas et al. showed that heart functions can be determined by measuring the shear modulus variations in the left ventricle wall [64].

**Chapter 2 – Background**

Different groups also used MRE to study the elastic properties of muscles. However due to the anisotropy of the muscle fibres, advanced inversion algorithms are required. In this application MRE was used to explore the possibility of detecting taut bands and confirm their existence [65].

MRE has also been applied to other regions of the body like thyroid, lungs, and prostate among other regions.

## **3. The Piezoelectric and the Pneumatic Actuators**

Pneumatic actuators are the most widely used MRE devices for their simplicity and flexibility. However, the piezoelectric actuators are more powerful, precise and more controllable in terms of vibration frequency as described in section 2.2.1.1 of this dissertation. In this chapter, a piezoelectric actuator developed at the Institute of Medical informatics, Charité, University of Berlin, a custom-made pneumatic actuator based on Ehman's design [2] and a commercial pneumatic actuator from Mayo-Clinic, Mayo Foundation for Medical Education and Research, were used to understand the advantages and disadvantages of both set-ups.

One of the main goals of this project is to implement the piezoelectric device, already available at the WBIC, in clinical practice. To achieve this goal, the MRE hardware has to be fully understood and has to be improved, in order to be more comfortable to the patient, safe and with optimized performance.

In this chapter a detailed description of both actuators including the improvements that have been made to the piezoelectric and the methods used to develop the custom-made pneumatic actuator are presented.

The other major goal of the project was to compare both types of actuation systems. To evaluate and compare the pneumatic and piezoelectric actuation systems, two different studies have been performed: (1) motion deflection tests at different driving frequencies and different excitation amplitudes for both set-ups (for the two pneumatic actuators and for the piezoelectric actuator) and; (2) elastogram maps were obtained from a phantom and from the liver and brain, with the piezoelectric actuator and with the custom-made pneumatic actuator. In the last study, the Mayo commercial pneumatic actuator has not been used.

### **3.1 PIEZOELECTRIC ACTUATOR**

First, basic theory of the piezoelectric effect is described to better understand the principles of the piezoelectric actuator. Then, the hardware will be described and the improvements performed to it will also be presented.

### **3.1.1 Piezoelectric Effect - Basic Principles**

A piezoelectric substance is one that, when a mechanical stress is applied, produces an electric charge because the substance is squeezed or stretched. Conversely, when an electric field is applied there is a mechanical deformation (the substance shrinks or expands). To explain this effect better we have to look at the individual molecules that make up the crystal. Every molecule is polarized with one end being negatively charged and the other end being positively charged, this property is called dipole. In a monocrystal for instance the polar axes of all the dipoles lie in one direction. If the crystal is cut at any point, the resultant polar axis of both pieces will still lie in the same direction and so the crystal is said to be symmetric. On the other hand, in a polycrystal, different regions in the material have different polar axis. Therefore, there is actually no point at which the crystal could be cut that would generate two symmetric crystals so it is called to be asymmetrical.

To produce the piezoelectric effect a strong electric field is applied to the crystal, which allows the molecules to move more freely and forces the dipoles to line up. Thus, if the piezoelectric material is compressed/stretched a voltage with the same/opposite polarity as the poling voltage will appear. However, conversely, it is clear that if a voltage is applied, then the material will suffer a deformation.

This is the key concept that lies behind the operation of the piezoelectric MRE actuator. If one applies an alternating voltage, instead of a simple voltage, to a piezoelectric material, this will vibrate at the same frequency as the signal applied. As a consequence, the frequency of vibration can be controlled and modulated with a high degree of precision. This vibration will generate a displacement in the order of microns. However, with the right instruments this displacement can be amplified to some millimetres as it is going to be described in more detail in the hardware section.

### **3.1.2 Hardware**

In the previous section basic principles of the piezoelectric effect were introduced and as it was described in section 2.2.1.1, along the years different types of piezoelectric actuators were developed based on this principle. In this section, the hardware of the piezoelectric device used in this project will be described in detail as well as all the improvements that have been made to it.



The piezoelectric system consists mainly of three components:

- (1) a wave generator with an amplifier;
- (2) an active piezoelectric actuator and;
- (3) a passive actuator that is in direct contact with the target tissue.

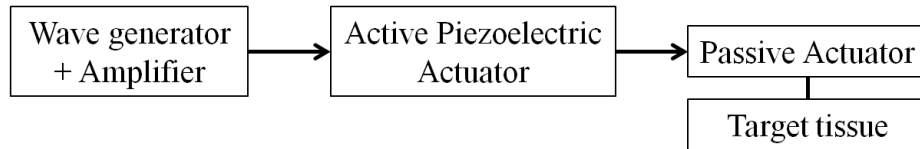


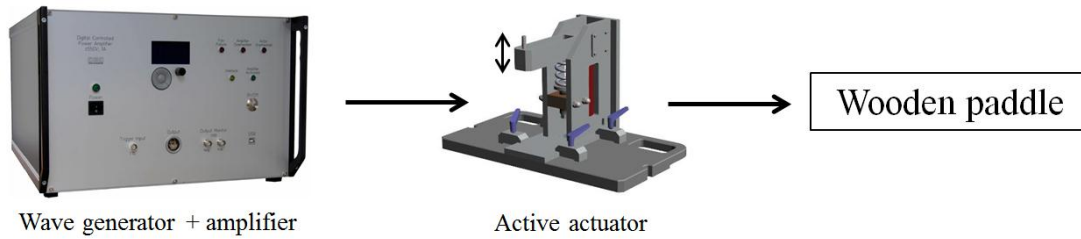
**Fig. 3.1** Schematic representation of the main components of the MRE system used in this project.

In Fig. 3.1 the three main components of the MRE system used in this project are illustrated.

The **wave generator and amplifier** enable us to generate a wave and also to control the amplitude and frequency of vibration, producing the piezoelectric effect with the amplitude and frequency desired. The wave generator and amplifier are connected to the **piezoelectric actuator** that produces the vibrations. These vibrations will be conducted to the tissue of interest by mean of a **passive actuator**, which is in direct contact with the target tissue.

This MRE piezoelectric system was developed mainly to use in brain MRE and in liver MRE. In Fig. 3.2 the main differences between both set-ups are presented. The system is the same and both set-ups work as described in Fig. 3.1. However, to activate the desired region both set-ups use different passive actuators and the active piezoelectric actuator is rotated as it is presented in the Fig. 3.2, in order to obtain the best direction of propagation in the target tissue. Differences between the two set-ups will be now described in more detail.

### Liver Set-up



### Brain Set-up

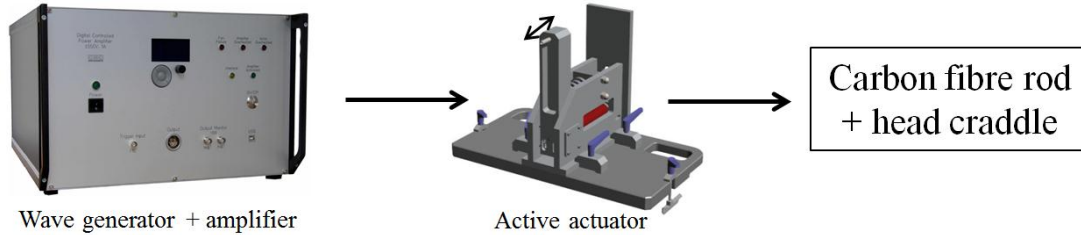


**Fig. 3.2** Schematic representation of the MRE system used in this project in two different set-ups (liver set-up on the top and brain set-up on the bottom).

To undergo mechanical excitation in a basic liver MRE exam, the subject will be placed in the MRI table; a wood stick is attached to the actuator and will be in touch with the patient abdomen, where the vibrations are propagated. The liver coil is placed above the wood stick surrounding the abdominal region of the patient (Fig. 3.3 a)).

On the other hand, to undergo mechanical excitation in a basic brain MRE exam, the subject will place his/her head inside a head cradle. A telescopic carbon fibre rod is then attached to both actuator and head cradle (Fig. 3.3 b)).

The high voltage cable that comes from the wave generator and the amplifier is then connected to the actuator (see Fig. 3.5). After the required waveform is selected, the amplifier will wait for the Transistor-Transistor Logic (TTL) signal from the scanner to trigger the excitation. The amplifier has an interlock circuit that will cut off the output if triggered by the subject.

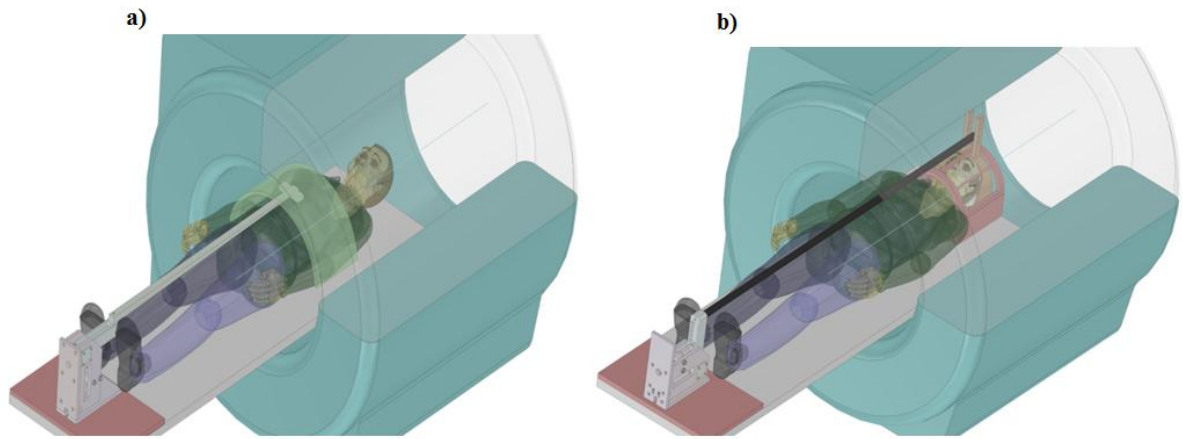


**Fig. 3.3** 3D models of the MRE system configuration for: a) liver imaging and b) brain imaging.

### 3.1.2.1 Wave form generator and amplifier

The wave form generator is the MRE component that produces the waves that are fed in the actuator to produce the mechanical excitation. It is the wave form generator that determines the type of excitation in use.

A HV-PA550-2D from CGC Instruments, Chemnitz, Germany, is currently being used at the WBIC, and is represented in Fig. 3.4.



**Fig. 3.4** Photography of the amplifier HV- PA550-2D from CGC Instruments currently in use [66].

The device is a combination of a high voltage power amplifier and a programmable digitally controlled waveform generator. The amplifier is able to provide an output power of about 1kVA to loads with a significant capacitance. The output voltage at each terminal ranges from 0 to 550 V and 0 to -550V for the positive and the negative terminals respectively.

The typical output load of the device is a piezo actor and the amplifier has been optimized to drive the actors P-035.90P produced by Ceramic GmbH. These are the piezo actors

used in the active actuator system that is described later in this section. The amplifier produces an offset voltage that equals half of the maximum amplitude for operation with the actors. If the waveform generator reaches the negative or positive maximum, the total amplifier's output voltage decays to zero or rises to 1.1 kV respectively [67].

The waveform generator can produce preferably harmonic signals or a combination of them in a frequency region of up to several kHz. The signal output can be synchronized with external instruments via the trigger input. The digital trigger signal at the trigger input starts the signal generation.

The device is designed for indoor dry laboratory use only. Moreover, it should be in a controlled temperature and humidity. To follow these rules, the device was installed in a room at the back of the magnet room, and its output is fed to a filter plate inside the RF cage. (Fig. 3.5) This room, where the wave form generator is placed cannot be accessed directly by the magnet room.

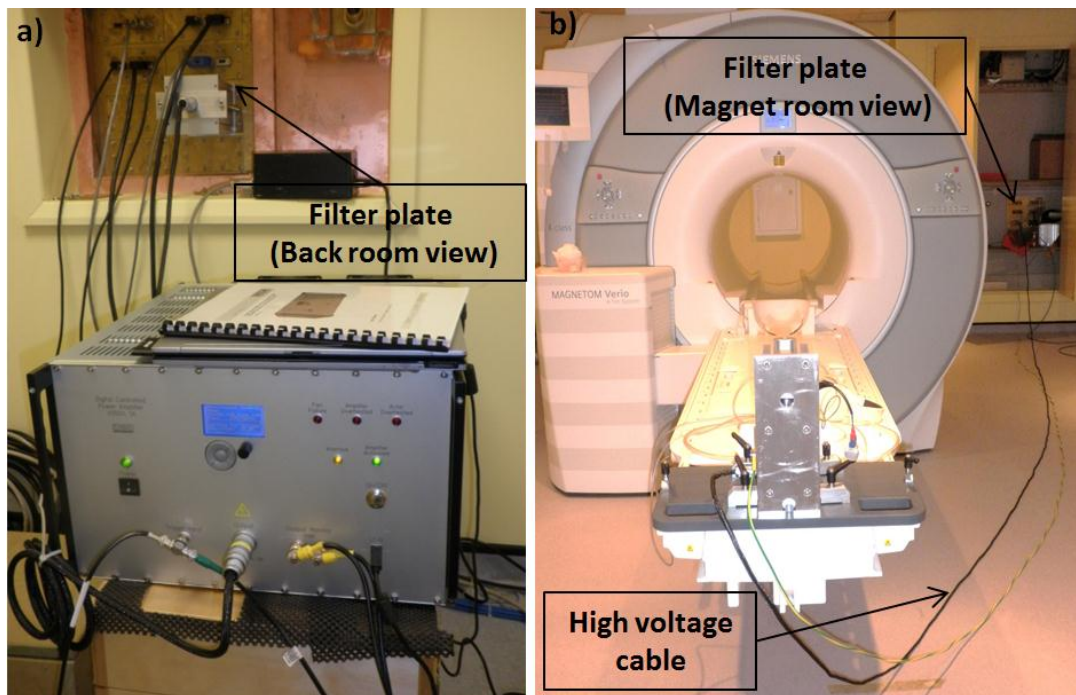


**Fig. 3.5** Connection between the waveform generator and the piezoelectric actuator. a) Wave form generator connected to the filter plate that has direct contact with the MR room; b) view of the filter plate from the magnet room and cables connection (high voltage cable identified), between the filter plate (connected to the wave form generator) and the piezoelectric actuator.

Finally, it should be mentioned that the set-up was cleared by Medicines and Healthcare products Regulatory Agency<sup>1</sup> (MHRA) to be patient safe. To get this approval, changes to the device had to be considered. These changes were:

- (1) Adding an equipotential earth bonding cable as a safety measure. If a failure of electrical insulation occurs, the bonding cable will put all the objects to which it is connected with the same electrical potential protecting the user of the equipment from different potentials;
- (2) Insulating the carbon-fibre rod (section 3.1.2.3) to reduce the touch voltage.

The standard procedures to be followed are presented in a document called MEIGaN from MHRA.

After having special considerations about patient safety, an important step of this process, it is important to consider upgrading the MRE hardware so it can become more user-friendly, easy to implement in the MR environment and being comfortable to the patient. Concerning the wave form generator, to achieve these goals, the device was remotely controlled from the computer room to be of easier access and more comfortable for the radiologist that is performing the MRE exam. This improvement was implemented during my stay in Cambridge. The wave form generator was remotely controlled and we no longer had to change MRE parameters in the back room, we could do it from the computer room.

---

<sup>1</sup> UK agency that enhance and safeguard the health of the public by ensuring that medicines and medical devices work and are acceptably safe

### 3.1.2.2 Active Piezoelectric Actuator

The active piezoelectric actuator used for liver and brain is represented in Fig. 3.6.

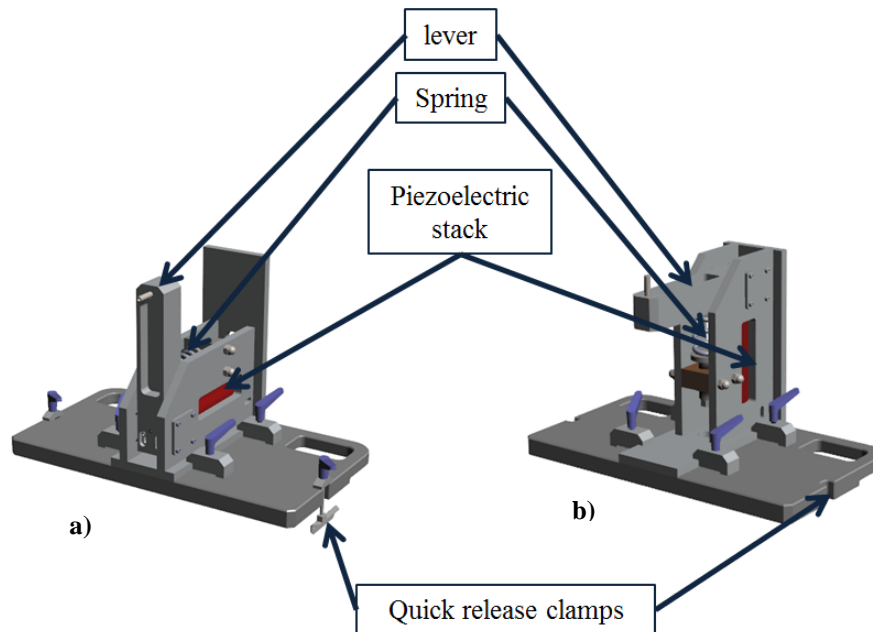


**Fig. 3.6** CAD representation of the piezoelectric actuator used: a) configuration required to induce excitation in the brain; b) configuration required to induce excitation in the liver.

More precisely, the piezoelectric actuator consists of a stack of piezoelectric crystals that expands if a voltage is applied. Consequently, if the stack is fixed between a spring and a rigid housing wall (as represented in Fig. 3.6), and the voltage is alternated, a longitudinal oscillation will be produced. In theory, this oscillation must be independent of the MRI gradients, and also if infinite force is considered, the control voltage should produce a spatial displacement relatively to the stiffness of human tissue [41]. Nevertheless, even if an ideal and optimized actuation system is used, a perfect sinusoidal excitation will not be generated because there are other factors influencing the actuation and wave propagation in the tissues. The information sheet of the piezoelectric stack is presented in APPENDIX A – Piezoelectric stack specifications.

Main characteristics of the actuator:

- (1) The actuator is placed on the scanner bed at subject's feet and is secured with two quick release clamps as shown in Fig. 3.3 and in Fig. 3.6;

- (2) the choice of a suitable piezoelectric material and its housing is very important, because it cannot disturb the imaging process of the MR scanner with susceptibility or radio frequency;
- (3) The actuator base plate is made of an insulating material;
- (4) All materials in the actuator assembly are non-magnetic and the presence of the actuator is not affecting the quality of the images acquired;
- (5) Motion is induced by coupling a rod to the lever of the actuator or a wood stick (for brain and liver MRE respectively) and by connecting it to the top surface of the tissue, as illustrated in Fig. 3.3.
- (6) The piezoceramic stack is connected to a lever that amplifies the displacement produced. The method for computing the actual displacement generated in the lever pin is illustrated in Fig. 3.7. Knowing the displacement that the piezoceramic stack produces when a voltage is applied and the dimension of the lever (225+9=234 mm), the actual displacement induced in the lever pin can be calculated  $\left(\frac{225}{9} = \frac{a}{0.13} \Leftrightarrow a \cong 3.3\right)$ . In other words, the lever, which is installed at the moment, amplifies the displacement of the piezoelectric stack 25 times. In the future, the lever should be replaced by a higher lever, in order to amplify even more the actual displacement generated in the lever pin. If for example we replace the 234 mm lever with a 409 mm lever the displacement is amplified 44 times instead of 25 times, which would improve the results considerably.

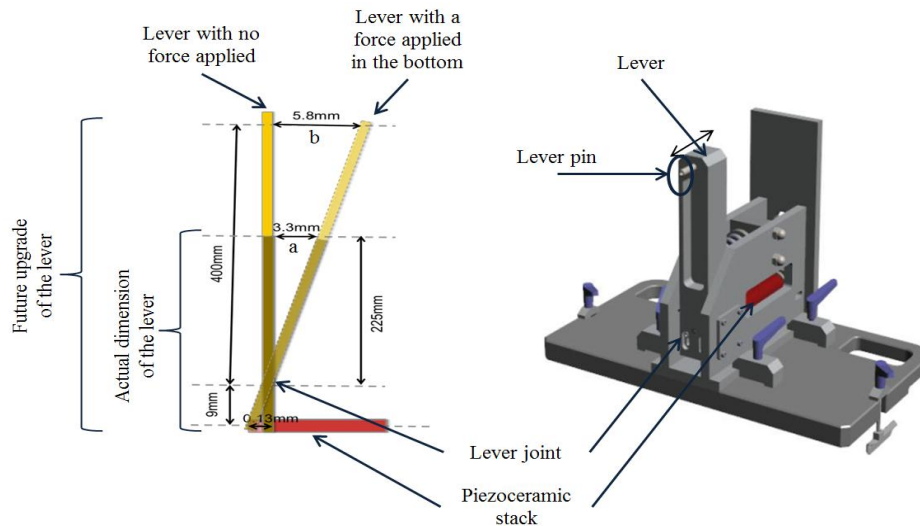


**Fig. 3.7** Measurement of the actual displacement generated in the lever pin. The piezoceramic stack induces a displacement of 0.13 mm when a voltage is applied to it. The dimension of the lever that is installed at the moment is 225+9=234 mm, so the displacement generated in the lever pin is of  $a=3.3$  mm (amplification of 25 times the displacement produced in the piezoelectric stack). In the future a lever with 400+9=409 mm will be installed and the displacement generated the piezoelectric actuator will be amplified 44 times instead of 25 times.



### 3.1.2.3 *Passive Actuators*

The passive actuators correspond to the hardware that is actually in direct contact with the tissue of interest, inducing the mechanical vibration in the tissue, but not being able to produce the vibration independently. Each application has its own challenges and so, in order to introduce the vibration in the tissue of interest it is important to consider each application separately and use different hardware designs for each. In the case of the piezoelectric actuator it can be used for liver and brain. For liver MRE a wood paddle is used to transmit the vibrations to the tissue and in the case of brain MRE a carbon fibre rod connected to a head cradle is used. These two mechanisms will be now further described.

#### ***Wood paddle used for liver excitation***

The wood paddle has 145cm of length and is fixed to the lever of the active piezoelectric actuator by one end and the other end is larger and is placed laterally (Fig. 3.8b)), right below the 9<sup>th</sup> or 10<sup>th</sup> rib to excite the liver. The body coil is placed above the wood paddle as it is shown in Fig. 3.8.

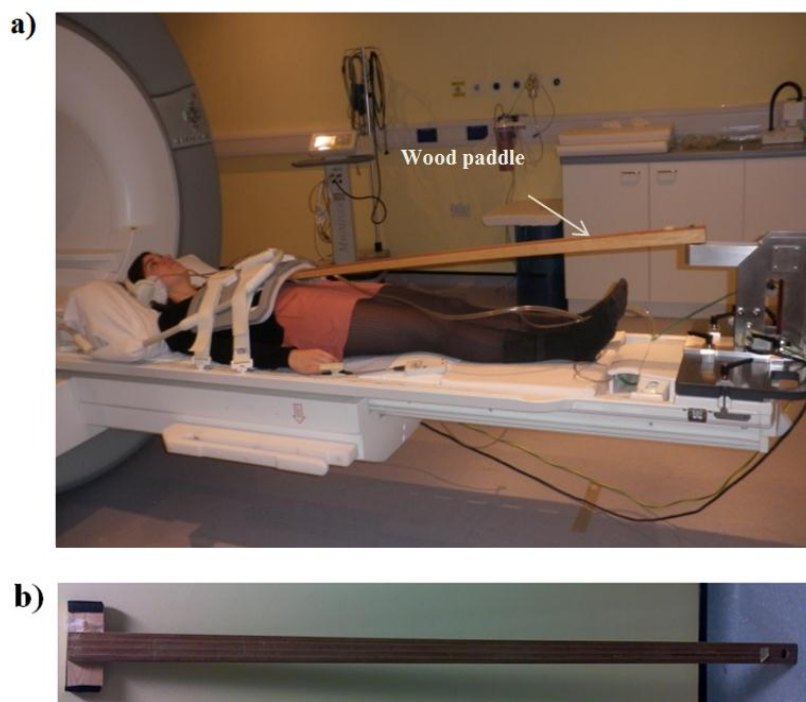


**Fig. 3.8** Liver set-up. a) all set-up; identification of the wood paddle used to induce vibrations in the liver; b) wood stick separately.



It is not an easy task to pass the barrier of fat tissue and to introduce vibrations on liver so the set-up is still not the ideal one. Moreover, it is not very user friendly and easy to use in the MR clinic. Therefore, further improvements of this set-up must be made.

#### ***Transmission rod and Head cradle used for brain excitation***

Fig. 3.9 shows the brain set-up and highlights the location and position of the carbon fibre rod and the head cradle. The head cradle suffered some changes and improvements, which are going to be described.

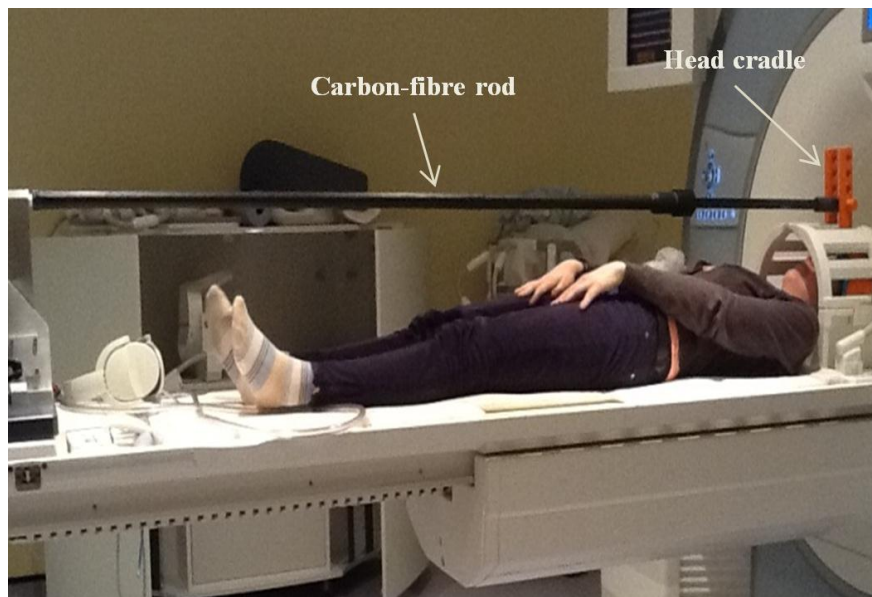


**Fig. 3.9** Brain set-up. Identification of the carbon fibre rod and of the head cradle.

The transmission rod consists of a telescopic carbon fibre tube with an external diameter of 32 mm, and an internal diameter of 30 mm. The fix tube measures 1600 mm and is extendable to 2050mm. It was manufactured by the Clinical School Workshop, Addenbrooke's Hospital. Currently, the carbon-fibre rod is fixed to the active piezoelectric actuator (Fig. 3.9), which induces a radial motion in the lever pin. When a voltage is applied to the piezoelectric stack, the lever pushes the rod with a negative angle  $\alpha$  and so the linear component along the x axis is reduced by a  $\cos(\alpha)$  (the force pushing the rod is decomposed, because the carbon-fibre rod is fix). Therefore, one of the future goals is to change the end of the carbon-fibre rod that is connected to the active piezoelectric actuator to have a circular shape (not being fixed to the lever) as illustrated in Fig. 3.10. This shape will allow for the rod to be always aligned with the x axis making  $\alpha$  zero enabling some free movement in the direction of excitation increasing the control of the parameters of excitation.



**Fig. 3.10** End of the carbon-fibre rod that connects to the active piezoelectric actuator: design of the carbon-fibre rod improved – with a pivot-type joint that enables some free movement in the direction of excitation.

The head cradle is the hardware equipment that enables the transmission of the vibrations into the skull. Therefore, its design is of utmost importance to guaranty that mechanical excitation can pass the skull barrier with maximum control and efficacy. The basic principles of the transmission of the mechanical excitation into the head cradle are schematically illustrated in Fig. 3.11. Basically, the head cradle sits on two pins that are placed and attached to a base plate that allows the head cradle to rotate inside the head coil, transmitting the mechanical vibrations into the skull through the carbon fibre rod, which is connected with the head cradle by a pin-hole hinge (on the top of it).

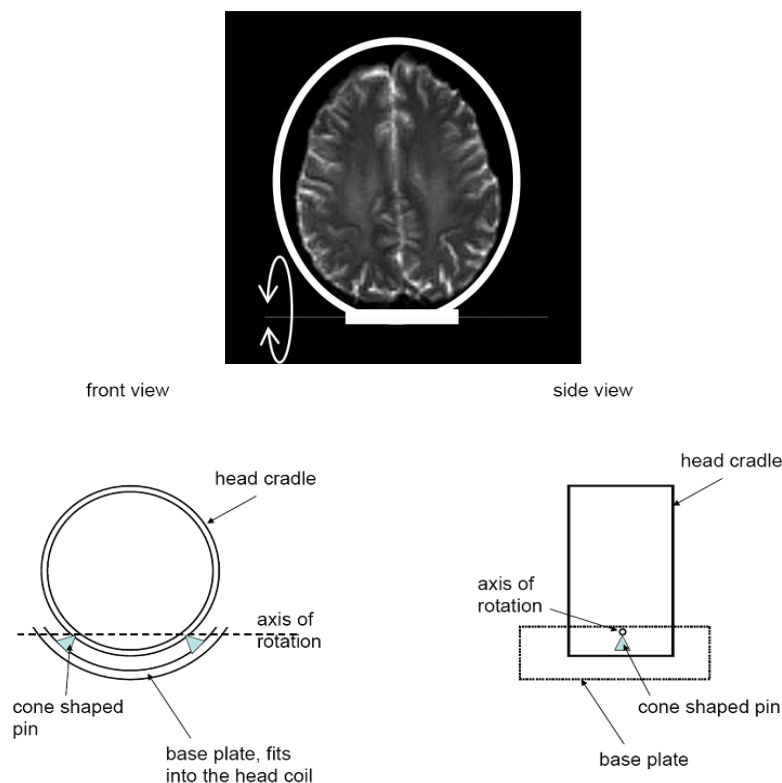


**Fig. 3.11** The head cradle (represented as a cylinder) sits on two pins attach to a base plate that allows it to rotate inside the head coil.

During this project the head cradle was improved and thus, two different head cradles were used:

- **Head cradle 1 (old head cradle)** - consists of a 6mm grey PFA sheet rolled into a 230mm cylinder. The cylinder sits on two pins attached to a base plate that allows it to rotate inside the head coil. This head cradle is illustrated in Fig. 3.12.

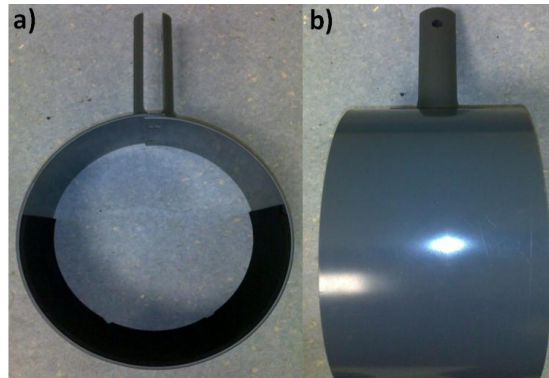


**Fig. 3.12** Photographs of the old head cradle a) front view; b) side view.

- **Head cradle 2 (improved head cradle)** – consists of extruded ABS material from the HP 3D printer. It was custom-made and it has an improved design. It is not a perfect cylinder which allows the subject to see, and it has an inflatable cuff connected to a manometer and squeezing pear allowing a personalized fixation mechanism of the subject's head in the cradle for maximum mechanical coupling and comfort. This head cradle is presented in Fig. 3.13.

All the improvements made in the piezoelectric equipment were important to increase the control of the mechanical excitation and the comfort of the patient, representing one step forward to have the acceptance of the ethics committee to implement the system in clinical practice. Moreover, it was clear that some changes in the hardware design can influence the validity and consistency of the results obtained.

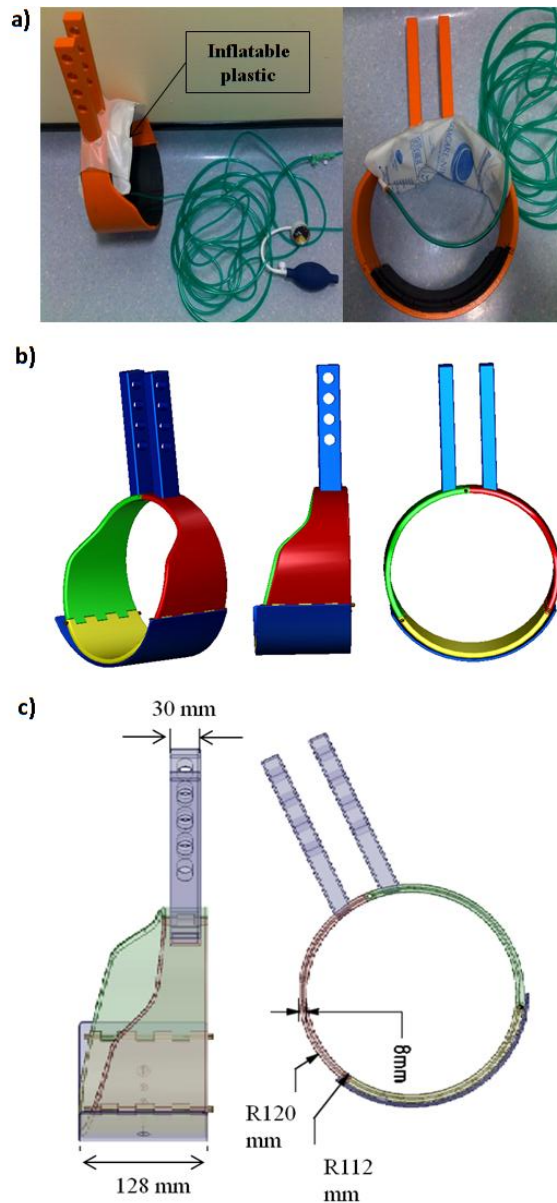


**Fig. 3.13** New head cradle used for the brain set-up of the piezoelectric system. a) Photographs of front and side view of the head cradle. The inflatable plastic for better coupling is highlighted; b) 3D modelling of the head cradle; c) dimensions of the head cradle at different views.

## 3.2 PNEUMATIC ACTUATOR

In this section the main characteristics of the pneumatic actuator developed by Ehman et al. are presented. Then, the two pneumatic set-ups used in this project are described in detail as well as their main differences.

Before understanding how sound equipment works it is very important to understand how sound waves work. Therefore, the properties of sound waves and basic principles of propagation and its importance for MRE are described next.

### **3.2.1 Acoustic Waves and MRE**

Sound waves are mechanical waves that exist as a variation of pressure composed of frequencies within the range of hearing (from about 20 Hz to 20000 Hz). They propagate through compressible medium such as solid, liquid or gas. They are created by the vibration of an object which causes the air surrounding it to vibrate and our brain interprets it as sound. More specifically, sound waves, as pressure waves have two phases: compression and rarefaction, as they propagate through the medium. The particles move only directly toward or away of the vibration source creating the compression and rarefaction zones as they propagate.

Different sound waves propagating in the same medium can lead to interference between them, and in those cases the shape of the pressure waves will combine in the medium into a complex wave form. If their amplitudes are added to one another (the compression zones of the two waves meet) the interference is said to be a constructive interference and on the contrary, if the waves are out of phase (the compression zone of one wave meets the rarefaction zone of the other wave) and their amplitudes subtract to one another, is said to be destructive interference. This property of the sound waves has to be considered carefully throughout the construction of the MRE actuation systems as it can interfere in the control of the experiment and can consequently lead to erroneous results and conclusions.

During propagation, the waves can interact with the medium and can be reflected, refracted or attenuated. The behaviour of the sound waves is generally influenced by the properties of the propagating medium such as its density and viscosity. This property of the sound waves will also influence the propagation of the waves through the soft tissue in MRE and will change considerably the results (When the waves reach fat tissue for instance, they will interact with the tissue and will be attenuated).

The basic properties of the sound waves such as its frequency and wavelength are the basic principles of the MRE actuation pneumatic systems. Sound waves generated in a subwoofer are propagated through a plastic tube into the tissue of interest. The basic properties of the propagating waves that arrive to the target tissue are then analysed. As a consequence one can obtain quantitative information about the basic properties of the medium where waves are propagating. To have a better control on this system it is important to make sure that the hardware components used don't interfere in the

properties of the sound waves that are generated in the wave generator. Moreover, the quality of the subwoofer (precision and amplification) will also interfere in the wave output and consequently in the precision of the technique.

These parameters are going to be discussed later in this section to understand what is their role and importance on determining elastic properties of the tissues with MRE.

### **3.2.2 Hardware**

Two different types of pneumatic actuators and the main principles and components of the hardware have been described in detail in section 2.2.1.1. In this project, two pneumatic actuators were used, both based on the actuator developed by Ehman and his group [68] [69] (Fig. 2.4). Motion deflection tests were carried out on both actuators and results were compared with the data obtained with the piezoelectric actuator described in the last section.

In this section the two pneumatic actuators that have been used are described in detail and the differences between them are going to be presented. By using two different pneumatic actuators with the same operating principles one can make assumptions of the influence of some special characteristics of this type of actuators, such as the power of the subwoofer and other hardware specifications. Moreover, it is possible to make assumptions and judgments about the differences in the images and data obtained with both.

In summary the two pneumatic systems used in this project are:

- ***Pneumatic actuator 1:*** custom-made system that was implemented at the WBIC MR environment to obtain measures of the acceleration and it was also tested with phantoms and volunteers for brain and liver MRE.
- ***Pneumatic actuator 2:*** Commercial pneumatic actuator (from Mayo-clinic) that was used just to obtain data for the accelerometer tests. We had access to this system because it was gently provided by Lomas and his group [70] [71] at the Addenbrooke's Hospital in Cambridge.

The two pneumatic actuators are based on the same principles and so they have a common structure (Fig. 3.14) and both consist on three main components:

- An **acoustic driver** (loudspeaker) for producing pressure shear waves;

- a **plastic tube** which acoustically couples the acoustic driver to the passive actuator (wave transmission) and;
- a **passive actuator** positioned inside the MRI system that is connected with the plastic tube and his in direct contact with the target tissue (enables tissue excitation).

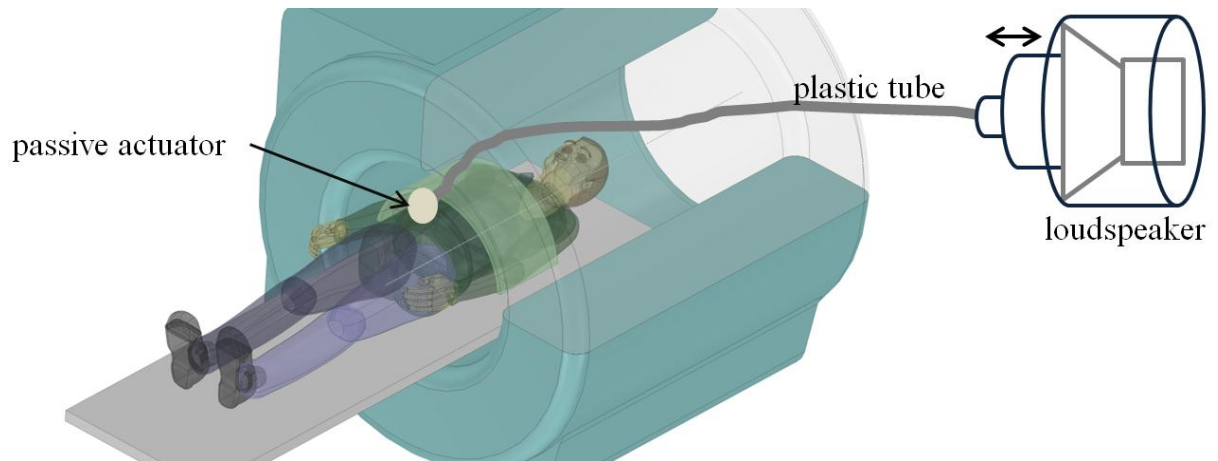


**Fig. 3.14** 3D general representation of a pneumatic device based on Ehman's design (also presented in Fig. 2.4).

In general this is a simple system to implement in the MR environment and easy to use. However, these remote actuation systems create a phase lag in mechanical motion and make it difficult to synchronize the mechanical vibration with the trigger pulse. Moreover, air is an easily compressive medium and therefore it is difficult to achieve high frequencies with this type of systems [72]. Specific properties of the subwoofer and the passive actuators change between the two pneumatic systems.

Owing to the fact that a powerful vibration with adequate displacement is necessary to guaranty optimal wave propagation into tissues, the performance of the MRE driver is directly related to: the properties of the transmit tube; the characteristics of the vibrating membrane and; the stimulating frequency and the vibrating amplitude. These specific properties increase or decrease the efficiency of the systems.

In summary, although different types of actuation devices affect the success of MRE exams it is also important to consider the properties of each device separately even if they are based on the same mechanical principles. Therefore, the Pneumatic actuator 1 and 2 are going to be described next, as well as the main technical differences between both.



### 3.2.2.1 *Pneumatic actuator 1*

Before using the commercial subwoofer from Mayo Clinic we first developed our custom-made pneumatic actuator due to its simple design, flexibility and simplicity of implementation it in the MR environment. The main components of this system are shown in Fig. 3.15.

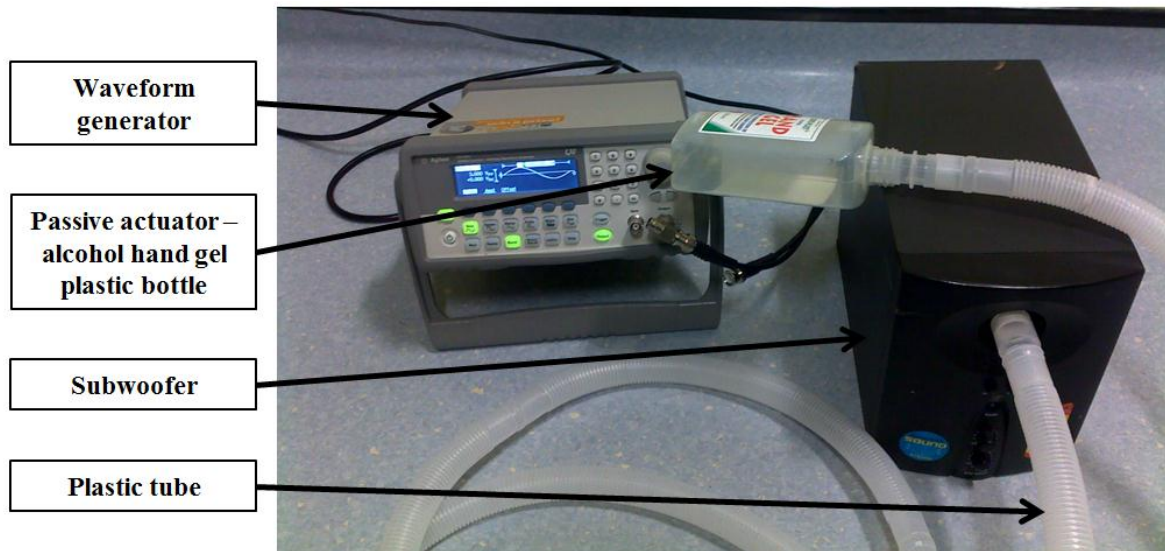


**Fig. 3.15** Pneumatic system 1 set-up. Identification of the components of the set-up.

#### ***Active Driver***

The commercial active subwoofer is driven by a function generator. Both are placed outside the magnet room, allowing a separation of the magnetic components and electronics from the scanner room to avoid any electromagnetic interference.

In Fig. 3.16 the main components of the subwoofer used in the custom-made actuator are illustrated. The rear end cone pushes the air into the speaker passing through the armature [73]. Fig. 3.19 illustrates the analogous image representing the subwoofer used in the commercial pneumatic system from Mayo Clinic. The differences between the two systems will be further described in section 3.2.2.3.



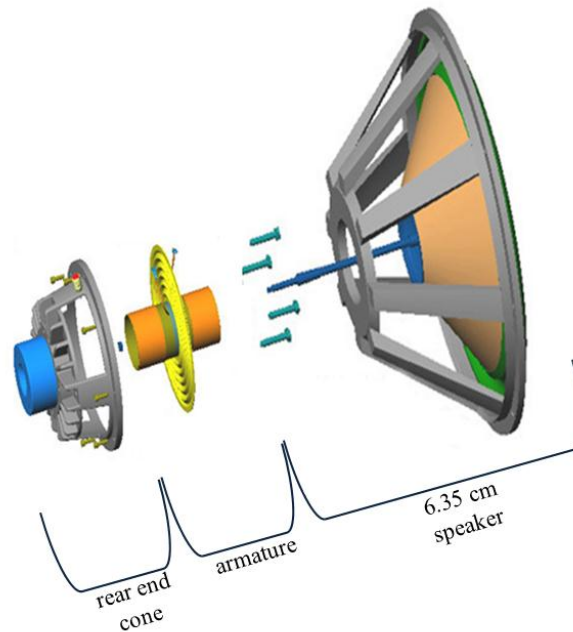


**Fig. 3.16** Schematic representation of the custom-made pneumatic subwoofer. Adapted from [74]

### ***Plastic Tube and Passive Actuator***

The sound waves produced in the loudspeaker are transmitted through a PVA hose (hospital equipment adapted) that is connected to a plastic bottle in the other end, which acts as a passive actuator and excites directly the tissue of interest (Fig. 3.15). The plastic bottle proved to be a good mean of sound waves transmission. However, due to its geometry and design it is clear that the transmission of the mechanical waves could be more efficient if another passive actuator with a specific geometry was used (for instance with the design of the passive actuator used in the comercial system –see section0). To improve the system and see if the geometry really makes a difference, we built a passive actuator similar to the comercial system in the HP 3D printer, as illustrated in Fig. 3.17, but it has not been tested yet.

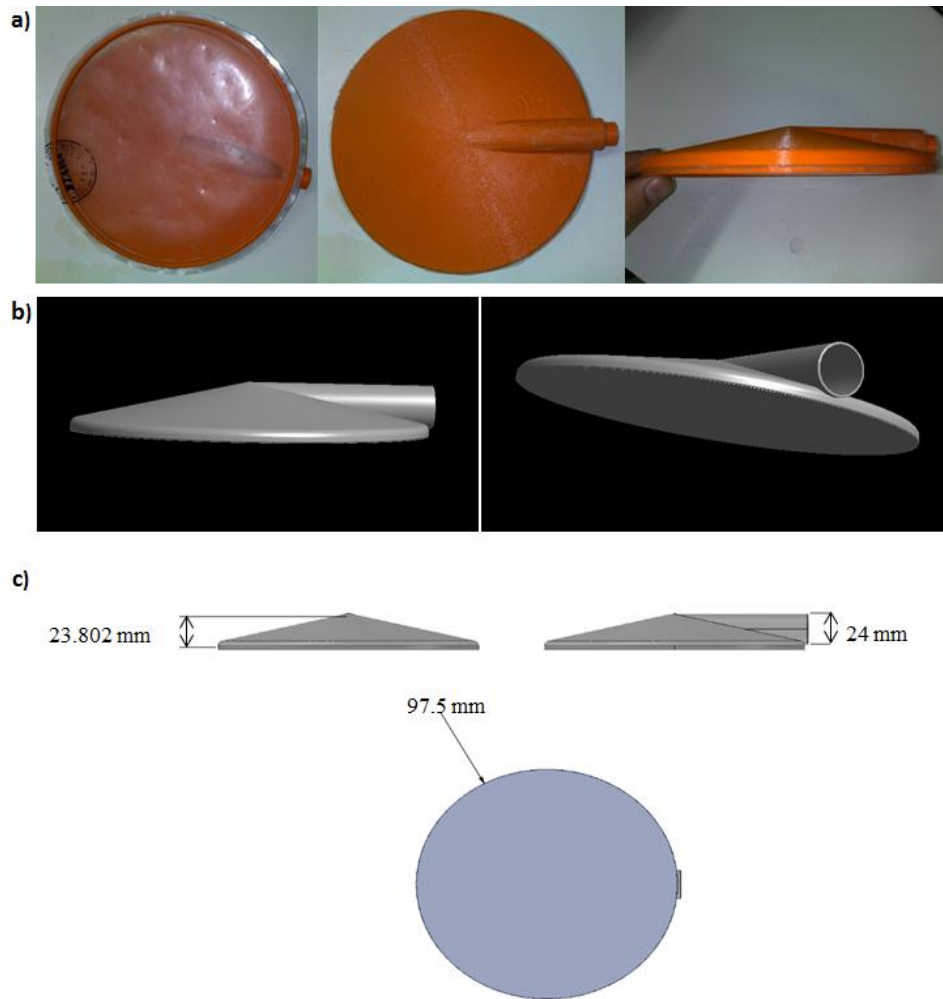


**Fig. 3.17** Passive actuator (similar to the Mayo one) built to replace the plastic hand gel bottle. a) Photographs of the flexible membrane of the passive actuator (back view) (on the left), of the rigid wall (front view) (on the centre), and of the side view (on the right); b) 3D modelling of the new passive actuator; c) dimensions of the passive actuator at different views.

The specifications of each one of the three components of the custom-built pneumatic actuator, are summarized in Table 3.1.

**Table 3.1** Technical specifications of the three main components of the custom-made pneumatic actuator developed at the WBIC.

Main Components	Technical Specifications
<b>Acoustic driver (loudspeaker)</b>	-Commercial active subwoofer with 15 Watts of power and 6.35 cm of diameter. -Low frequency response with the bandwidth of 50-100Hz
<b>Plastic tube</b>	PVA hose measuring 23mm diameter and 6m length.
<b>Passive actuator</b>	Plastic hand gel bottle.

### 3.2.2.2 *Pneumatic actuator 2*

The loudspeaker is connected to a plastic tube that introduces the mechanical vibration in the passive actuator near the tissue of interest, allowing a separation of the magnetic components and electronics from the scanner room, to avoid any electromagnetic interference. The plastic tube is sealed with a thin drum membrane which serves as periodic mechanical vibration in response to the loudspeaker. A sine signal with the same frequency to amplify the loudspeaker is generated by a Digital Signal Processing (DSP) module.

#### ***Active driver***

The system includes a remotely located active acoustic driver acoustically coupled to one or more passive acoustic drivers positioned on the subject being imaged. The device is composed of a loudspeaker cone coupled to a ported cover. This cover is constructed of a rigid material such as polycarbonate and has a thin rectangular shape (Fig. 3.18a)). The acoustic waves generated by the loudspeaker cone are directed to the passive driver via a tube (Fig. 3.18b)). Once in the tube, shear waves are projected to the subject being imaged. The motor of the active driver includes an armature and voice coils that are electrically connected to the waveform generator and amplifier and receive an alternating current. The reciprocating motion of the armature is transferred to a diaphragm that, when activated by the motor armature, produces acoustical pressure waves. Consequently, the magnitude of the acoustic pressure waves will vary by the amount of displacement of the diaphragm. This diaphragm is composed of a silicone rubber between two stiffening plates [68] [69].

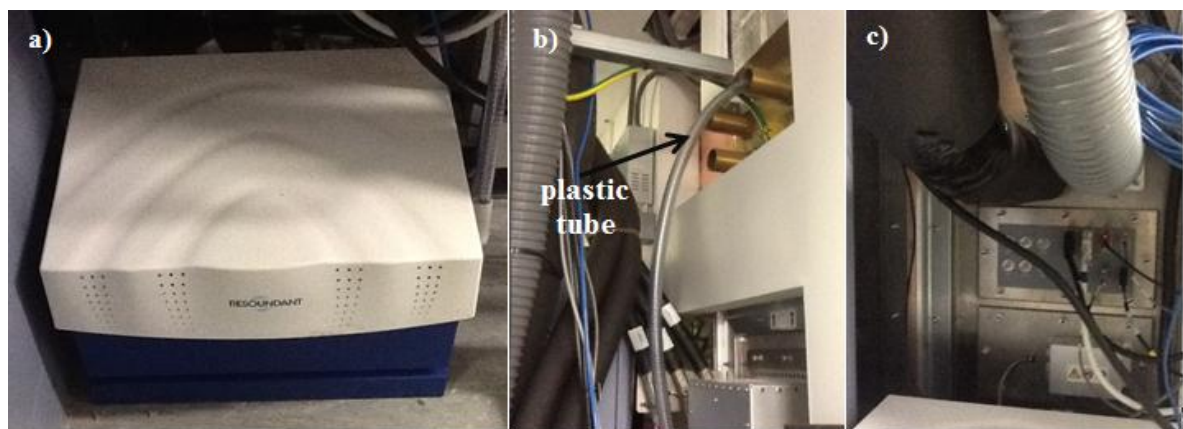


**Fig. 3.18** Components of the commercial pneumatic system from Mayo Clinic that are places outside the magnet room a)active driver; b) connection of the plastic tube with the magnet room; c)electronics plate that makes the connection of the active actuator with the magnet room and MRI system.

In other words, the active driver possesses an air compressed system. The basic principles of this air compressed system can be understood by analyzing Fig. 3.19. The illustration reveals how air displacement of the rear cone is forced through a central vent in the front cone. This "compression loading" creates the rapid air movement necessary to give the speaker "quickness" for good transient response at higher crossover frequencies. This image is the analogous of Fig. 3.16 for the subwoofer used for the custom-made pneumatic actuator.

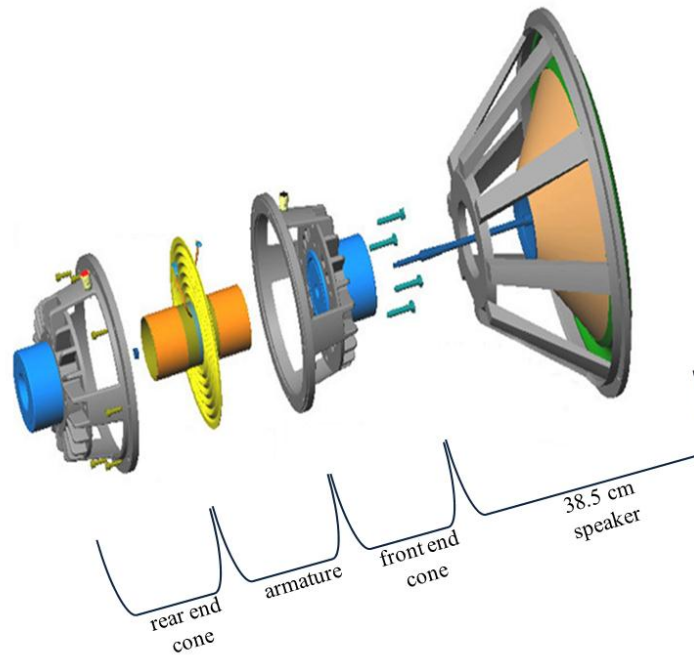


**Fig. 3.19** Representation of a subwoofer with an air compression system. Adapted from [74]

In summary the active driver was made of:

- A linear actuator with an armature that reciprocates in response to an alternating current applied to an actuator coil;
- A diaphragm mounted for reciprocating motion within the chamber and;
- A drive rod connecting to the armature to the diaphragm to cause the diaphragm to produce pressure waves directed through the tube to the passive driver when the diaphragm is stroked.

### ***Plastic tube***

The plastic tube is made of material that is flexible but not elastic. The flexibility enables it to be fed along the path between the subject inside the MRI magnet and the remotely controlled loudspeaker, that is outside the magnet room. It is non-elastic so it does not

stretch in response to the variations in air pressure caused by the shear pressure waves that propagate through the tube.

### ***Passive Driver***

The passive actuator is positioned on the subject being imaged in the MRI system and has a housing which defines a chamber and a flexible membrane which covers an opening into the chamber. A tube is acoustically coupled at one end to the chamber in the passive actuator. Stretched across the outer wall of the chamber is a flexible membrane that is normally made of a poly carbonate material but can also be made of rubber [68]. The pressure waves generated in the acoustic driver are coupled through the tube to the passive actuator chamber to cause the flexible membrane to oscillate. The membrane is positioned against the tissue of interest to apply a corresponding oscillatory force to the subject during the MRE examination. Externally, the passive driver is formed by a cylindrical outer wall and a rigid circular end wall with a hole to acoustically couple the tube to the interior chamber of the passive driver. All the spaces are completely enclosed which guarantees that the vibrations produced in the loudspeaker cone are efficiently conveyed acoustically to the flexible membrane in the passive actuator. The passive driver is presented in Fig. 3.20. [69] [12]

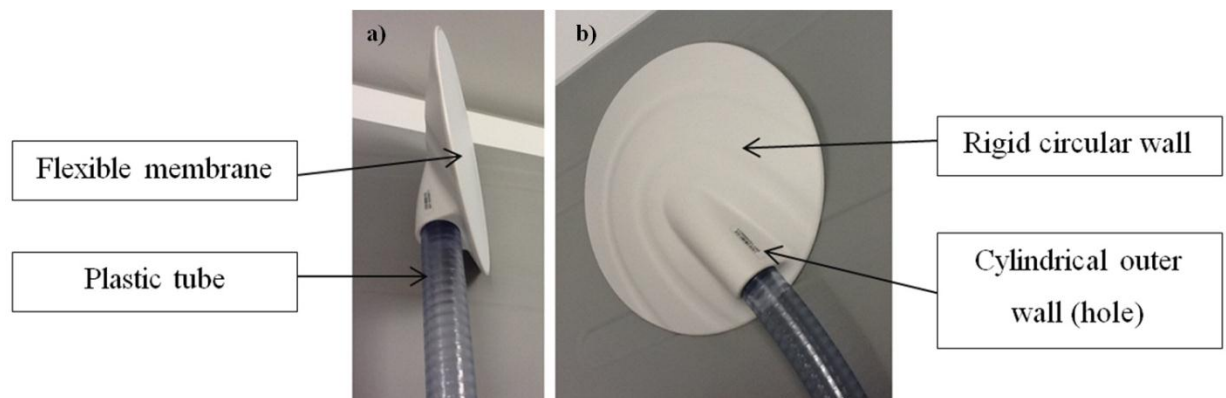


**Fig. 3.20** a) side view and b) front view of the passive actuator from Mayo Clinic, coupled to the plastic tube.

The specifications of each one of the three components of the custom-built pneumatic actuator are summarized in Table 3.2.

Magnetic Resonance Elastography: Design and Implementation as a Clinical Tool  
**Chapter 3 – The Piezoelectric and the Pneumatic Actuators**

**Table 3.2** Technical specifications of the three main components of the commercial pneumatic actuator developed in Mayo Clinic.

Main Components	Technical Specifications
<b>Acoustic driver (loudspeaker)</b>	<ul style="list-style-type: none"> <li>-38.1cm speaker manufactured by Resonant Engineering</li> <li>-The loudspeaker has low frequency response with the bandwidth of 50 -150 Hz</li> <li>- Resonant frequency of 30 Hz</li> <li>-Handle 1000 watts peak power or 600 watts rms</li> </ul>
<b>Plastic tube</b>	<ul style="list-style-type: none"> <li>-Flexible but not elastic plastic tube measuring 25.4mm of diameter.</li> <li>-Sealed with a thin drum membrane</li> </ul>
<b>Passive actuator</b>	<ul style="list-style-type: none"> <li>-Housing that defines a chamber.</li> <li>-Flexible membrane which covers an opening into the chamber that oscillates with the excitation (interior)</li> <li>- Flexible membrane that is normally made of a poly carbonate material or rubber (outer wall)</li> <li>-All spaces completely enclosed</li> </ul>

### 3.2.2.3 *Pneumatic actuator 1 Vs Pneumatic actuator 2*

As described above the pneumatic actuators used in this project were both based on Ehman's design. However, they present several differences that will influence the results obtained experimentally:

1. ***Subwoofer power:*** To promise optimal wave propagation into tissue a powerful vibration with adequate displacement is necessary. Therefore, the power of the subwoofer and its technical characteristics are properties that have a huge influence on its performance. HaiRong Zheng and his group [75] [76] performed experiments to evaluate the function of their pneumatic actuator changing the voltage and measuring the resulting displacement, and showed that higher voltages generate higher displacements. Measures of displacement were also carried out in this project and are going to be discussed in the next section. Just considering the power of both pneumatic actuators, it is expected that the pneumatic actuator 2 gives much better results and higher displacement values than the pneumatic actuator 1 (Table 3.3).
2. ***Possession of air compressed system:*** the possession of an air compressed system gives the guaranty that all the power of the loudspeaker is being used. Moreover, it improves the control of the system and its precision concerning the MRE parameters

such as the frequency and amplitude of excitation. This is another property of the pneumatic actuator 2 that the pneumatic actuator 1 does not possess (Table 3.3).

3. ***Plastic tube properties***: In the same studies [75] [76] HaiRong Zheng and his group also varied the length and diameter of the plastic tube and measured the resulting displacement. They concluded that the frequency response does not change so much when the diameter is constant and the length of the tube changes. However, it was proved that if the length of the tube remains constant and the diameter is changed it will lead to very different frequency responses, presenting maximum displacements at different frequencies. Their study also suggested that the vibration amplitude attenuates more when the diameter of the tube increases. Therefore, it is important to consider all of these factors when we are evaluating the function performance of pneumatic actuators.
4. ***Material properties and design of the passive actuators***: The design of the passive actuator will also change the frequency response of the tissue. As it was said before the plastic gel bottle has neither an appropriate geometry nor adequate material properties because there is a huge loss of energy. On the other hand, the rigid outer circular wall of the passive driver from Mayo clinic and the flexible membrane that is in direct contact with the tissue of interest, directs the mechanical excitation to the tissue with no losses increasing its control and precision.

In Table 3.3 the main differences between both pneumatic actuators concerning the properties discussed above are presented.

**Table 3.3** Comparison of some important technical specification of the pneumatic actuator 1 and 2.

Technical Specifications	Pneumatic Actuator 1	Pneumatic Actuator 2
<b>Subwoofer power</b>	- 6.35 cm of diameter - bandwidth of 50-100Hz -15 Watts of power and	-38.1cm of diameter - bandwidth of 50 -150 Hz - Resonant frequency of 30 Hz -1000 watts peak power or 600 watts rms
<b>Possession of air compressed system</b>	No	Yes
<b>Plastic tube properties</b>	23 mm	25.4 mm
<b>Passive actuator design</b>	Parallelepiped Hand gel plastic bottle with slightly concave surfaces (rudimentary).	Flat flexible membrane connected to an outer rigid wall circular chamber (all spaces are closed).

### 3.3 COMPARISON BETWEEN THE PIEZOELECTRIC AND THE PNEUMATIC ACTUATOR

In the previous section a detailed description of the piezoelectric system, used at the WBIC was given, and of the two different pneumatic set-ups that were studied and analysed in this project were also described. To compare the two types of actuators (the piezoelectric and the pneumatic systems) two different studies were performed:

- (1) **Motion Measurements:** Motion deflection tests were carried out to measure the displacement that each set-up induces on a phantom and;
- (2) **Shear Elasticity Measurements:** Elastograms of phantoms, liver and brain were obtained with both systems and compared.

In the next two sections, methods and results of these studies are going to be described and discussed.



### **3.3.1 Motion Measurement**

To understand how excitation parameters affect mechanical waves generated and how can different hardware set-ups influence MRE results we tested both pneumatic and piezoelectric set-ups by measuring the displacement that each actuator induces in the target material. The main goal was to compare the performance of the piezoelectric and the pneumatic actuators. To do that, we performed motion measurements in the piezoelectric actuator developed by the Charité group, described in the last section, and compared the results with pneumatic actuators 1 and 2 also described in the last section.

#### **3.3.1.1 *Phantoms***

Motion measurements were performed in gelatine phantoms made of dental mould. A fixed volume of the gel is warmed and the corresponding portion of water (depending if we want it to be more or less stiff) is added to the liquid gel. The mixture will then dry and will assume the shape of the container where it was poured. For motion measurements the concentration of the phantom wouldn't influence the results. Therefore, a random phantom was chosen to perform the study. In Fig. 3.21 the phantom used for the motion deflection tests is shown attached to the accelerometer.



**Fig. 3.21** Gelatine phantom attached to the accelerometer used to perform the motion deflection tests.

#### **3.3.1.2 *Instrumentation and Set-up***

To remove any bias induced by body movement, the motion deflection tests were carried out on a gelatine phantom at different frequencies and different excitation amplitudes using a commercial accelerometer (Steval MKI005V1, STMicroelectronics presented on APPENDIX B – Commercial accelerometer Specifications).

As represented in Fig. 3.23 a gelatine phantom was used and in all the different tests and experiences the passive actuators were attached to the phantom and were fixed by Velcro strips to the MRI table. Depending on the type of set-up used, the phantom was moved in

different directions of motion. Motion deflections were probed by a commercial accelerometer that was attached laterally to the phantom with tap (Fig. 3.21). The accelerometer was connected to a computer where data were sampled by Unico Lite and stored.

To summarize, in this experiment the four different set-ups used were:

**Set-up 1 - Piezoelectric actuator liver set-up:** the wood paddle was attached to the gelatine phantom, and was placed below it (Fig. 3.23a)) and the accelerometer was placed laterally in the phantom. The wood paddle vibrates up and down in the z direction.

**Set-up 2 - Piezoelectric actuator brain set-up:** the gelatine phantom was placed inside the head cradle as illustrated in Fig. 3.23b) and the accelerometer was placed laterally in the phantom. The head cradle vibrates in y-x direction. However, due to the nature of the rocket system of the head cradle the phantom will move in every direction.

**Set-up 3 - Pneumatic actuator 1:** the gelatine phantom was attached to the passive actuator (hand gel bottle) that was placed below the phantom and once more the accelerometer was placed laterally in the phantom. In this set-up the phantom will also move in every direction because the passive driver does not have a fixed direction of vibration (Fig. 3.23c)).

**Set-up 4 - Pneumatic actuator 2:** the passive driver was attached to the gelatine phantom and was placed above the phantom, in order to make sure that the flexible membrane was in direct contact with the gel. The accelerometer was placed laterally and similarly to what was described in the last set-up the phantom moved in every direction (Fig. 3.22 and Fig. 3.23d)).

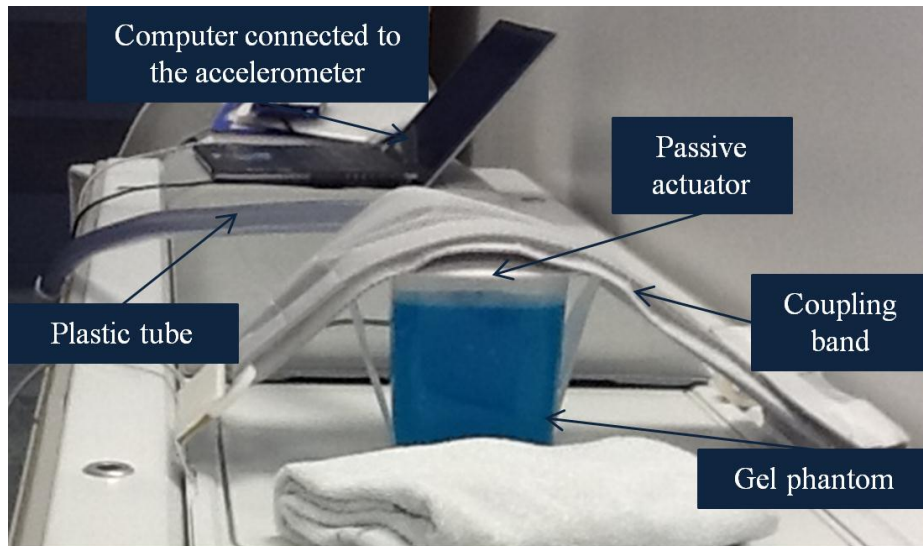


**Fig. 3.22** Pneumatic actuator 2 set-up for motion measurement. Identification of different components of the set-up.

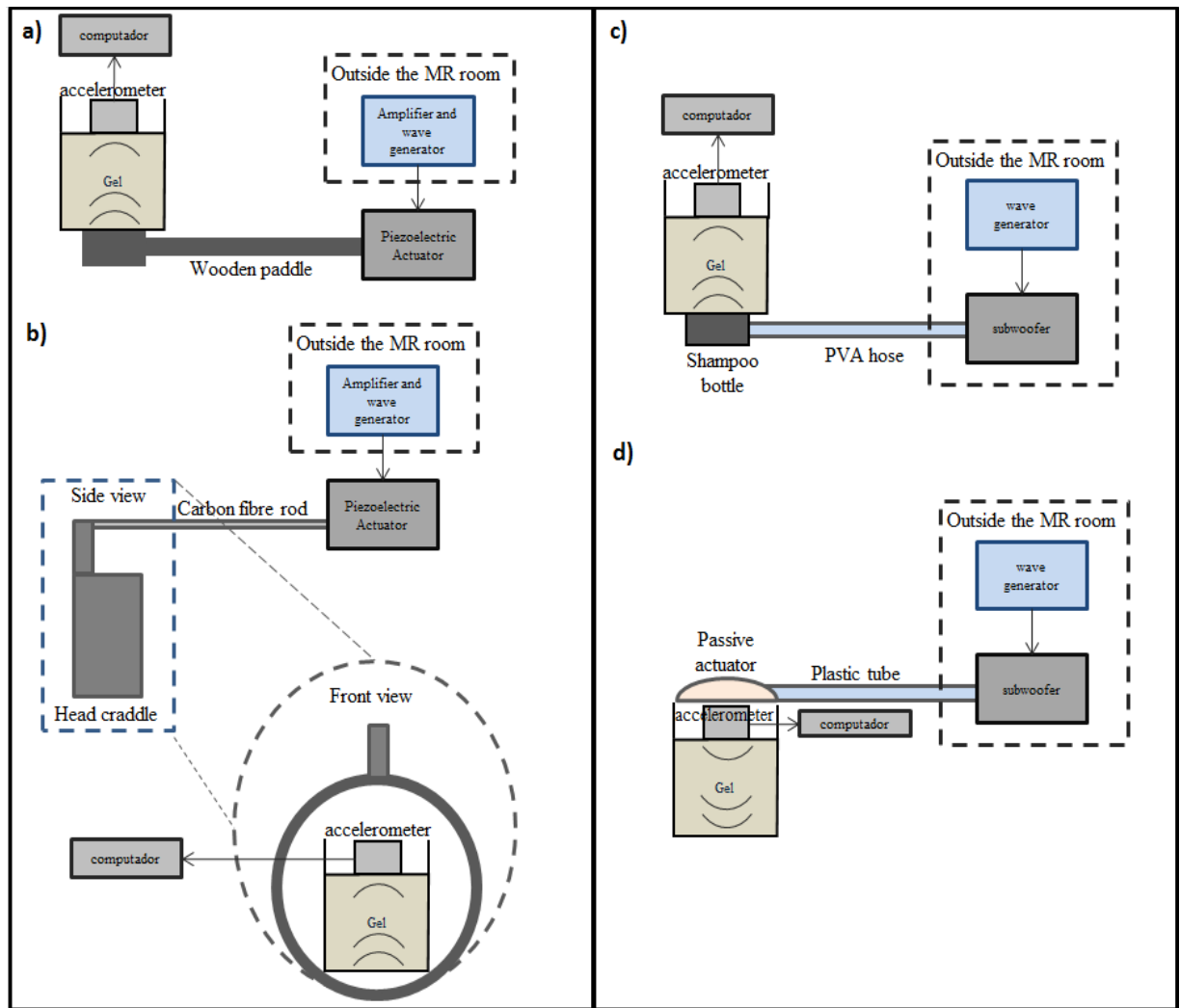


**Fig. 3.23** Schematic representation of the different set-ups used to measure acceleration with the piezoelectric system in the liver set-up (a) and in the brain set-up (b) and with the pneumatic systems (pneumatic actuator 1: c) and pneumatic actuator 2: d))

### 3.3.1.3 Accelerometer Results and Data Analysis

The main goal of this experiment was to obtain the actual displacement that each type of actuation device (piezoelectric and pneumatic) induces in the target tissue. In the last session materials and the set-up used to get these measurements were explained. Nonetheless, the raw data extracted directly from the accelerometer represents acceleration measurements. However, as referenced before, we are interested in the correspondent displacement values. To convert acceleration into displacement, data must be double-integrated. Before applying each integration step of the double integration process, data must be treated and analysed. In order to reduce integration errors and keep displacement values as close as possible to the real values, there are some data analysis considerations and steps that must be kept in mind. In this section the double integration process and all the steps that were applied to obtain displacement values are going to be described and explained.

#### 3.3.1.4 Double integration Process

Acceleration,  $a(t)$ , can be obtained by taking the second derivative of position or the first derivative of velocity (Equation (3.1))

$$a(t) = \frac{d^2x}{dt^2} = \frac{dv}{dt} \quad (3.1)$$

In order to extract displacement from acceleration measurement we need to apply double integration to the acceleration signal. To apply the double integration, initial values of position and velocity must be known (initial velocity after the first integration and the initial position after the second integration). Equations (3.2) and (3.3) describe how to obtain displacement from acceleration.

$$v(t) = v(t_0) + \int_{t_0}^t a(\tau) d\tau \quad (3.2)$$

$$x(t) = x(t_0) + \int_{t_0}^t v(\tau) d\tau \quad (3.3)$$

Analog and digital integration algorithms have been developed. Some examples of digital integration methods are the rectangular and trapezoidal integration methods that are two of the methods amongst the most used ones. However, integration methods are not the focus of this project so they are not going to be further discussed. In this project

MATLAB was used and the function *cumtrapz* (that is based on trapezoidal algorithms) was applied to integrate the data.

### ***Integration Challenges***

To measure acceleration, accelerometers are used to convert acceleration to an electrical signal. However, this conversion introduces three main challenges that have to be considered to obtain the right values for displacement: the accelerometer drift; the gravity effect that is not automatically removed in most of the accelerometers (as the one that was used in this project); and finally the use of initial conditions for velocity and position;

#### **Accelerometer Drift**

The accelerometer drift is caused by a small Direct Current (DC) bias in the acceleration signal. The vibration occurs around a fix point and as a zero mean over time. This drift and small bias can induce large errors of integration. To eliminate this problem the signal must be filtered. If no filter is applied, the output of the integration can be unbounded over time [77, 78]. Fig. 3.24 is an example of the drift effect presented in real data. This data was acquired with the piezoelectric system at 20Hz of vibration frequency. Fig. 3.25 represents the first (Fig. 3.25a)) and the second integration (Fig. 3.25b)) of the same signal, without filtering.

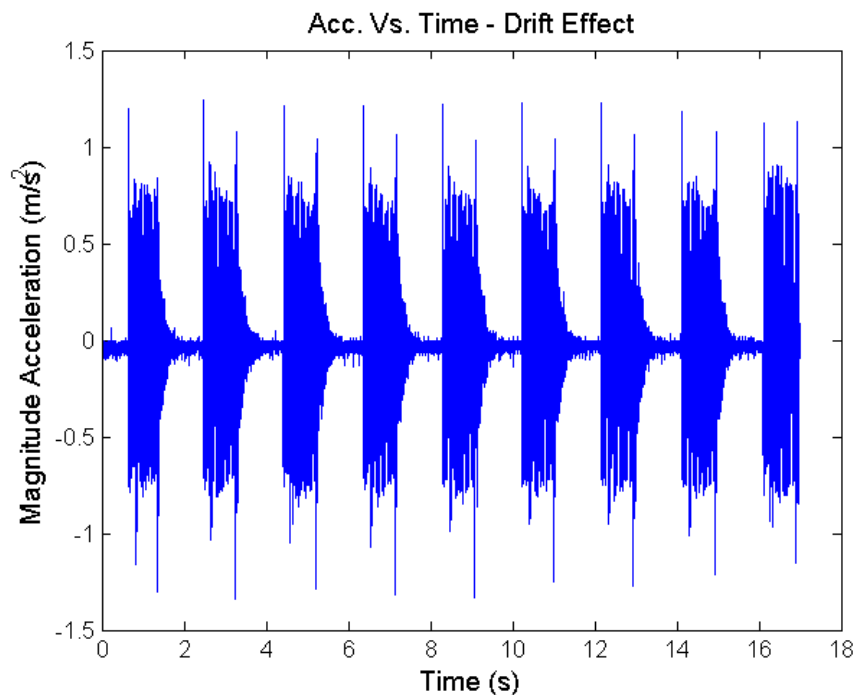


**Fig. 3.24** Acceleration signal obtained using the piezoelectric system at 20Hz of vibration frequency.

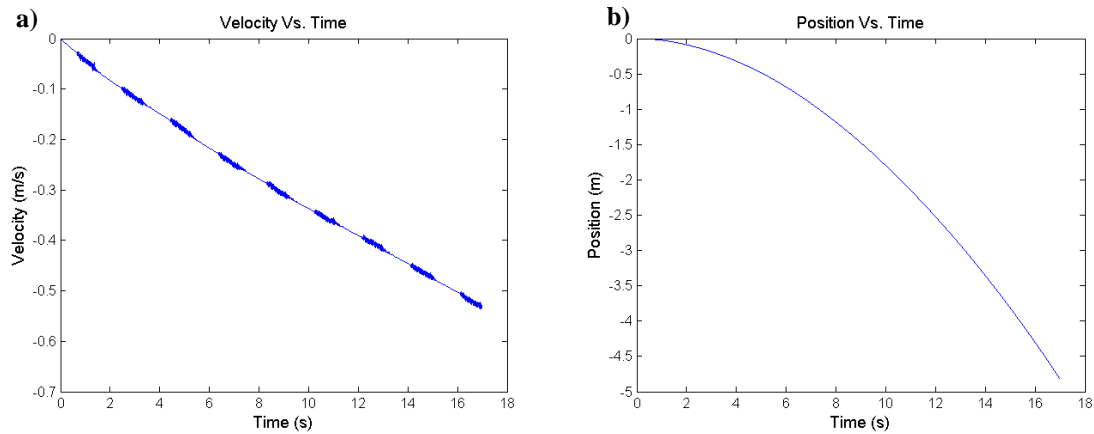


**Fig. 3.25** Integration errors due to drift effect: a) after first integration of acceleration signal (velocity); b) after second integration of acceleration signal (position).

This effect has to be minimized by the application of filters as it is going to be discussed in section 3.3.1.4.

### Gravity Effect

In parallel to the problem of accelerometer drift the gravity effect is another issue that must be eliminated. The first thought to eliminate this effect in the data is to subtract the value of gravity to acceleration measurements. However, it is not as simple as that because this effect is influencing all data and is intrinsic to it. Therefore, a simple subtraction will not solve the problem correctly. To eliminate the gravity effect high pass filtering should be used to remove the gravity component of the accelerometer signal.

In Fig. 3.26 the  $y$  component of the accelerometer measurements (component that was under the effect of gravity) is illustrated, and in Fig. 3.27 plots of the velocity and position obtained after the first and the second integration without using any filtering, are represented.

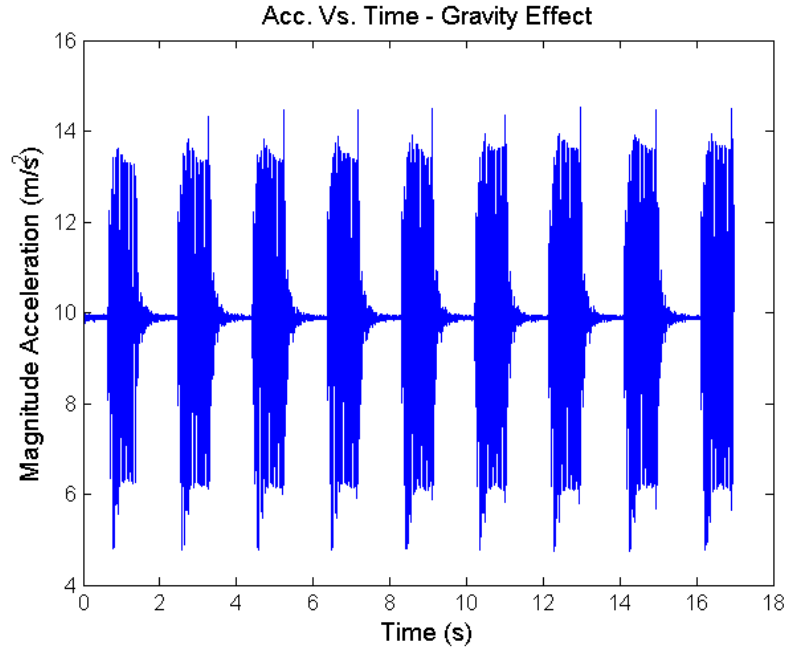


**Fig. 3.26** Acceleration measured with the gravity effect.

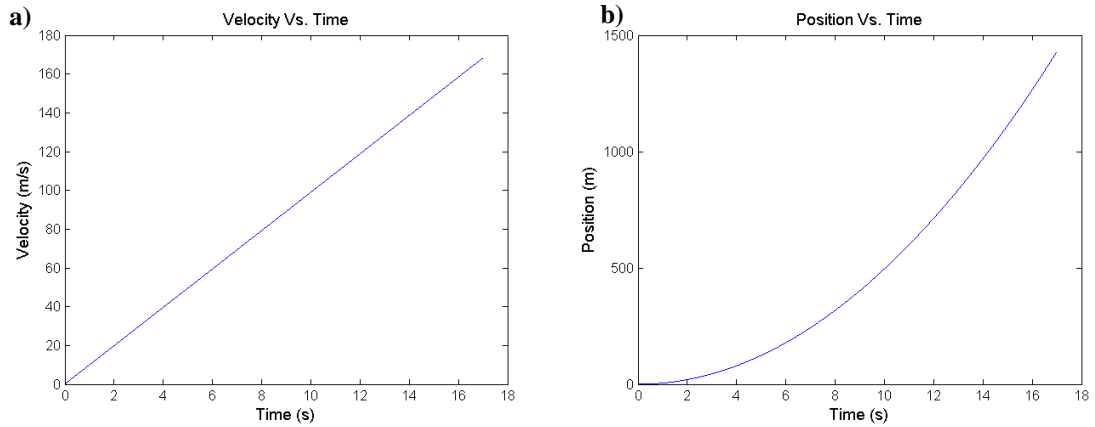


**Fig. 3.27** Integration errors due to gravity effect: a) after first integration of acceleration signal (velocity); b) after second integration of acceleration signal (position).

In this experiment all of the three components of the acceleration signal are going to be used. Therefore, the gravity effect that is presented in the y component of the data has to be removed. The solution to this problem is to use filtering as referenced before and as it will be explained in more detail in section 3.3.1.4.

### Initial Conditions

Another problem that arises from double integration is the difficulty of measuring the initial conditions, because they can only be obtained by direct measure. If the initial conditions are not used it will induce a huge error in the double integration process and will make a difference in the final result of displacement obtained (Fig. 3.29). To

overcome this problem of lack of initial conditions, it is important to use filtering. Therefore, after the first integration, to obtain velocity, a high pass filter can be used to remove that DC component of the signal again and, after the second integration to get position, the signal can be high-pass filtered as well eliminating integrating errors caused by a lack of initial conditions. To overcome this limitation *Slifka* [79] developed a method that doesn't require the use of initial conditions based on *Ribeiro et al.* [80] [77] [81]. In Fig. 3.30 is shown the double integration results with the use of high pass filters between each integration process.

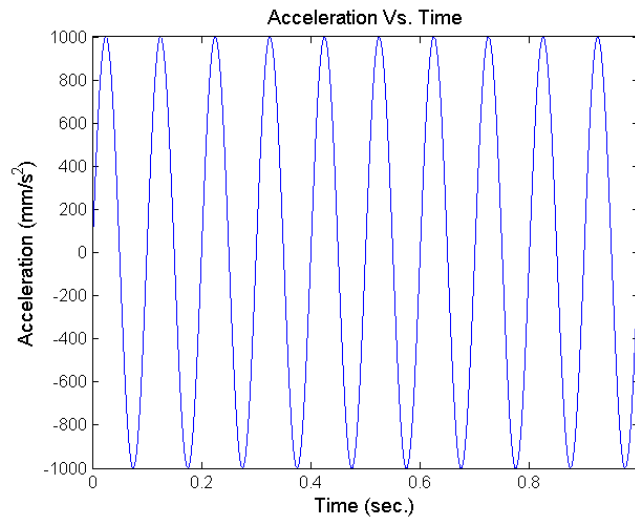


**Fig. 3.28** Acceleration without gravity effect.

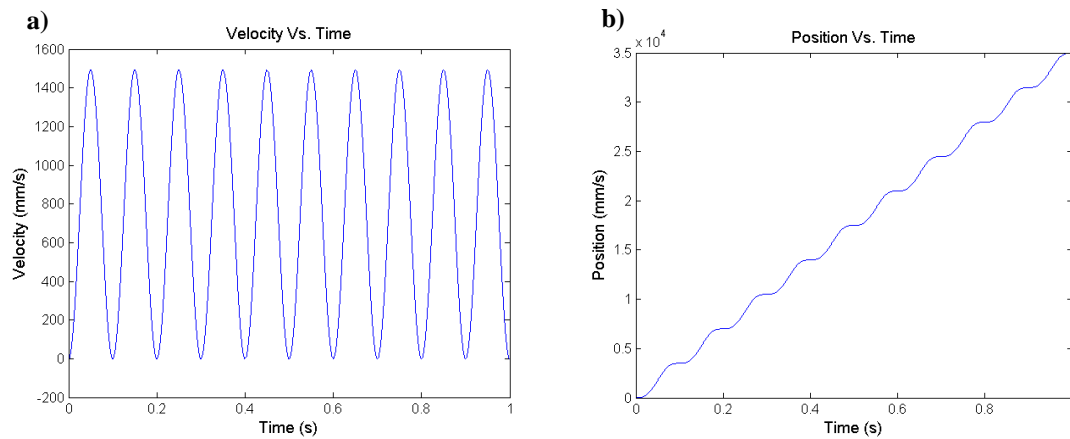


**Fig. 3.29** Integration errors due to lack of initial conditions: a) after first integration of acceleration signal (velocity); b) after second integration of acceleration signal (position).



Magnetic Resonance Elastography: Design and Implementation as a Clinical Tool  
**Chapter 3 – The Piezoelectric and the Pneumatic Actuators**

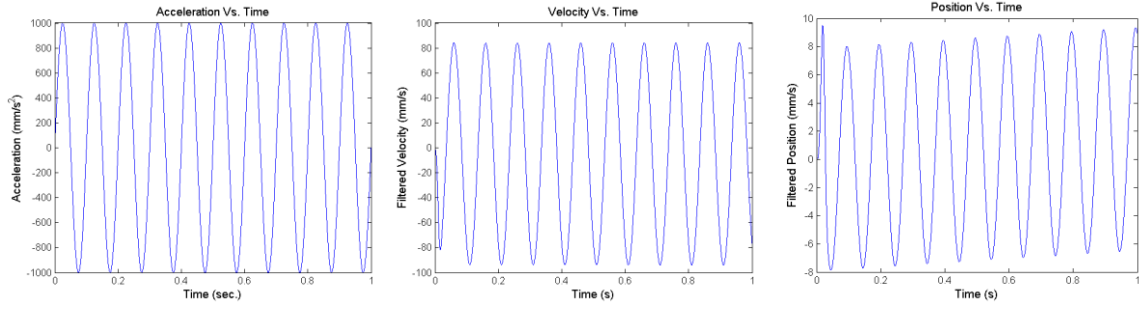


**Fig. 3.30** Double integration errors corrected by using filtering.

Three major effects that induce errors in the double integration process have been discussed and possible solutions have been suggested. In summary the double integration process to minimize the errors should be as represented in Fig. 3.31.

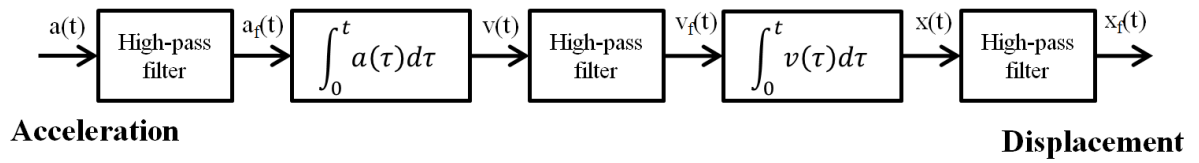


**Fig. 3.31** Block diagram of the double integration process.

The first high pass filter will remove the gravity effect and the drift effect and the other filters used in each stage of the double integration process will remove the error cause by the lack of initial conditions and by accelerometer drift(DC bias presented in the data).

In the next section three types of filtering and its advantages and disadvantages will be presented.

### 3.3.1.5 Digital filtering for Double Integration

Previous section described the need of using high-pass filtering to remove possible integration errors. The specifications of a filter are: its cut-off frequency; pass-band attenuation and; stop-band attenuation. There are three different types of filters that can be used: FIR filters, IIR filters and FFT filters. These filtering processes are going to be described next, as well as its advantages and disadvantages.

### ***IIR filtering***

To represent an Infinite Impulse Response Filter (IIR) a recursive differential equation is used (equation (3.4)).

$$a_0 y(n) = \sum_{i=1}^N a_i y(n-i) + \sum_{j=0}^M b_j x(n-j) \quad (3.4)$$

where  $y$  is the output and  $x$  is the input and the output is written as a combination of present and past inputs and past outputs. The advantage of the IIR filters regarding the FIR filters is that when it meets the same magnitude response specifications, the IIR filters will have a much lower order than the FIR filter which requires a lower computational power. The disadvantage of this type of filters is that its phase response is not as linear as the FIR's response, which means that if a signal is filtered with this filter, there will be a delay in different frequency components, causing distortion. To overcome this nonlinearity of the phase response, mathematical techniques were developed to adjust the pole locations of the filter without changing the magnitude response, but instead making the phase response linear. Another method to linearize the phase response is to filter the signal, and after time reversing the signal, filter it again with the same filter. However this will change the magnitude response and it doubles the order of the filter which is a disadvantage of this technique.

IIR filters were tested in this project but didn't gave reliable displacement measures, so the other two methods were also tested.

### ***FIR filtering***

Finite impulse response filtering (FIR) is described by equation (3.5):

$$y(n) = \alpha_0 x(n) + \alpha_1 x(n-1) + \alpha_2 x(n-2) + \dots + \alpha_{N-1} x(n-(N-1)) + \alpha_N x(n-N) \quad (3.5)$$

where  $y$  is the output and  $x$  is the input. As it can be observed from the previous equation the output of the FIR filtering process is simply a linear combination of the input and  $N$  is the order of the filter. These filters have the advantage of having a linear phase response. Nevertheless, the order of the filters has to be really high which lead to the necessity of having access to a very high computational power.

To minimize acceleration drift described above, Ribeiro [77] proposed a high-pass digital FIR filter with a cut-off frequency of 0.9Hz and frequency response shown in Fig. 3.32.

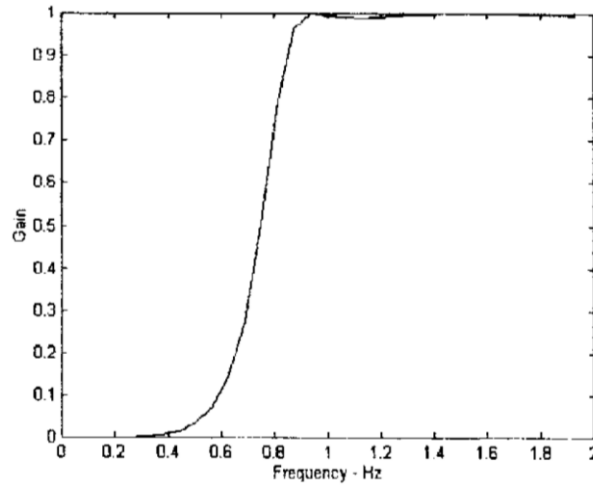


**Fig. 3.32** Frequency response of the high-pass FIR filter proposed [77].

The filtering process proposed [80] can be described by the following steps:

1.  $X = FFT(x)$ ;
2.  $X_f = X * H$ ;
3.  $x_f = IFFT(X_f)$ ;

where,  $X$  is the Fast Fourier Transform (FFT) of the signal  $x$ ,  $X_f$  is the FFT of the filtered signal, which consists on the multiplication of the FFT of the signal by the filter gain,  $H$ . the inverse FFT of  $X_f$  is the filtered signal desired.

This type of filtering was tested in this project in an attempt to improve the performance of the double integration process. This process removes the zero shift induced by the drift. However, it has the disadvantage of inducing an error (distortion) at the first second of the measurements, as illustrated in Fig. 3.33.

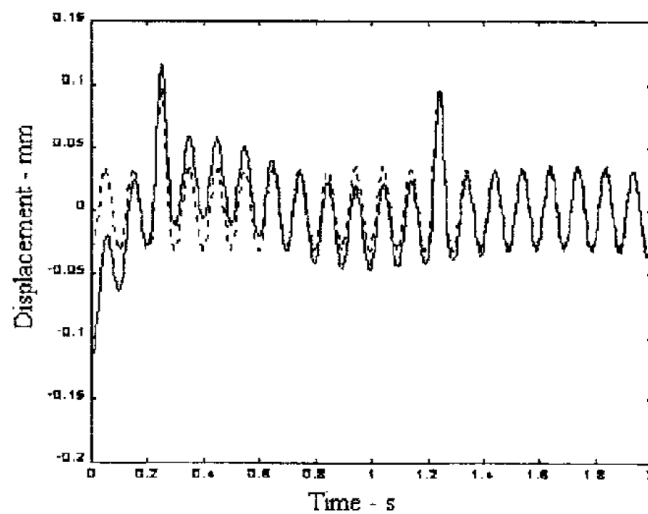


**Fig. 3.33** Integration error when a FIR filter is used. [77]

To minimize this error the signal can be truncated in the time domain reducing the error to the first milliseconds of the signal. Nevertheless, this procedure will remove information from the signal which is undesirable.

### ***FFT filtering***

Because of the time aliasing problem, Ribeiro [81] proposed another filtering method to remove this error. In this process the FFT is applied to the signal and then the value of frequencies below 0.7 Hz are made constant. To be well succeeded this process implies that the signal must be sampled for at least 4 s and despite the sample rate not being a problem, higher sample rates means higher resolution in time.

In basic steps the FFT filtering process is made in the raw acceleration signal. The signal is then integrated to obtain velocity, after obtaining velocity the signal is FFT filtered to be integrated and to obtain displacement. Finally the signal is FFT filtered again. The whole filtering process was called FFT-DDI method by the authors and can be summarized as follows:

1.  $X = FFT(x);$
2.  $X_f = X;$
3.  $X_f(1) = X_f(3);$
4.  $X_f(2) = X_f(3);$
5.  $X_f(2047) = conj(X_f(2));$
6.  $x_f = IFFT(X_f);$

The third element of the FFT is chosen because it corresponds to a frequency of about 0.7 Hz. Moreover, the size of the FFT is often set to a power of 2 (2048) because it is more efficient computationally. However, this method seems to work well only with a single frequency signal. LSlifka [79] showed that when a random signal is used the cut-off frequency of 0.7Hz doesn't remove frequencies that come from the accelerometer drift. To overcome this problem, LSlifka proposed a modification to the FFT-DDI Ribeiro's method which significantly improved the analysis, when considering a multiple frequencies signal. Ribeiro's method and LSlifka modifications were both implemented in this project, and the modifications performed by LSlifka were adapted, in order to give reliable results in this study in particular. The modifications implemented in the process are listed below:

1. increase the cut-off frequency of 0.7 Hz to 10 Hz to remove the drift;
2. Just the real part of the time-domain filtered signal, after performing the IFFT, must be considered and the imaginary part must be discarded;

The FFT process was then rewritten as:

1.  $X = FFT(x);$
2.  $X_f = X;$
3.  $X_f(0) = \alpha_0 X_f(k);$
4. for  $i = 1:(k-1)$   
 $X_f(i) = \alpha_i X_f(k); X_f(N-i) = conj(X_f(i));$
5.  $x_f = Real(IFTT(X_f));$

where N is the size of the FFT, k is the index number of the FFT coefficient that represents the cut-off frequency and  $\alpha_i$ 's are filtering coefficients specified by the user. For this project this algorithm was used to obtain displacement values through acceleration measures. After implementing other filtering techniques it was concluded that this algorithm was the one that gives less integration errors and more reliable results.

### 3.3.1.6 Accelerometer Results

In this section all the results obtained with the accelerometer will be presented, as well as the conclusions about the comparison of different type of set-ups and their reliability in clinical practice.

#### *Acceleration Analysis*

Acceleration measurements were obtained as described in section 3.3.1.2 of this dissertation. For the piezoelectric set-up the sinusoidal signal from the wave generator was set to 40% and then to 75% of its total power (which corresponds to 1.1kV), for the Mayo set-up the waveform generator was set for 30V and for the custom-made pneumatic set-up it was set to 5V. In Fig. 3.34 the acceleration signals for five different vibration frequencies for three different set-ups: the piezoelectric liver set-up; the custom-made pneumatic set-up and; the commercial Mayo Clinic pneumatic set-up, are illustrated. Analysing these signals it is clear that both the piezoelectric and the Mayo set-up are less noisy and more powerful than the custom-made pneumatic set-up. This result was expected due to the materials and the primitive design used to build the custom-made pneumatic set-up. Moreover, it should be pointed out that the acceleration measurements

obtained with the piezoelectric and the commercial Mayo set-up are consistent and prove the reliability of the MRE method.

It is also important to understand which properties of the signals will induce integration errors. There are two signal properties that must be carefully analysed: (1) the noise presented in the signal; and (2) the time of vibration without interruption. As discussed before, the acceleration signal of the custom-made pneumatic set-up is noisier than the other two set-ups so probably it will induce more errors in the double integration process. The time of vibration without interruption is important because the filtering process will always cause some errors at the beginning and at the end of the signal thus, if the vibration signal takes longer, the displacement signal extracted will present less errors. As illustrated in Fig. 3.34 the acceleration measurements of the Mayo set-up were obtained continuously, which will induce less errors of integration in the double integration process.

# Magnetic Resonance Elastography: Design and Implementation as a Clinical Tool

## Chapter 3 – The Piezoelectric and the Pneumatic Actuators

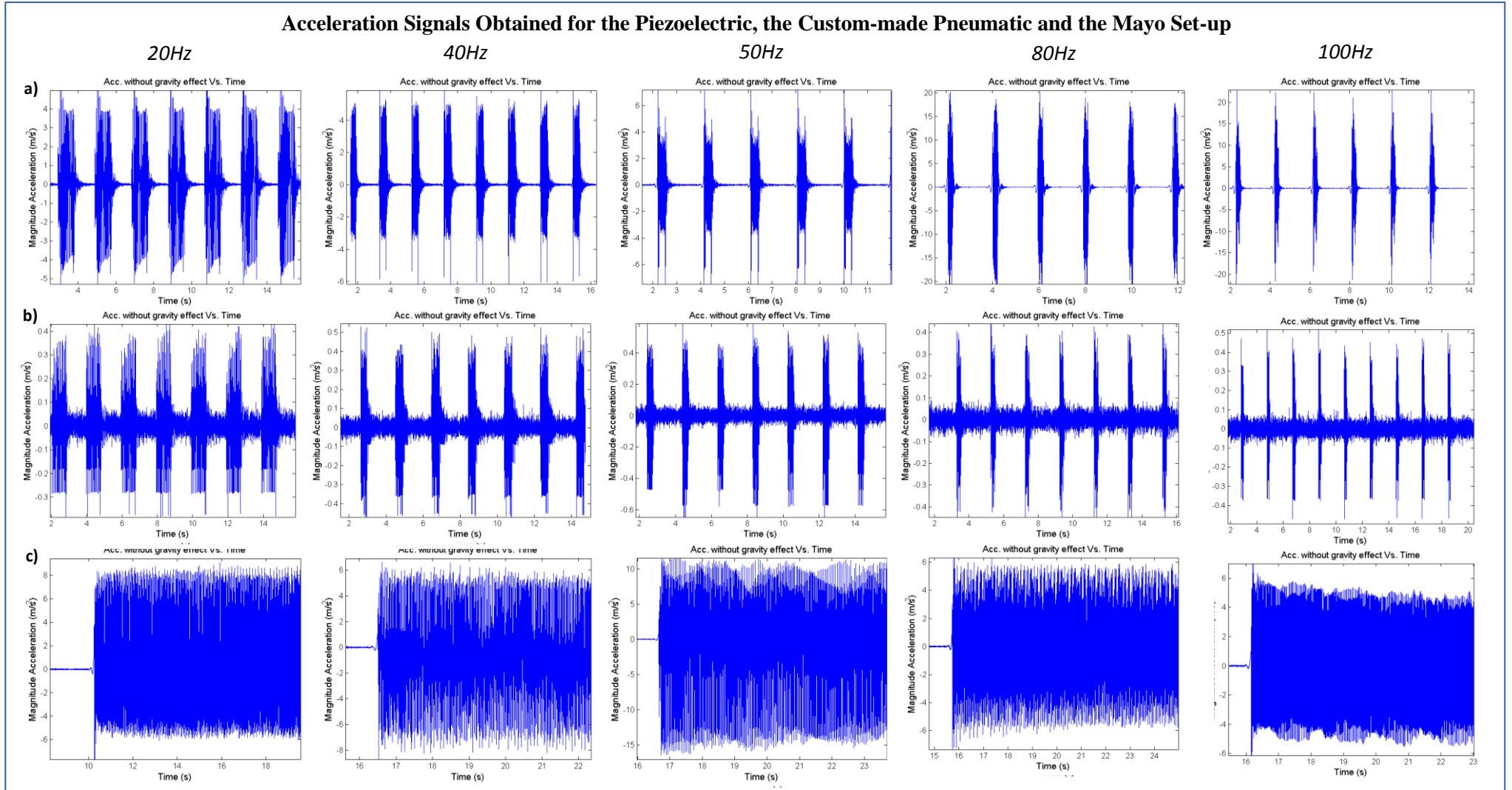


**Fig. 3.34** Acceleration signals obtained with three different setups: a) the piezoelectric liver set-up; b) the pneumatic custom-made set-up; and c) the commercial Mayo Clinic pneumatic set-up, at 5 different vibration frequencies (20, 40, 50, 80 and 100Hz).

### Displacement Analysis

The acceleration measurements were then introduced in the double integration process as described in Fig. 3.31. Velocity and displacement measurements were obtained for each set-up and for each vibration frequency.

After analysing each velocity and displacement signal individually to understand if there were large integration errors that could be eliminated, the magnitude peak-to-peak displacement values were calculated for each vibration frequency and for each set-up as shown in Fig. 3.35. Owing to the fact that it is not certain that the phantom vibrates only in the direction of the passive actuator, for all the cases the magnitude of the acceleration signal was considered instead of considering one particular direction.

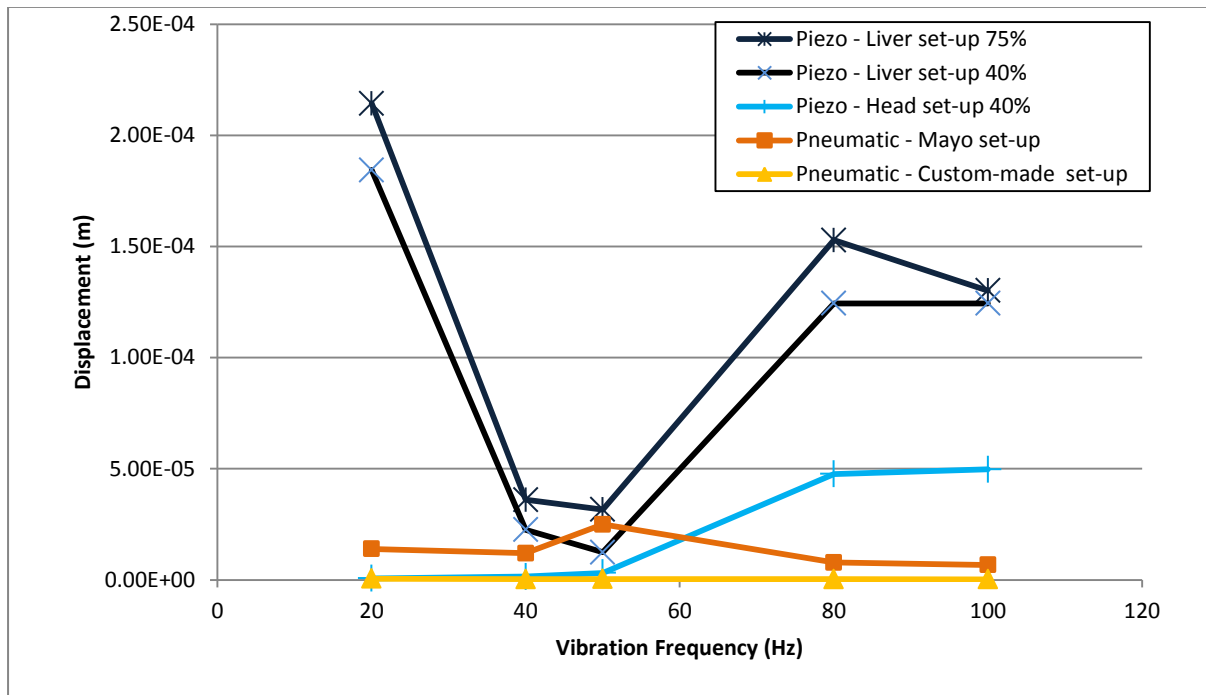


**Fig. 3.35** Magnitude peak-to-peak displacement values for both set-ups of the piezoelectric actuator (liver and brain set-up) with different waveform amplitudes (40% and 75%) for the custom-made pneumatic actuator and for the commercial Mayo Clinic pneumatic actuator at five different vibration frequencies (20, 40, 50, 80 and 100Hz).

Fig. 3.35 shows that the results obtained for the custom-made pneumatic device present very little displacement compared with the other set-ups. Therefore, in order to better evaluate the displacement curve obtained for the custom-made pneumatic set-up, this curve was isolated in Fig. 3.36.



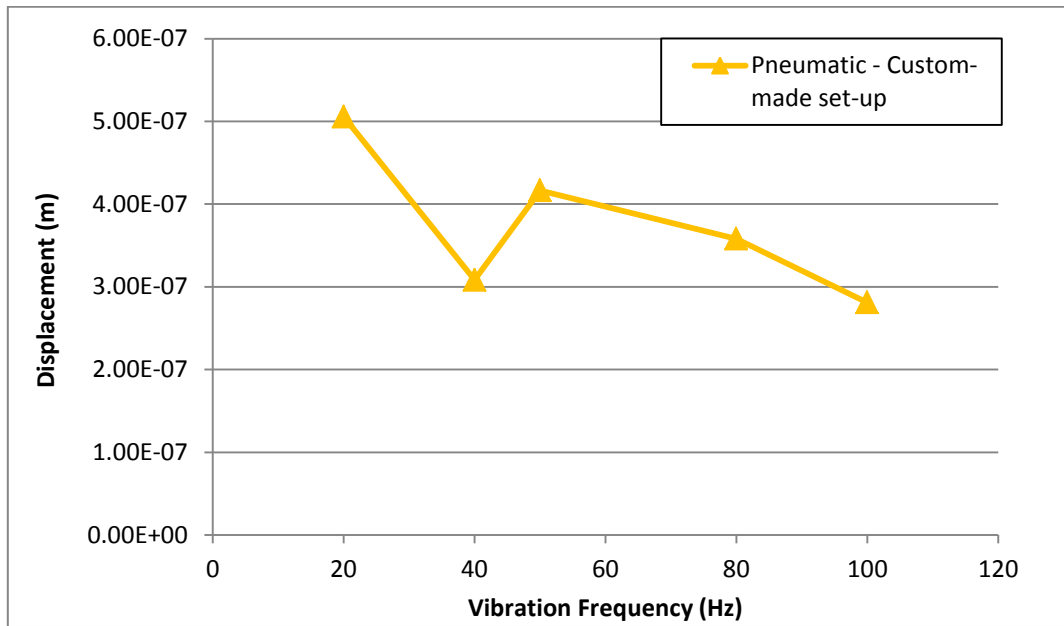


**Fig. 3.36** Magnitude peak-to-peak displacement values for the custom-made pneumatic actuator at five different vibration frequencies (20, 40, 50, 80 and 100Hz).

Analysing Fig. 3.35, it is clear that the piezoelectric setup proved to be more consistent comparing the results at 40% and 75% inducing a higher displacement at 75%, as expected. Moreover, it proved to be more powerful at frequencies surrounding 20Hz and at higher frequencies (80 and 100Hz), presenting similar results as the commercial pneumatic actuator from Mayo Clinic at frequencies surrounding 40 and 50Hz. These results proved the consistency and reliability of both the piezoelectric and the Mayo set-up [55]. Concerning the displacement values obtained for the piezoelectric actuator head set-up, it proved to induce less displacement compared to the liver set-up. These results would be expected because the head cradle induces movement in every direction which leads to lower efficiency in the transmission of the vibration into the tissue. On the other hand, possibly this set-up introduces more noise in the acceleration data than the liver set-up, which could have created some difficulties and errors in the double integration process. The custom-made pneumatic actuator proved to be less powerful and consistent, especially at higher frequencies (Fig. 3.36). However, this system was easy to install in the MR environment and it was cheap compared to the other two set-ups. Moreover, this device can be easily improved by replacing the actual subwoofer for a more powerful one and the new passive actuator, developed at the WBIC, (similar to the Mayo-Clinic one) should be used, in order to transmit vibrations into the tissue in a more efficient manner. By implementing these changes we can obtain more reliable results and induce higher displacement on the tissue of interest.

In summary, it was proved that different type of actuation devices can have a huge influence on the frequency response of the tissue and even the same actuator acting on different target tissues will give different results.

### **3.3.2 Shear Elasticity measurements**

After comparing the external measurements of motion during an MRE experiment in the gelatine phantom with a commercial accelerometer, shear elasticity measurements obtained with both: the piezoelectric system and the custom-made pneumatic set-up are discussed next in this section. In this study, we have performed phantom, liver and brain experiments to compare the results obtained with both systems. Therefore, this section is divided in three main sections each corresponding to a different target tissue.

All Experiments were run on a clinical scanner (Verio; Siemens, Erlangen, Germany). A single-shot Echo Planar Imaging (EPI) sequence with added MEG in the through-plane direction was used to acquire transverse phase contrast wave images. At each time point, two phase images with inverse MEG amplitude were acquired to calculate phase-difference images. Further acquisition parameters are specified in each of the following three sections.

#### **3.3.2.1 Phantom study**

Homogeneous phantom studies allow us to easily analyse and understand the propagation of the waves through the soft mimicking tissue. Therefore, phantom scanning with both set-ups was our first approach to compare shear elasticity results.

Further acquisition parameters were: repetition time:  $TR = 3.0$  s; echo-time:  $TE = 149$  ms; FOV = 300 mm, matrix size  $128 \times 128$ ; slice thickness = 10 mm.

Next, the parameters specific for MRE (frequency dependent) are described.

#### **Wave image acquisition – Piezoelectric liver set-up**

- **50Hz:**  $f_{MEG}$ : 5; vibrational amplitude (amplifier): 20; MEG Amplitude: 260 mTm<sup>-1</sup>;  $N_{MEG}$ : 2; and number of steps (Burst): 16;
- **100Hz:**  $f_{MEG}$ : 5; vibrational amplitude (amplifier): 10; MEG Amplitude: 120 mTm<sup>-1</sup>;  $N_{MEG}$ : 4; and number of steps (Burst): 16;
- **200Hz:**  $f_{MEG}$ : 30; vibrational amplitude (amplifier): 30; MEG Amplitude: 35 mTm<sup>-1</sup>;  $N_{MEG}$ : 8; and number of steps (Burst): 16;

***Wave image acquisition – Pneumatic actuator 1***

- **50Hz:**  $f_{\text{MEG}}$ : 5; subwoofer power: 5V; MEG Amplitude: 5 mTm<sup>-1</sup>;  $N_{\text{MEG}}$ : 2; and number of steps (Burst): 16;
- **100Hz:**  $f_{\text{MEG}}$ : 5; subwoofer power: 5V; MEG Amplitude: 10 mTm<sup>-1</sup>;  $N_{\text{MEG}}$ : 8; and number of steps (Burst): 16;
- **200Hz:**  $f_{\text{MEG}}$ : 30; subwoofer power: 5V; MEG Amplitude: 30 mTm<sup>-1</sup>;  $N_{\text{MEG}}$ : 8; and number of steps (Burst): 16.

***Wave generation***

The homogeneous gelatine phantom with concentration 1:3 (described in section 3.3.1.1) was used to simulate human soft tissue in the experiment and shear waves were introduced into the phantom by both set-ups: the piezoelectric system (liver set-up) and the pneumatic actuator 1 (both described in sections 3.1 and 3.2, respectively). In Fig. 3.37 the set-up used to test the piezoelectric actuator (liver set-up) is illustrated. The set-up used to test the custom-made pneumatic actuator was similar to the piezoelectric one but using the hardware presented in Fig. 3.15. Three different vibration frequencies of 50, 100 and 200 Hz were superposed with linearly increasing amplitude to minimize transient effects.

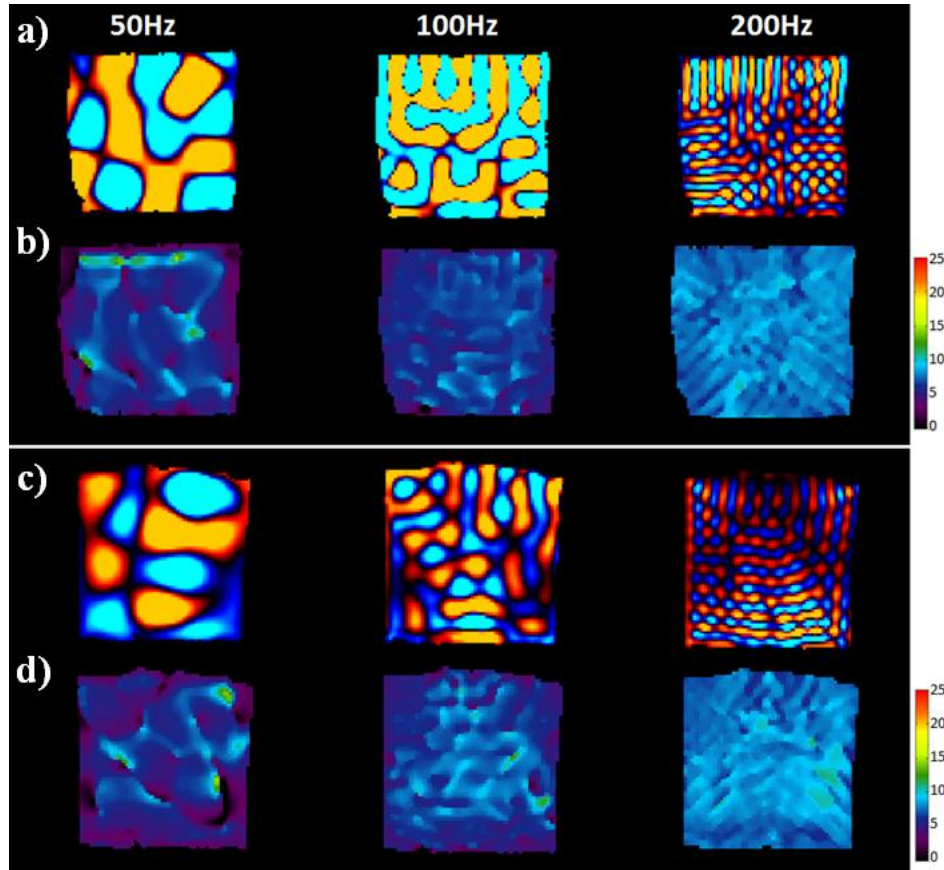


**Fig. 3.37** Images of the set-up used to test the piezoelectric and the pneumatic actuator. The piezoelectric actuator was either tested with the brain and with the liver set-up.

### ***Results and Discussion***

Fig. 3.38 shows experimental results obtained for sagittal slice orientations. The comparison of the displacement wave maps obtained with both set-ups revealed that the piezoelectric set-up induce a higher displacement leading to brighter images for this set-up (Fig. 3.38a) and c)). It is also clear that for both set-ups there is a huge drop-down in the displacement maps for 200Hz of excitation frequency. This result was expected because waves are more attenuated at higher frequencies and thus there will be a reduction in displacement maps.

Despite being obvious that the piezoelectric set-up induced a higher displacement in the tissue mimicking phantom, which corroborates the results obtained with the commercial accelerometer, presented in the last section, both set-ups presented similar elasticity values (at the same order of magnitude). These results demonstrate the feasibility and the validity of the MRE technique. Furthermore, observing the table of Fig. 3.38 it is clear that the piezoelectric set-up gave shear elasticity values slightly higher than the values obtained with the pneumatic system. The overestimated values obtained with the piezoelectric set-up compared to the pneumatic shear measurements, may be due to the more powerful and precise vibrations produced by the piezoelectric actuator, which implies that the shear wave will not be so attenuated compared to the shear waves created with the pneumatic set-up. Therefore, the values will be closer to the real shear elasticity measurements. Nonetheless, it must be pointed out that the feasibility and validity of the method using a custom-made pneumatic actuator was proved. Moreover, it is important to insist that these are preliminary results because the custom-made pneumatic subwoofer can be easily improved having the potential to present even more similar results compared with the results obtained with the piezoelectric system.



	50 Hz	100 Hz	200Hz
G Piezo (KPa)	6.514	6.842	7.021
G Pneumatic (KPa)	6.403	6.556	7.004

**Fig. 3.38** MRE data obtained for phantom with: a) and b) the piezoelectric system and c) and d) the custom-made pneumatic actuator. a) and c) are displacement wave images for 50, 100 and 200Hz and b) and d) are the corresponding shear stiffness maps. In the table below are presented the mean shear stiffness values for each one of the actuators for each frequency.

### 3.3.2.2 Liver study

Experiments on liver were also performed in one female healthy volunteer with 50kg and results were compared using both actuator set-ups. Images were acquired with breathholds (with air out) to obtain smoother and better images.

Further acquisition parameters were:  $TR = 8.6$  ms;  $TE = 4$  ms;  $FOV = 250$  mm; matrix size =  $350 \times 350$ ; slice thickness = 10 mm.

Next, the parameters specific for MRE (frequency dependent) are described.

***Wave image acquisition – Piezoelectric liver set-up***

- **50Hz:**  $f_{MEG}$ : 30; vibrational amplitude (amplifier): 40; MEG Amplitude: 300 mTm<sup>-1</sup>;  $N_{MEG}$ : 1; and number of steps (Burst): 16;
- **62.5Hz:**  $f_{MEG}$ : 30; vibrational amplitude (amplifier): 40; MEG Amplitude: 240 mTm<sup>-1</sup>;  $N_{MEG}$ : 1; and number of steps (Burst): 16;
- **75Hz:**  $f_{MEG}$ : 40; vibrational amplitude (amplifier): 40; MEG Amplitude: 200 mTm<sup>-1</sup>;  $N_{MEG}$ : 1; and number of steps (Burst): 16;

***Wave image acquisition – Pneumatic actuator 1***

- **50Hz:**  $f_{MEG}$ : 40; subwoofer power: 5V; MEG Amplitude: 300 mTm<sup>-1</sup>;  $N_{MEG}$ : 2; and number of steps (Burst): 16;
- **62.5Hz:**  $f_{MEG}$ : 40; subwoofer power: 5V; MEG Amplitude: 240 mTm<sup>-1</sup>;  $N_{MEG}$ : 8; and number of steps (Burst): 16;
- **75Hz:**  $f_{MEG}$ : 40; subwoofer power: 5V; MEG Amplitude: 200 mTm<sup>-1</sup>;  $N_{MEG}$ : 8; and number of steps (Burst): 16.

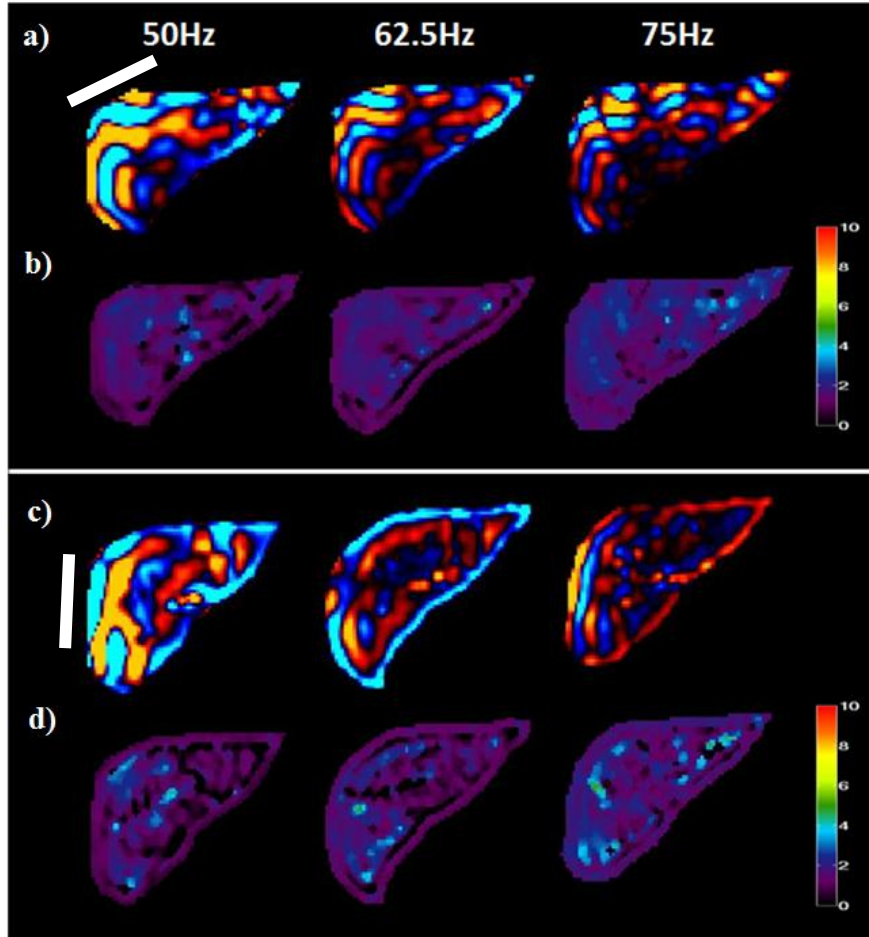
***Wave generation***

One female healthy volunteer underwent mechanical excitation in liver. Shear waves were introduced by both set-ups: the piezoelectric system (liver set-up) and the pneumatic actuator 1 (both described in sections 3.1 and 3.2, respectively). In Fig. 3.8 is illustrated the set-up used to test the piezoelectric actuator (liver set-up) and the set-up used to test the custom-made pneumatic actuator was similar to the piezoelectric one but using the hardware presented in Fig. 3.15. The plastic bottle (in the pneumatic set-up) was introduced laterally in the abdomen as illustrated in Fig. 3.39 by the white line. Three different vibration frequencies of 50, 62.5 and 75 Hz were superposed with linearly increasing amplitude to minimize transient effects.

***Results and Discussion***

Wave images (Fig. 3.39(a), (c)) appear more uniform using the piezoceramic device, which enabled a regular penetration throughout the liver. Reconstructed shear stiffness maps (Fig. 3 (b), (d)) appear smoother and more uniform using the piezoelectric system. Despite having noisier maps, the pneumatic system still presents global mean values in the same order of magnitude of the ones found with the piezoelectric setup. However, once more the shear

elasticity measurements obtained with the piezoelectric actuator were overestimated compared with the values obtained with the pneumatic actuator, probably for the same reason that was explained before.



	50 Hz	62.5 Hz	75Hz
G Piezo (KPa)	2.509	2.758	2.907
G Pneumatic (KPa)	2.256	2.383	2.887

**Fig. 3.39** MRE data obtained for liver with: a) and b) the piezoelectric system and c) and d) the custom-made pneumatic actuator. a) and c) are displacement wave images for 50, 62.5 and 75Hz and b) and d) are the corresponding shear stiffness maps. In the table below are presented the mean shear stiffness values for each one of the actuators for each frequency.

### 3.3.2.3 Brain study

Experiences were performed in brain on a female healthy volunteer for three different frequencies (25, 50 and 75Hz). However, due to some hardware limitations of the custom-made pneumatic actuator it was only possible to compare results for 25Hz of excitation frequency. To obtain better results at more vibration frequencies the pneumatic actuator has to be improved as suggested before.

Further acquisition parameters were:  $TR = 8.6$  ms;  $TE = 4$  ms; FOV = 250 mm; matrix size =  $350 \times 350$ ; slice thickness = 10 mm.

Next, the parameters specific for MRE (frequency dependent) are described.

***Wave image acquisition – Piezoelectric liver set-up***

- **25Hz:** frequency of the MEG: 25; vibrational amplitude (amplifier): 50; MEG Amplitude: 400 mTm<sup>-1</sup>; number of MEG cycles: 1; and number of steps (Burst): 40;

***Wave image acquisition – Pneumatic actuator 1***

- **25Hz:** frequency of the MEG: 5; subwoofer power: 5V; MEG Amplitude: 5 mTm<sup>-1</sup>; number of MEG cycles: 2; and number of steps (Burst): 40;

***Wave generation***

One female healthy volunteer underwent mechanical excitation in brain. Shear waves were introduced by both set-ups: the piezoelectric system (liver set-up) and the pneumatic actuator 1 (both described in sections 3.1 and 3.2, respectively). In Fig. 3.9 is illustrated the set-up used to test the piezoelectric actuator (brain set-up). The set-up used to test the custom-made pneumatic actuator was similar to the piezoelectric one but using the hardware presented in Fig. 3.15. The plastic bottle was placed touching the posterior part of the head of the subject.

***Results and Discussion***

Shear elasticity maps presented in Fig. 3.40 are noisy and are not really smooth and homogeneous. However, it is clear that the images obtained with the pneumatic set-up are much noisier than the images obtained with the piezoelectric set-up. Moreover, the wave image obtained with the pneumatic set-up is apparently obtained with a higher frequency of vibration, which is accordingly with the less control and precision that we obtain with the pneumatic set-up as referenced before. To improve the performance of both actuators a better system that enables the shear waves to penetrate more deeply into the skull is needed. The pneumatic actuator 1, despite giving reliable results for phantom and liver it needs further improvements (especially in the passive actuator) in order to be able to penetrate the skull barrier.



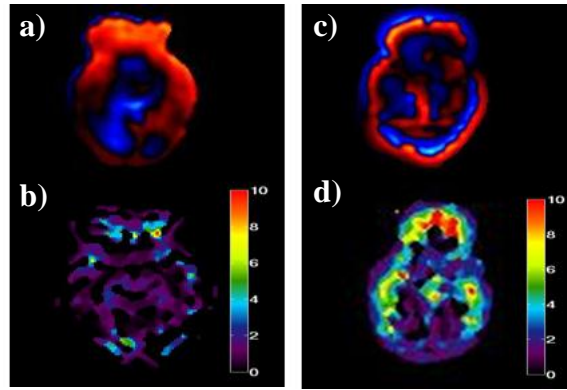


**Fig. 3.40** MRE data obtained for brain with: a) and b) the piezoelectric system and c) and d) the custom-made pneumatic actuator. a) and c) are displacement wave images for 25Hz and b) and d) are the corresponding shear stiffness maps.

### 3.4 CONCLUSION

In this chapter two types of actuation devices were described and compared: the piezoelectric and the pneumatic actuators. The piezoelectric device used in this study was developed by the Charité group and two different pneumatic systems: a custom-made pneumatic device and the commercial pneumatic system developed by Mayo Clinic were used.

The piezoelectric actuator was improved in terms of hardware and the custom-made pneumatic actuator was developed, with a reduced cost, from scratch and implemented in the MR environment at the WBIC. All of the hardware specifications and properties of the three actuation systems were carefully evaluated and systematically studied and compared.

In a first study, to compare both types of actuators, motion deflection tests were performed in a gelatine phantom using a commercial accelerometer. The data obtained directly from the accelerometer are acceleration measurements. Our interest is to measure the displacement that each device induces in the target tissue. Therefore, the acceleration data is introduced in a double integration process in order to obtain displacement values. The process of double integration presented some challenges due to the accelerometer drifting, gravity effect and, lack of initial conditions. The noise presented in the accelerometer measurements and the fact that it is a multifrequency signal, also introduced some errors in the double integration process. These problems were partially eliminated by the use of high pass filters in each stage of the process. There are three main types of filtering: IIR, FIR and a new method developed by Ribeiro et al. and improved by LisfKa which is called the FFT-DDI method. All of the three different types of filtering were tested in this project and the FFT-DDI method gave more reliable results. Using this method the acceleration measurements were converted into displacement values and the peak-to-peak magnitude of displacement was determined for five

different excitation frequencies of excitation. Both the liver and the brain set-up of the piezoelectric device, and both pneumatic devices were tested. The piezoelectric device proved to be able to induce a higher displacement on tissue, confirming the higher precision and control associated with this kind of device. The liver set-up proved to be more powerful and precise than all the other devices for lower frequencies (20Hz) and for higher frequencies (80Hz-100Hz). However, the Mayo set-up induced higher displacements in the material for frequencies of 30Hz-50Hz. However, the piezoelectric preformed always better when considering vibration frequencies higher than 80Hz. This suggests that higher frequencies could still be employed with this system with reduced attenuation in the tissue of interest. Concerning the displacement values obtained for the piezoelectric actuator head set-up, it proved to induce less displacement compared to the liver set-up. The custom-made pneumatic device induces little displacement when compared with the other devices. However, it is easily improved and it can still generate reliable results with the advantage of reduced cost.

Despite the disadvantages of the pneumatic system, it still generated waves in phantom and liver experiments and the stiffness values obtained were consistent comparing with the values obtained for the piezoelectric actuator. Shear elasticity measurements were also performed in brain, but due to hardware limitations it was just possible to obtain wave propagation at 25Hz of vibration frequency with the pneumatic actuator.

In summary, the pneumatic device offers an easier and faster system to integrate in the MR environment and the piezoelectric actuator can achieve higher frequencies and provide more reliable quantitative measurements. Nevertheless, other factors such as cost and complexity are a disadvantage with the piezoelectric system.

## **4. MRE Validation using DST and FEMs**

In section 2.2.4 a brief overview of different methods used in MRE to solve equation (2.14) was given. Moreover, we have seen that most of the approaches, make some assumptions in order to simplify the motion equation. The main assumptions considered in the inversion MRE algorithms are: the isotropicity; homogeneity and linear elasticity of the medium. Furthermore, it is also assumed that the propagating shear wave is plane, which is only true when a point vibration source is considered. Therefore, these assumptions become only an approximation from reality, which leads to elastic parameters such as: the shear modulus; wave velocity and; attenuation, to be somewhat different from the parameters extracted directly from equations (2.22) and (2.23) . Moreover, MRE studies are controversy amongst each other and a big variety of shear modulus for the same tissue is presented in the literature [53]. Some of the reasons for the difference between the results are: the dispersion of the shear wave speed at different excitation frequencies; a mismatch between wave propagation and image slice orientation; different boundary conditions; and also because different actuation systems, with different hardware properties, have a great impact in the frequency response of the tissue as discussed in section 3.3. Due to this incongruence in MRE literature, it is important to study all the parameters that affect the results, and to understand if the approximations and simplifications usually made can actually give us reliable results. Table 4.1 indicates the parameters that influence the MRE results in-vivo. In every step of the MRE process there are factors that influence the final results. As it is described in this table, in the first step of MRE the factors that contribute are mostly derived from the hardware and the mechanical excitation itself; in the image acquisition step the parameters that affect the process are: pixel resolution; imaging plane and; the type of sequence used, that can generate more or less noise in the images [82]. Finally, in the last step of MRE, the algorithm that performs the wave inversion and data processing parameters, such as filter limits, can affect the MRE final results. The effects of the factors and parameters pointed above on the viscoelastic properties measured should be examined and evaluated on a systematic way before MRE can become a useful and reliable diagnostic tool. [51] [9]

Magnetic Resonance Elastography: Design and Implementation as a Clinical Tool  
**Chapter 4 – MRE Validation using DST and FEMs**

**Table 4.1** Purely experimental parameters that affect MRE in-vivo results during the three different step of the MRE process discussed in section 2.2.

Experimental Parameters		
Mechanical Waves	MR Imaging	Wave Inversion
Frequency	Imaging Plane	Algorithm
Load Magnitude and Direction	Pixel Resolution	Filter Limits
Hardware Properties	Noise	

There are different methods for testing the reliability of the MRE technique. Both, static and dynamic shear testing (SST and DST, respectively) [35] [83] [84] and FEM [51] [22] [85] [86] [87] [88] have been used in previous studies. Nevertheless, the ability of the DST technique to study each of the effects stated above, especially the effect of different excitation frequencies, is limited, because it goes only up to 16 Hz, which is very low for a MRE exam [89].

FEM, on the other hand, provide detailed information about the wave propagation field and is a powerful technique that enables the study of the parameters stated above. Therefore, Finite Element (FE) models using ABAQUS 6.1 were developed in this project, in order to infer about the effects of the parameters in wave propagation through tissue (section 4.1).

In summary, the ultimate goal is to study all the parameters and systematically validate the MRE results obtained in-vivo and infer about their reliability. More specifically, this study can be divided in two main objectives:

1. Systematically study the influence of different parameters in the propagation of the waves using Abaqus (FEMs);
2. Validate MRE in-vivo results, comparing the shear elasticity values obtained experimentally with the shear elasticity values obtained by using DST.

This chapter of the dissertation will be divided in two main sections that will incorporate the two main objectives stated above: section 4.1, where an introduction about FEMs in general and about ABAQUS is given, and the models developed and respective results are

presented and discussed; section 4.2, where a brief description of the DST method is given as well as the methods and results obtained are presented.

#### 4.1 MRE VALIDATION USING FEMs

FEMs have been used throughout the years to validate and solve important and complex engineering problems. Moreover, advances in computer hardware have made FE analysis easier and very efficient into solving a huge range of engineering problems. However, when a FEM is developed it is important to make sure that the model and the assumptions made, are as close as possible to reality. Therefore, before using FE analysis to solve complex problems, the models should be validated and the dependency of the results on the purely computational parameters must be eliminated, in order to extract reliable conclusions from the FE analysis. In parallel, to be able to use FEMs with Abaqus and to use FEMs to validate the MRE process, we will first analyse what are the purely computational parameters and eliminate the dependency of the results on these parameters. In Table 4.2 the purely computational parameters and the parameters that are both computational and experimental are presented.

**Table 4.2** Purely computational parameters that affect FEM results and parameters that affect both: the computational and the experimental results.

Purely Computational Parameters	Computational and Experimental Parameters			
FEM analysis	Mechanical Waves	MR Imaging	Wave Inversion	Region of Interest
Boundary conditions	Frequency	Imaging Plane	Algorithm	Geometry
Mesh Density	Load Magnitude	Pixel Resolution	Filter Limits	Tissue Properties
Simulation Type	Load Direction	Noise		Surrounding Tissue Geometry and Properties

This section (MRE validation using FEMs) can be divided in two main objectives:

1. Eliminate the dependency of the FEM results on the purely computational parameters;
2. Validate MRE using FEMs by studying the influence of the experimental parameters on the results.

To accomplish the aforementioned objectives, this section was divided in two main studies:

**STUDY 1 - Examine the influence of the purely computational parameters:**

- study the influence of Boundary Conditions (BC) and model dimensions;
- study the influence of mesh density;

**STUDY 2 – Examine the influence of the experimental parameters:**

- study the influence of material properties
  - changing the density of the material
  - changing the elastic modulus (E) of the material

In section 4.1.1 it is given a brief description of Abaqus modules and its importance for the FEM process. To study the influence of all the parameters stated above different models were developed. Nonetheless, some of the models' properties remain constant from one model to another. Therefore, in section 4.1.2 general considerations about the models are given. All the parameters, methods and assumptions made are discussed in sections 4.1.3 and 4.1.4. In these sections STUDY 1 and STUDY 2 are respectively described.

**4.1.1 Understanding Abaqus and its Analysis Steps**

In order to have a better understanding of the FE models and different cases developed, next a brief overview about the different steps that should be considered in a MRE model using Abaqus is going to be given.

To obtain reliable results about the effect and influence of boundary conditions, excitation frequency, type of stimulus and material properties in the calculus of the shear modulus, it

is important to know which analysis method should be used in a first instance. In Abaqus an Analysis history is defined by:

- Dividing the problem history into steps;
- Specifying an analysis procedure for each step and;
- Prescribing loads, boundary conditions, base motions, and output requests for each step.

There are two different kinds of steps in Abaqus: general analysis steps, which can be used to analyse linear or nonlinear response, and linear perturbation steps, which can be used only to analyse linear problems. In Fig. 4.1 is represented a schematic diagram summarizing the modules for the FEM analysis in Abaqus.

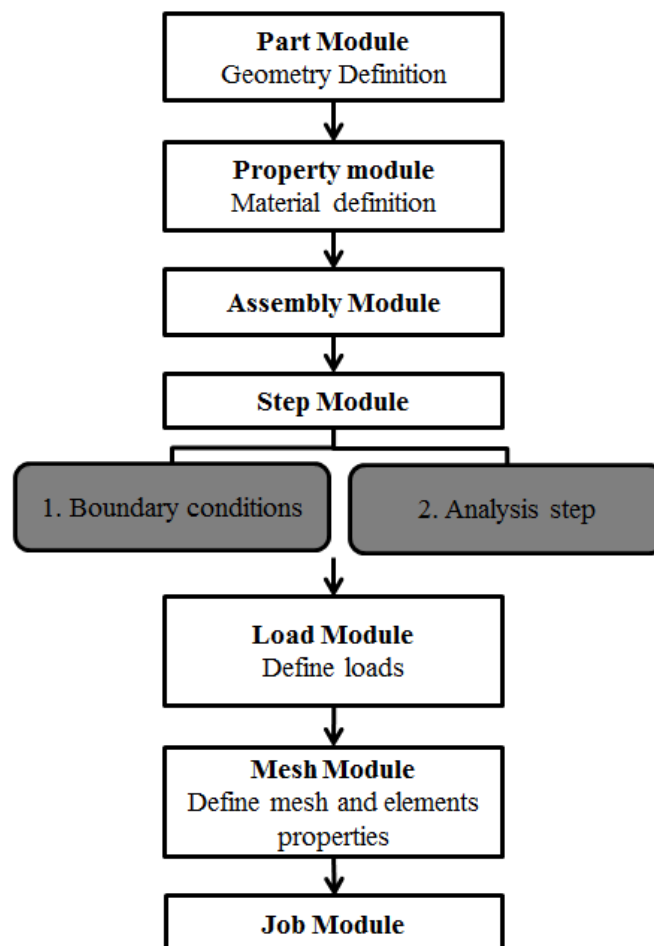


**Fig. 4.1** Schematic diagram of the different modulus in Abaqus.

#### *4.1.1.1 Part module*

The **part module** is where the geometry of the model is specified. In the current project the part was defined using the tools available in Abaqus. No other design program was needed due to the simple geometry of the models. The part module allows creating different types of parts like: deformable, discrete rigid, analytical rigid or Eulerian parts. In this project all the geometries created were solid and deformable (to mimic gel material) to let the waves propagate into the mimicking tissue models. The geometry of the models is very important, since it specifies the complexity of the mesh and the computational requirements to solve the FEM.

#### *4.1.1.2 Property module*

The second module of the FE modelling in Abaqus is the **property module**. This module allows the user to create sections, define material properties and assign them to regions of parts. When a section is assigned to a part, Abaqus automatically assigns that section to each instance of the part. As a result, the elements that are created when those part instances are meshed will have the properties specified in that section. So it is in this module that the material properties are specified. Like in the other modules, first, a linear elastic homogeneous solid was created to simplify.

#### *4.1.1.3 Assembly module*

The third step is the **Assembly module**. This module is used to create and modify the assembly. Each model should contain only one assembly, which is composed of instances of parts from the model. When a part is created, it exists in its own coordinate system, independent of other parts in the model. Therefore, the assembly model is used to unify the model and to position the instances relative to each other in a global coordinate system. As a result a model can contain many parts and part instances but it can only have one assembly. In this project as there is only one part, this part represents the assembly of the model. It is especially important when more than one part in the module exist.

#### *4.1.1.4 Step module*

The **step module** is used to create and configure analysis steps and associate output requests. The step sequence provides a convenient way to capture changes in a model, such as loading and boundary condition changes. In this module analysis steps can be created and output requests and type of analysis are specified. In addition, steps allow the user to change the analysis procedure of an existing step. The first step is always the



definition of BC and the other steps can vary depending on the type of analysis procedures and loading. In this project different BC have been specified to understand which type gives the best results.

### ***Transient Modal Dynamic Analysis***

#### **(1) Initial step**

Abaqus creates a special initial step at the beginning of the model's step sequence. This step allows the user to define boundary conditions, predefined fields, and interactions that are applicable at the beginning of the analysis.

In the model developed in this project, boundary conditions were applied to the model in this initial step. As the model developed has only one part, there were no interactions to set. Constriction of the bottom edge of the prism in the y direction was set to be the boundary conditions. The initial step was followed by two analysis steps presented as follows.

#### **(2) Frequency Extraction step**

The frequency extraction procedure performs eigenvalue extraction to determine the natural frequencies and the corresponding mode shapes of a system and it is a linear perturbation procedure. Abaqus provides three eigenvalue extraction methods, which are; Lanczos, Automatic multi-level substructuring (AMS) and subspace iteration.

The Lanczos solver has the most general capabilities and so was the one chosen for the FE model. This solver consists of a set of Lanczos "runs", in each of which a set of iterations called steps is performed. For each Lanczos run a spectral transformation that allows rapid convergence to the desired eigenvalues is applied. A Lanczos run will be terminated when its continuation is estimated to be inefficient. The idea of this approach is to start with a block of orthogonal vectors and to increase the dimension of subspaces by the block size at each Lanczos step. This approach allows automatic computation of all multiple eigenvalues if the largest multiplicity does not exceed the block size. A block size with dimensions (7, n) was used; where n is the number of eigenvalues requested. To capture the wave motion were extracted the first 30 natural frequencies and so the dimensions of the Lanczos block were (7,30).

### (3) Modal Dynamics Analysis step

After the natural frequency extraction step a transient modal dynamic analysis was performed to characterize the wave propagation in tissue.

A modal dynamic analysis gives the response of the model as a function of time based on a given time-dependent loading. The structure's response is based on a subset of the modes of the system, which must first be extracted using an eigenfrequency extraction procedure. The modes will include eigenmodes and, if activated in the eigenfrequency extraction step, residual modes. The number of modes extracted must be sufficient to model the dynamic response of the system adequately. The time increment set in this step was  $3.3 \times 10^{-4}$  s in order to sufficiently catch the wave motion during a cycle.

#### *4.1.1.5 Interaction module*

The next step is the **Interaction module**. In this module mechanical and thermal interactions between regions of a model or between a region of a model and its surroundings are specified. Interactions that may be defined include constraints such as rigid body constraints. In this project there were no interactions created because the model was homogeneous. However, creating an interaction step would be advisable if a stiffer inclusion in the model was considered.

#### *4.1.1.6 Load module*

After the interaction module comes the **Load module** that is used to define and manage; loads, boundary conditions, predefined fields and load cases. In MRE the load defines the excitation of the tissue so it should vary depending on the type of MRE exam that we are considering (quasi-static MRE, harmonic MRE or transient MRE) and also in the direction of excitation. In the present studies, the load was applied in the y direction (longitudinal loading) and it was always applied a sinusoidal excitation to mimic harmonic MRE exams described in section 1.2 of this report.

#### *4.1.1.7 Mesh module*

The **mesh module** allows the user to generate meshes on parts and assemblies created within Abaqus. There are different levels of automation and control available, which should differ depending in the type of analysis that is in use. There are three main points that should be considered on this module: seeds, that are related with the mesh density; mesh techniques, that provide different levels of control over the mesh; and element types

and shapes. Different shapes of elements can be generated. For two dimensional problems (the case of this project) the elements can be triangles or quadrilaterals. All the types of elements presented in Abaqus correspond to one of the aforementioned shapes. In this project it was only used one type of elements in the different models created. The type of elements used in this project was CAX8R that are usually used for stress analysis and correspond to quadrilateral elements. More precisely, these elements are 8-node biquadratic axisymmetric quadrilateral with reduced integration.

#### *4.1.1.8 Job and Sketch module*

The **job module** is used to create and manage analysis jobs and to view a basic plot of the analysis results. This module allows the user to create a job and submit it to analysis and to monitor its progress. It was selected a full analysis job to perform the analysis of the model and computational parallelization of 16 core was used to make the analysis faster.

The **sketch module** is used through all the modules listed above and is used to create a sketch that defines a planar part, a beam or a partition or to create a sketch that might be extruded, swept or revolved to form a three-dimensional part.

#### **4.1.2 FEM models – General Considerations**

To approximate the FE models to the 2D MRE image data and infer about the validity of MRE, for all FEM developed it was created an axisymmetric rectangular prism model with ABAQUS standard, representing a semi-axial cross section of the cylindrical gel phantom. The bottom edge of the prism was always constrained in the y-direction as it is represented on Fig. 4.2.

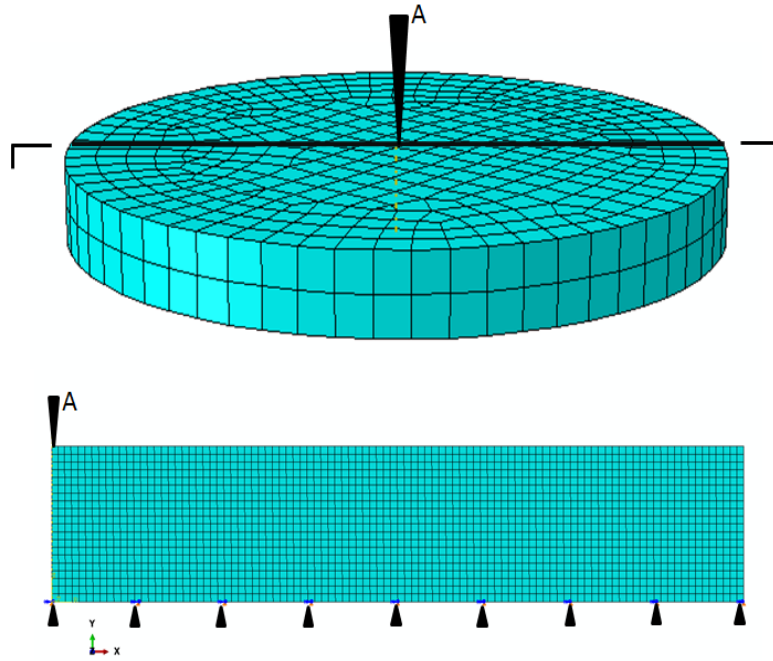


**Fig. 4.2** Geometry representation of the 2D FE model representing a semi-axial cross section of the cylindrical MRE phantom. The bottom surface of the model was constrained in the vertical direction and a sinusoidal load was applied in the middle of the top surface (A).

In the property module all the material properties were defined. Material properties were kept constant in STUDY 1 but were changed in STUDY 2 (details in the section of each study).

There was always just one assembly in all the models created, due to the homogeneity of the modes.

A transient Dynamic Analysis procedure was used to characterize the wave propagation in the model. Therefore, first it was performed a natural frequency extraction step using Lanczos solver, where the first 30 natural frequencies were extracted. This step was followed by a modal dynamic step. To catch the wave motion during the excitation, the time increment in modal dynamic analysis was set to  $3.3 \times 10^{-4}$  s.

#### **4.1.3 STUDY 1 - Examine the Influence of Purely Computational Parameters**

In the present study, the BC and the mesh properties were examined individually. To analyse these parameters, the rectangular prism was modelled as a homogeneous isotropic linear elastic solid with Poisson's ratio  $\nu=0.495$  (almost incompressible solid). 80 time frames were obtained in order to make sure that the steady-state was achieved (similar to

MRE experimental results) and no material damping was considered. The shear wavelength ( $\lambda'$ ) in the FEM was calculated at the time frame 80 (steady-state) and the frequency of excitation was set to 150Hz. Shear wavelength was determined by measuring the distances between wavepeaks directly from the output waveform data of the FEM.

The effects of the BC on shear wavelength can be examined by comparing two axisymmetric FE models; one with dimensions 100x20 mm and the other with dimensions 100x10 mm. The longitudinal dimension of 100 mm is kept constant because it is sufficiently large compared with the propagating shear wavelength. Therefore, it can be considered infinite. In Fig. 4.3 the shear wavelength ( $\lambda'$ ) as a function of Young's Modulus (E) (for the two models described above) is illustrated. From equation (2.8) it was possible to compare the results with the theoretical curve. Analysing the results is clear that the model with thickness 100x20 mm presents results that are closer to the theoretical curve. This result may be explained because the vertical dimension of the model with 10 mm of thickness is small, when the shear wavelength gets longer (it is clear from  $E=60\text{kPa}$ ). Therefore, the waveform is distorted from the ideal plane wave by the boundary conditions. From this analysis it is clear that BC are an important consideration when developing FE models and have to be taken into account in order to obtain reliable results with no distortion. In conclusion, the model with thickness 100x20 mm simulates better the wave propagation in the tissue. Consequently, this model is going to be used in the next studies instead of the model of thickness 100x10 mm.

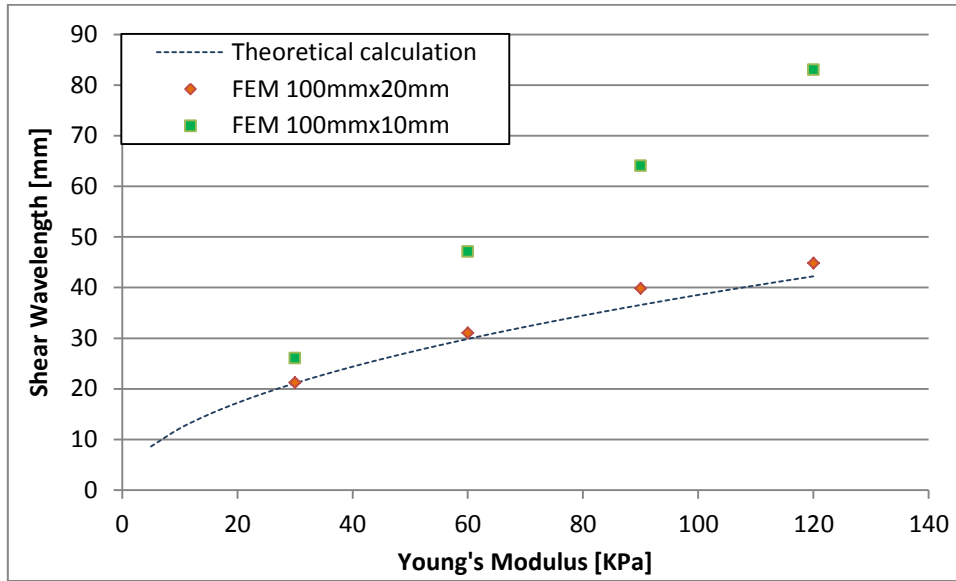


**Fig. 4.3** Shear wavelength ( $\lambda'$ ) as a function of the Young's Modulus (E) from two models with different thickness. The crosses correspond to the model of 10 mm thickness and the dots symbols correspond to the model of 20mm thickness. The dashed line corresponds to the theoretical relationship between E and  $\lambda'$  (equation(2.8)). A density of  $1 \times 10^3 \text{ kg/m}^3$  was considered.

To examine the influence of mesh properties, two models with different elements size were compared and the results are plotted in Fig. 4.4. First of all analysing displacement profiles of Fig. 4.4 it is clear that the axisymmetric FE simulation captures the amplitude drop-off and attenuation of the shear wave observed in experimental MRE (wave amplitude decreases in the x direction). This observed attenuation is due to material properties and energy dissipation that attenuate the waves through the model (tissue). Analysing this figure it can also be concluded that the model with 2x2 mm of element size, could not capture the wave propagating into the phantom because the mesh was too coarse. Therefore, as expected the model with a finer mesh (1x1 mm) gave better results, than the model with the coarser mesh, and could give us an appropriate displacement profile for all the 5 different Young's models. In contrary, the model with 2x2 mm could only predict the displacement profile for a Young's modulus of 120 KPa. However, it is important to mention that the model with the coarser mesh (2x2 mm) needs less computational time to solve the same problem. Therefore, the advantages and disadvantages have to be weighted carefully. In this specific case the computational time needed to solve both models was not very different and as the results were much better for the model with elements size of 1x1 mm, this model is chosen to be applied in later models and the model with elements 2x2 mm is discarded.

Magnetic Resonance Elastography: Design and Implementation as a Clinical Tool  
Chapter 4 – MRE Validation using DST and FEMs

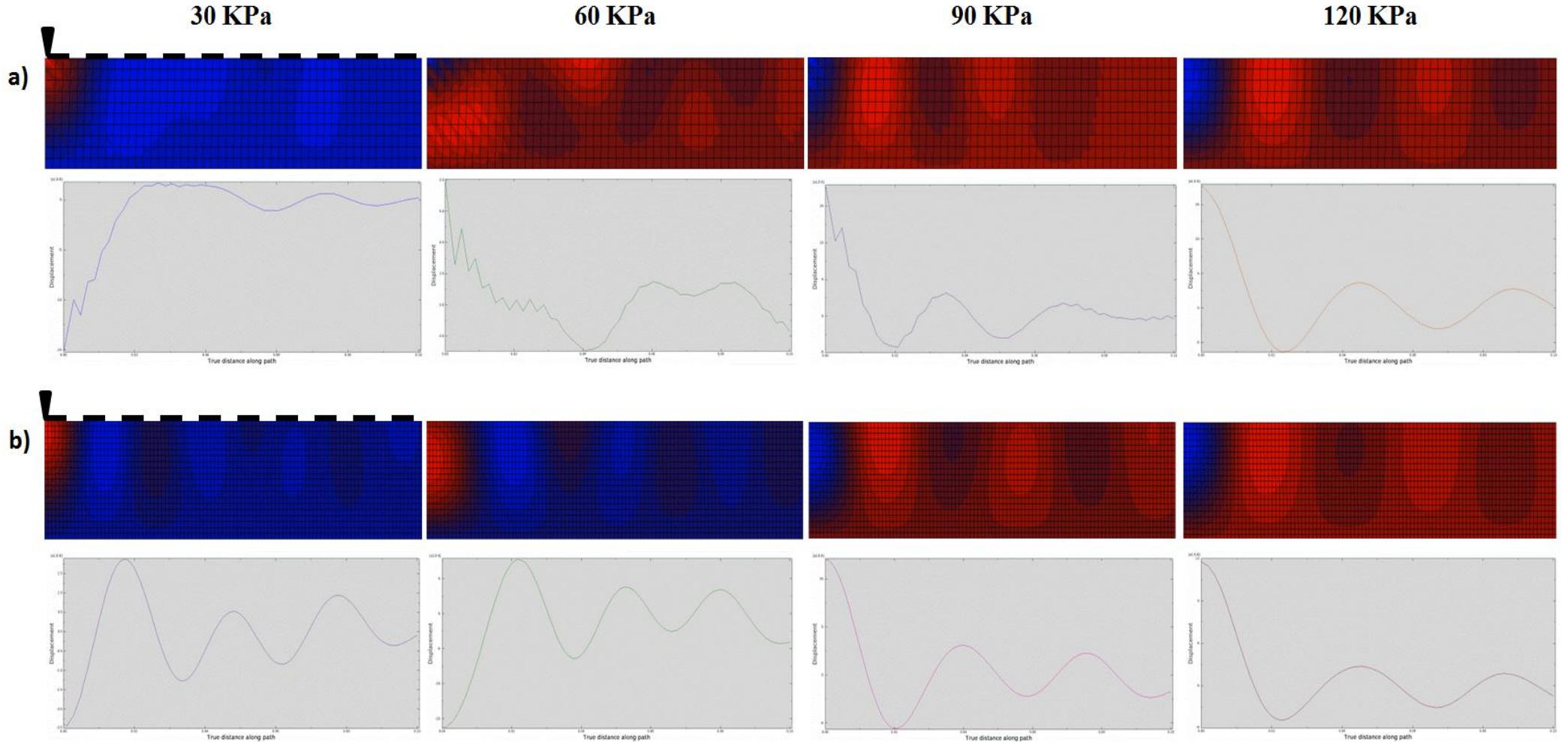


**Fig. 4.4** Effect of the elements size on the shear wave propagation throughout the FEM and correspondent displacement profile measured at the top edge represented in a dashed line in the figure. The black arrow at the top edge in the corner represents the sinusoidal load applied to the model. Two models were created, both axisymmetric rectangular prism models representing a semi-axial cross section of the cylindrical gel phantom. The bottom edge of the prism was always constrained in the y-direction both have the same dimensions (100x20 mm) and differ on the elements size: a) elements size of 2x2 mm; b) elements size of 1x1 mm. Each image represents the time frame 80 for different Young's values (30, 60, 90 and 120 KPa) for both models.

#### 4.1.4 STUDY 2 – Examine the influence of the experimental parameters:

In the present study the material density was examined. The simulated shear wavelengths with different Young's Modulus (E) and material densities at excitation frequency of 150Hz are shown in Fig. 4.5.

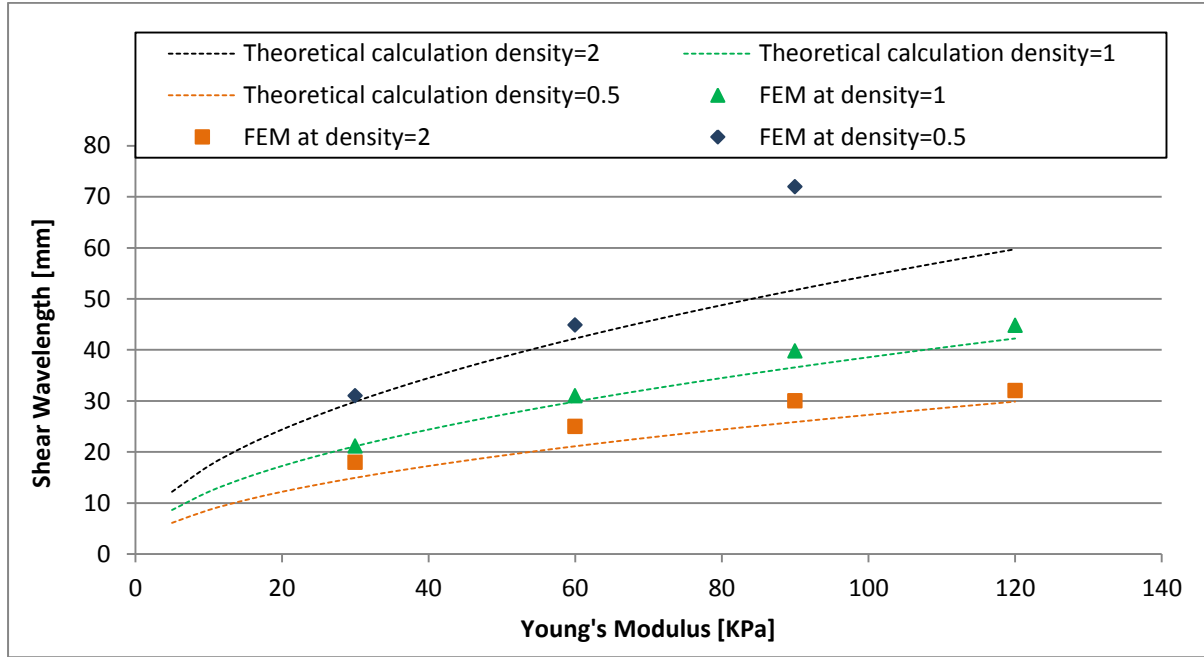


**Fig. 4.5** Shear wavelength ( $\lambda'$ ) as function of Young's Modulus (E) with 150Hz of excitation frequency and at different densities of material. The dashed curves represent the three theoretical relationships between E and  $\lambda'$  for three different densities ( $0.5 \times 10^3 \text{ kg/m}^3$ ;  $1 \times 10^3 \text{ kg/m}^3$  and  $2 \times 10^3 \text{ kg/m}^3$ ).

From Fig. 4.5 it can be concluded that the present axisymmetric FE model presents similar results than the theoretical calculations and the in-vivo MRE experiments, which suggest that both MRE and FE modelling are appropriate and reliable techniques to investigate the propagation of waves in the tissue and determine elastic properties of the tissue. However, the FEM at density of  $1 \times 10^3 \text{ kg/mm}^3$  presented more similar results to the theoretical curve than the other two models of different densities. From the same figure it is also clear that the propagation of the wave through the tissue and the corresponding shear wavelength vary a lot depending on the density of the tissue itself. Therefore, when developing FE models it is very important to introduce the right value for the tissue density that we want to model.



## 4.2 MRE VALIDATION USING DST

DST has been frequently used to characterize soft biomaterials [90]. In this test, thin samples of the material are subjected to oscillatory shear strains. Different groups have used a commercial rheometer [91] [92] [93] or a custom-build system [94]. Shear force or shear torque is measured and these values are then converted to shear stress, usually over a range of frequencies. Finally the data is analysed to obtain the complex shear modulus. Some groups have compared the results obtained with DST with the results of MRE and proved that DST is a shear test that provides quantitative information for MRE studies [35] [83] [84].

More generally, DST is a non-destructive dynamic material test that can measure the shear modulus over a frequency range. In this type of testing a sinusoidal stress ( $\sigma$ ) is applied to a known sample of known geometry and the resulting strain ( $\gamma$ ) is measured as well as the phase lag ( $\delta$ ). From these data it is possible to determine the complex modulus ( $G^*$ ), composed of the storage modulus ( $G'$ ) and the loss modulus ( $G''$ ) by equation (4.1).

$$G^* = G' + iG'' = \frac{\sigma}{\gamma} \cos \delta + i \frac{\sigma}{\gamma} \sin \delta \quad (4.1)$$

where the storage modulus is equivalent to the elastic shear modulus, while the loss modulus contains the viscoelastic component of the shear modulus [95].

More specifically the sample can be subjected by a controlled stress or a controlled strain and for a known stress the sample will deform a certain amount. Thus, the deformation that it suffers is related to its stiffness.

To perform this analysis it has to be assumed that the shear displacement is linear and also that the shear strain is constant through the thickness of the sample. Therefore, when soft materials are tested, typically very thin samples are used to avoid inertial effects at higher frequencies. However, as the thickness of the sample decreases it becomes more difficult to cut samples of uniform thickness and to maintain structural integrity of the sample. Thus, in fact, shear modulus estimation of soft materials using DST without inertial correction are limited to low frequencies [94] [96]. Due to these limitations, DST on agarose gels, is challenging and all of the factors that influence the test results have to be kept in mind and analysed carefully.

The purpose of this study was to compare the shear modulus measured with DST to MRE stiffness estimates in three different concentrations of gelatine phantoms. The DST tests were performed at the department of Chemical Engineering and Biotechnology of the

University of Cambridge, with the help and supervision of the Senior Technical officer Dr. Simon Butler.

#### 4.2.1 DST Instrumentation

Rheometry is the measurement of the flow and viscoelastic parameters of complex fluids. The scientific instruments in which rheometric measurements are performed are called rheometers. They incorporate the necessary simple flow geometries, in which the fluid being measured is subjected to forces or movement, and from which the resulting movement or force is measured. Complex flows of any kind can be split up into components of shear and extensional flows, and Rheometry is the search for the simple geometries where either shear or extensional flows dominate [97]. Therefore, there are two distinctively different types of rheometers: rheometers that control the applied shear stress or shear strain are called rotational or **shear rheometers**; whereas rheometers that apply extensional stress or extensional strain are **extensional rheometers** (Fig. 4.6). In this study we used the shear type rheometers.

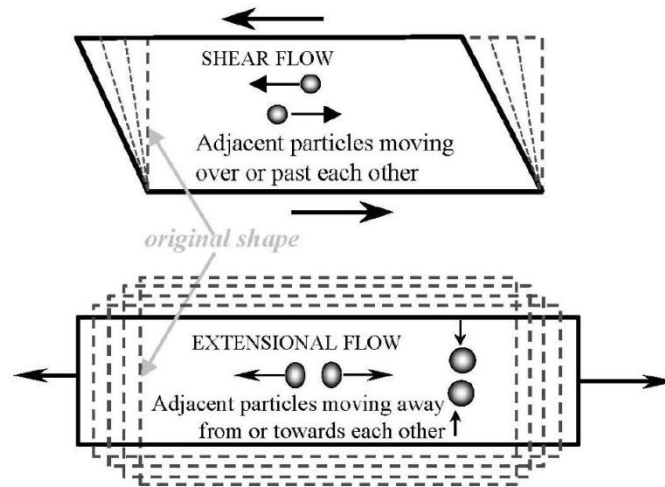


**Fig. 4.6** Particle motion in shear and extensional flows. [97]

Rotational or shear type rheometers are usually designed as either a native strain-controlled instrument (control and apply a user-defined shear strain which can then measure the resulting shear stress) or a native stress-controlled instrument (control and apply a user-defined shear stress and measure the resulting shear strain).

In general, the instrumentation of a rheometer consists of; a displacement sensor, a temperature control system a drive motor and a drive shaft. The displacement sensor measures a change in voltage as a result of the instrument probe moving through a magnetic

core; the temperature control system is used to maintain the temperature constant (it can be changed by the user); the force motor is used to generate the sinusoidal wave that is transmitted to the sample via the shaft drive. Finally, the shaft drive is used to maintain the motor force over some limits, enabling the sample clamps to hold the sample with the correct amount of strength. In this project we have used two different types of rheometer: a strain and a stress rheometer and compared the results.

#### *4.2.1.1 Strain Rheometer*

In this project we have used an ARES device (Fig. 4.7). It was manufactured by Rheometric Scientific Ltd. (now taken over by TA Instruments) and its serial number is 500014312. It is controlled using TA Orchestrator software (version 6.6.3) and uses a 2K FRTN1 transducer (FRT = force re-balance transducer). The geometry used for the tests were 50mm parallel plates, with the temperature controlled using a water jacket fitted to the bottom plate.

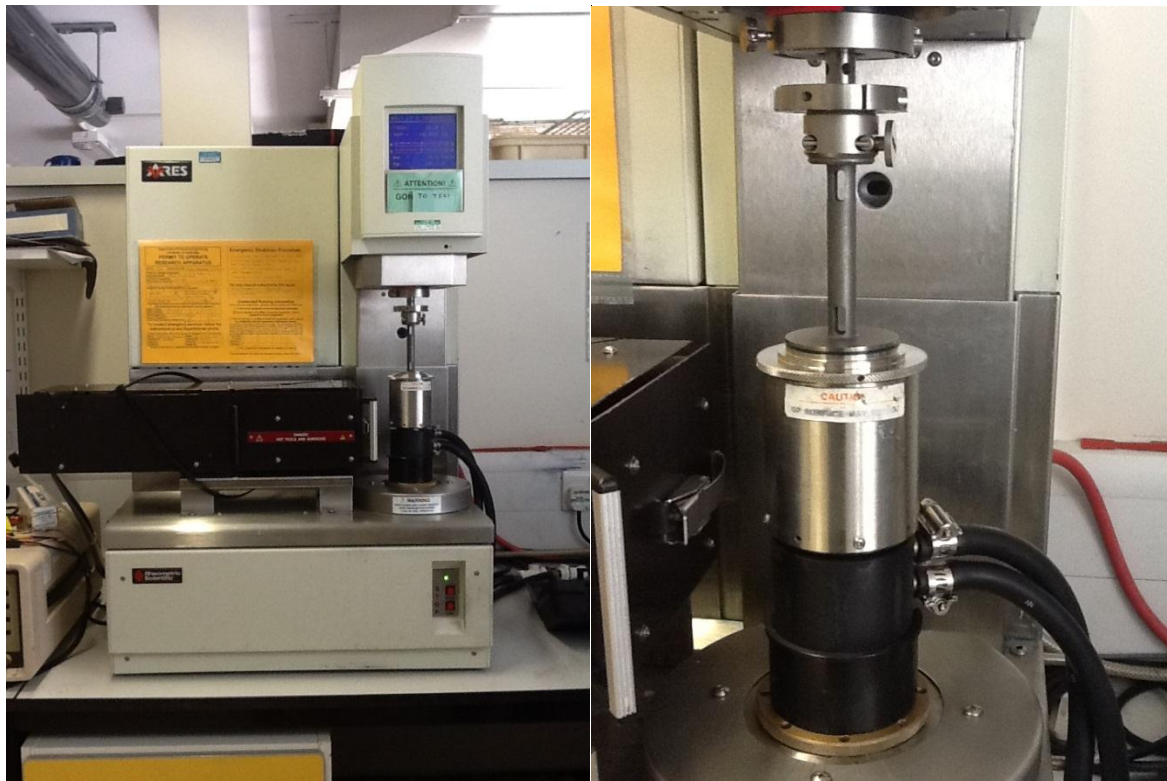


**Fig. 4.7** Photographs of the strain rheometer used in this study.

#### *4.2.1.2 Stress Rheometer*

The Bohlin CVO120 (Fig. 4.8) is a controlled stress rheometer manufactured by Malvern Instruments Ltd. Its serial number is 01007870CURA144. It is controlled using the Bohlin software (version 6.50.5.7). We used both 40 and 20mm parallel plate geometries for the

tests. The temperature was controlled by a Bohlin ETO (Extended Temperature Option). This consists of an electrically heated bottom plate that uses cold air for cooling.



**Fig. 4.8** Photographs of the stress rheometer used in this study.

#### **4.2.2 Samples**

Samples of phantoms (described in section 3.3.1.1) with three different concentrations of dental gel (1:1 – same concentration of water and gel; 1:2 – one measure of gel for two measures of water and 1:3 – one measure of gel for three measures of water) were used.

To do the samples with the same diameter and thickness we printed, in the HP 3D printer, various circular containers with 1mm of thickness and three different diameters (50 mm, 40 mm and 20 mm) (Fig. 4.9).

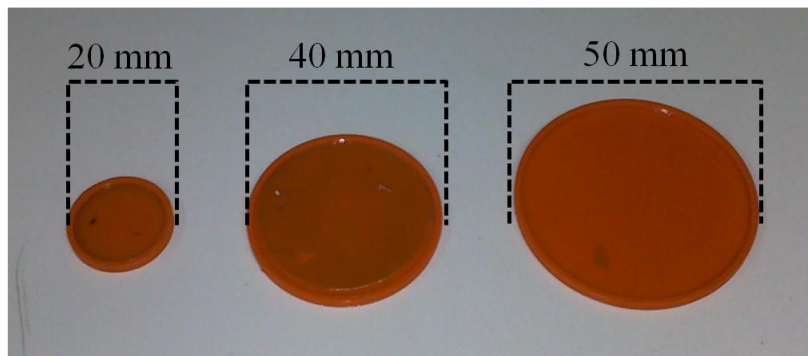


**Fig. 4.9** Image of the circular containers where the samples were poured to dry.

The warm gelatine mixture was poured in the custom-made containers and dried for approximately 10 min. The gel texture and stiffness enabled an easy removal of the gel from the containers.

### **4.2.3 Test Modes**

There are three main types of testing modes that are performed in order to probe viscoelastic properties of a determined material; temperature sweep, frequency sweep and amplitude sweep and strain sweep.

In order to investigate the effect of shear strain and shear stress on the gel samples, we performed the frequency, amplitude and strain sweep tests. Using the shear strain rheometer we performed frequency sweep and strain sweep and using the shear stress rheometer we performed frequency and amplitude sweep. The temperature was kept constant to 19°C (MR room temperature) in all tests to better mimic MRE conditions in vivo thus the temperature sweep test was not performed. To have a better understanding of these three test methods (frequency, strain and amplitude sweep) they are described next as well as the methods used in this study.

#### **4.2.3.1 Frequency sweep**

During a frequency sweep test, a sample is held to a fixed temperature and amplitude of deformation, and the frequency of excitation is varied. In this case, to analyse the data, the storage modulus and the loss modulus are plotted against the frequency. At low frequencies the data describe the behaviour of the samples at slow changes of stress and at high frequencies it is expressed the behaviour of fast load.

In this study, we performed the frequency sweep test for 30 different frequencies from 0.1Hz to 100Hz for the 3 different groups of samples (3 different concentrations). We used the strain and the stress rheometer to perform this test. However, the results obtained with the stress rheometer are not so reliable and precise for the frequency sweep, due to the technical principals of the machine and thus, were discarded.

#### **4.2.3.2 Strain and stress sweep**

During a strain or stress sweep test the amplitude of deformation of strain or stress (respectively) is varied while the frequency and the temperature are kept constant. To analyse the amplitude sweep tests the storage modulus ( $G'$ ) and the loss modulus ( $G''$ ) are plotted against the deformation.

The strain sweep test was performed with the shear strain rheometer for 31 different strain amplitudes, from 0.00918% to 10.1217% of the total amplitude.

The stress sweep test was performed with the shear stress rheometer for 30 different stress amplitudes, from 0.1 to 242.

#### 4.2.4 Results and Discussion

Oscillatory Rheometry tests have been performed, and the results obtained were compared to the MRE in-vivo results.

Applying amplitude sweep tests to the three different concentration phantoms, the linear regime of viscoelasticity was estimated to be 0.5%. Thus, the frequency sweep tests were performed at a strain value of 0.5% to make sure that we were dealing with the linear region of viscoelasticity (Fig. 4.10).

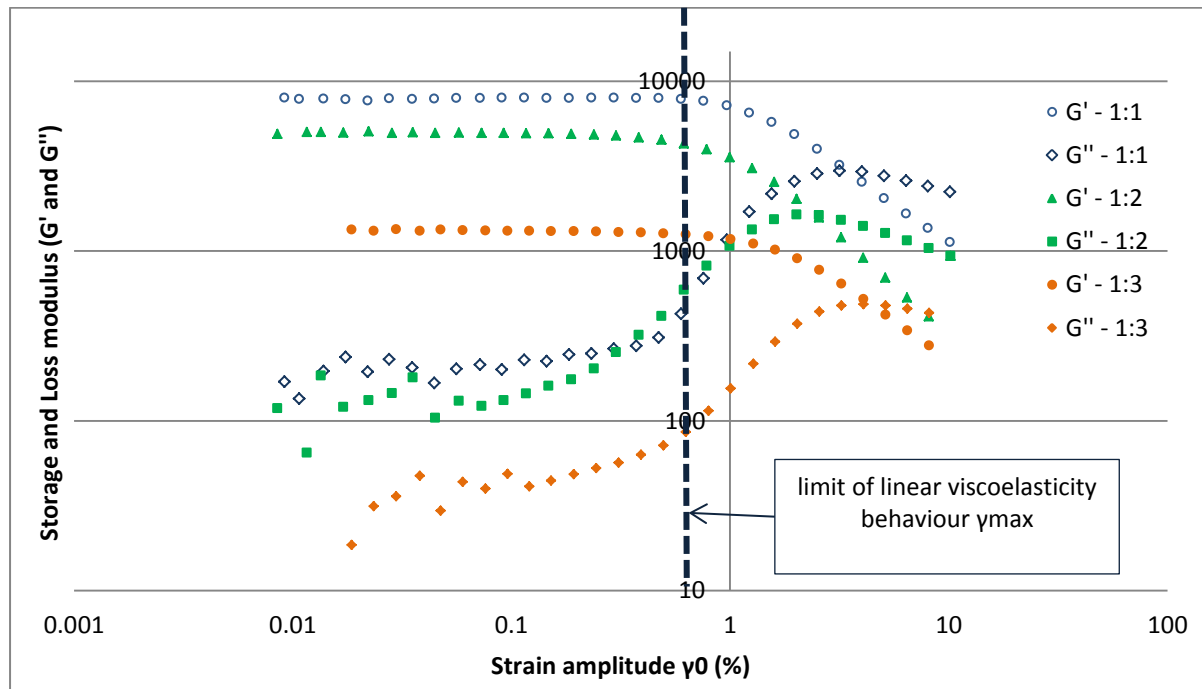


**Fig. 4.10** Amplitude strain sweep of 3 gelatine phantoms with concentrations of 1:1; 1:2 and 1:3 (gel:water). The dashed line marks the limit of the linear viscoelastic limit.

A frequency sweep test was also performed in order to compare the results obtained with the DST and with MRE in-vivo. However, frequency range limitations of both methods did not allow a direct comparison in the expected frequency range. Other groups have covered larger frequency ranges and were able to combine directly the data from rheometric studies and MRE obtaining a strong correlation of the results reported with the two techniques. Based on these above mentioned groups, we can say that MRE data are found to be a good extrapolation of rheometric data. However, this extrapolation should be further confirmed with rheometric tests which can reach higher frequencies reliably.

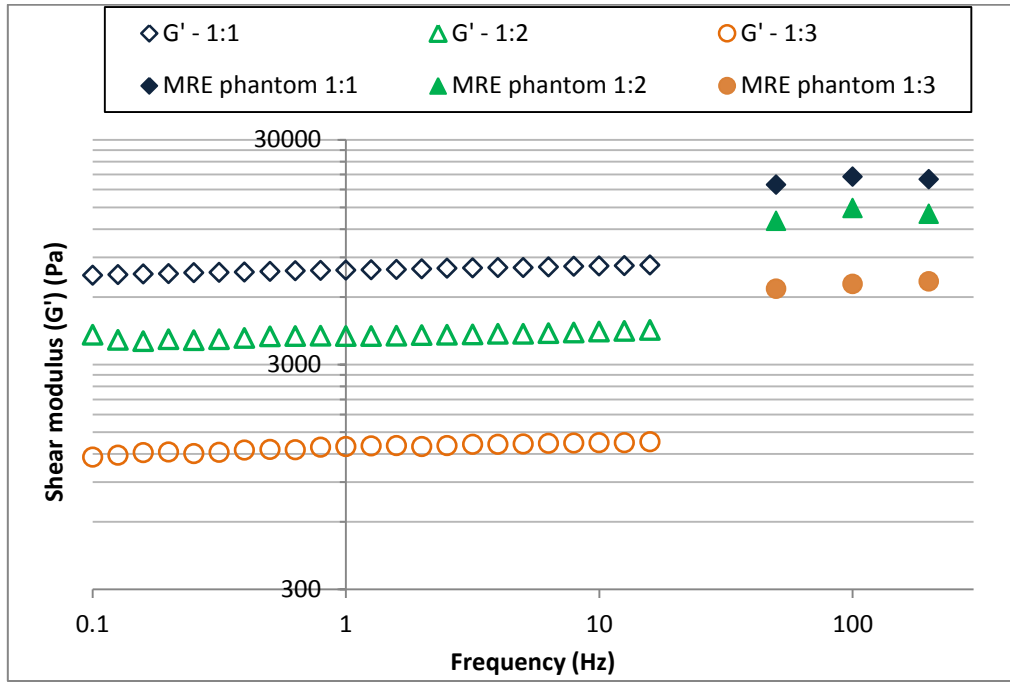


**Fig. 4.11** Storage modulus of the shear moduli versus frequency, for rotational rheometric data. Frequency sweep test of the three gelatine phantoms (concentrations of 1:1; 1:2; 2:3 (gel:water)).

As referenced before, the samples have been tested in frequency sweep maintaining the temperature constant at 19°C (same temperature at the MR room). The storage and the loss modulus have been determined for different frequencies and the results were compared to the results obtained with MRE results (Fig. 4.11).

As it can be seen in Fig. 4.11, values of shear moduli found by both methods are in the same order of magnitude. However, the MRE measurements gave higher values for all the 3 different phantoms these results were also reported in other studies [91].

Another aspect that should be mentioned and discussed is concerning the elastic behaviour of the gelatine phantoms. Although most of the MRE inversion methods assume that soft tissues follow the Hooke's law, it is well known that they actually deviate from it, and present viscoelastic behaviour. Therefore, to better mimic soft tissues MRE phantoms are usually gel phantoms with viscoelastic behaviour. Nevertheless, it has been notice that the gelatine phantoms created at the WBIC do not exhibit nor linear elastic (the relation between stress and strain is not linear) nor viscoelastic behaviour. This assumption is made because all of the phantoms made lost their elastic properties after being used some times due to the exerted load of the actuator. Moreover, they tend to lose water becoming stiffer and less viscoelastic. Though, they presented permanent deformation. This property of the phantoms is not favourable to study MRE because presumably the values of the shear parameters will change

over the time. Having this in mind, new phantoms should be made from time to time in order to be sure about their elastic properties.

### **4.3 CONCLUSION**

In this chapter we have seen that there is a huge variety of parameters that affect MRE results. These can be related to specific hardware properties of the actuation device, as shown in section 3.3, or - more significantly - related to the experimental parameters and to the assumptions that are made in most of the inversion algorithms in order to solve the motion equation. Therefore, the validation of the MRE technique is a very important step before it can become a useful and reliable diagnostic technique. **FE models** using ABAQUS were developed in order to study all the parameters stated. Two different types of parameters were considered: purely computational ones and experimental ones. The use of FE modelling requires that the results will depend only on the experimental parameters and not on the purely computational ones. In order to evaluate this dependency, two different studies using FEMs were performed. In both studies, an axisymmetric rectangular prism model representing a semi-axial cross section of the cylindrical gel phantom was created so that the bottom edge of the prism was always constrained in the y-direction. A transient Dynamic Analysis procedure was used to characterize the wave propagation in the model. Therefore, a natural frequency extraction step was performed followed by a modal dynamic step.

The main objective of **STUDY 1** was to study the influence of purely computational parameters and to try to eliminate their influence on the FE models. In this study the parameters that were changed were: BC and model dimensions, and mesh density. In order to study BC, two different models with different dimensions (100x10 mm and 100x20 mm) were created. Graphics of the shear wavelength were obtained for the two different models and were compared to the theoretical curve of the shear wavelength as a function of Young modulus. The model with thickness 100x20 mm yielded results that are clearly closer to the theoretical curve. From this analysis we concluded that BC is an important consideration when developing FE models and has to be taken into account in order to obtain reliable results with no distortion. In conclusion, the model with thickness 100x20 mm provides a better simulation of the wave propagation in the tissue and was used for all the remaining cases. Mesh density was also studied with two models with different elements of size 1x1mm and 2x2 mm. Images of the wave propagation into the axisymmetric models and displacement profiles have shown that the model with element size of 2x2 mm is unable to



capture the wave motion and insignificant displacement values were obtained for this model. With this experiment we can conclude that mesh properties is an FEM parameter that must be carefully chosen in order to eliminate the dependency of the results. For all the other models developed, an element size of 1x1 mm has been applied.

The main objective of **STUDY 2** was to study the influence of the experimental parameters as material properties and load specifications. In order to do that, different material densities and Young moduli were assigned to the material and different types and magnitude of loading were also applied. In this study the conclusions of STUDY1 were applied, in that a model with dimensions 100x20 mm and size elements of 1x1 mm was created to eliminate the influence of the purely computational parameters. The density of the material was changed and shear wavelength was plotted against Young modulus for three different material densities. This study clearly showed that the propagation of the wave through the tissue and the corresponding wavelength vary significantly depending on the density of the tissue itself. The material with density of 1 kg/mm<sup>3</sup> revealed to be closer to the theoretical curve than the materials with the other two densities.

In the second part of this chapter, the necessity of validating MRE results was emphasized and it was concluded that, amongst the techniques that have already been used to validate MRE results, the **DST technique** is a useful modality despite its limitations in terms of vibration frequency. DST was described and the experimental MRE results were compared with the results obtained with the DST technique. Results obtained with DST and experimental MRE were plotted in a graphic with the loss ( $G''$ ) modulus as a function of frequency of vibration. Although the DST technique provided results only up to 16Hz, it was concluded that we could correctly extrapolate these results to higher frequencies and compare them with results obtained with experimental MRE. The results obtained with both techniques showed good agreement.



## **5. Conclusion and Final Remarks**

### **5.1 CONCLUSION**

MRE shows great potential for the non-invasive in vivo determination of mechanical properties in a variety of tissues, leading to a powerful technique with the potential to diagnose at an early stage diseases that change tissue elasticity.

In order to generate mechanical waves, an actuation device is needed and there are important considerations that must be followed to enable appropriate wave propagation through the tissue of interest. Furthermore, the actuator should allow the variation of the frequency, amplitude and type of excitation depending on the tissue that it is going to be imaged. Pneumatic, piezoelectric and electromagnetic devices have been developed and implemented at the MR environment. The advantages and disadvantages of each actuation device have been studied and described thoroughly. The piezoelectric device implemented at the WBIC has been compared with a custom-made pneumatic device developed from scratch during this project. In order to compare both actuation devices, motion deflection tests were carried out in a gelatine phantom with a commercial accelerometer, and shear elasticity maps of the gelatine phantom, liver and brain were obtained. It was proved that the piezoelectric actuator is more powerful and enables a higher control than the pneumatic actuator. In spite of the disadvantages of the custom-made pneumatic system presented herein, it was nonetheless able to generate waves in phantom and liver experiments and the stiffness values obtained were consistent when compared to the values obtained for the piezoelectric actuator. Shear elasticity measurements were also performed in brain, but due to hardware limitations it was only possible to obtain wave propagation at 25Hz of vibration frequency with the pneumatic actuator. The pneumatic actuator proved to be more flexible and easier to implement in the MR environment, as expected. Moreover, although the commercial pneumatic actuator developed by Mayo-Clinic has similar cost comparing with the piezoelectric actuator, this study proved that a custom-made MRE pneumatic device can be implemented from scratch in the MR environment with reduced costs.

MRE studies are contradictory amongst each other and a big variety of shear moduli for the same tissue is presented in the literature. This incongruence is due to the huge amount of different parameters that influence the MRE results. In order to validate and test the

reliability of the MRE results, both FEM and DST have been employed in this project. Nevertheless, the ability of the DST technique to study each of the effects that affect MRE results is limited because it goes only up to 16 Hz, which is very low for a MRE exam. FE modelling, on the other hand, provides detailed information about the wave propagation field and is a powerful technique that enables the study of the parameters stated above. Therefore, FE models using ABAQUS 6.1 were developed in this project, in order to infer about the effects of the parameters in wave propagation through the tissue of interest.

In spite of the frequency limitations that characterize the DST technique, it was concluded that DST results can be correctly extrapolated to higher frequencies. The results obtained with DST and experimental MRE showed good agreement, confirming the validity of MRE for measuring tissue elasticity parameters.

In summary, in order to optimize a piezoelectric actuator to be acceptable as a clinical aid, the safety of the equipment was assessed and approved by MHRA, its performance was evaluated and changes were made to reduce the losses in energy transfer from the active to the passive driver. Moreover, improvements in the hardware were also made to make it more user-friendly and comfortable to the patient. Finally, and probably the most important and hard to obtain is the consistency and meaning of the results that were accessed and evaluated using FEMs and DST. This project was crucial in the development of the MRE technique at the WBIC and one step further was taken towards the acceptance of the ethics committee in order to implement this new promising diagnostic technique in clinical practice.

## **5.2 CHALLENGES**

MRE is a new imaging technique that has been developed and employed in clinical practice for the last decade. Although far from perfection, it yields quantitative measures of elasticity that clearly demarcate differences between tissue types and identify tumours as areas of high stiffness. However, throughout the execution and implementation of the current project it was clear that this technique still presents a lot of challenges that must be overcome. Challenges remain in pulse sequence design, the ability to deliver sufficient signal to all areas of the body, and the improvement of processing algorithms in order to generate more accurate, higher resolution elasticity and attenuation maps. It should also be mentioned that in this particular project, special attention was given to MRE hardware

and its limitations, and it was proven that the type of actuation device is a major issue with the potential to strongly condition MRE results. To overcome these challenges, further research on this field has to be conducted in order to eliminate the major hurdles that currently still prevent MRE from becoming a reliable diagnostic technique

### **5.3 FUTURE PLANS**

In this project, the advantages and disadvantages of different actuation devices have been explored and a piezoelectric and a custom-made pneumatic actuator have been implemented in the MR environment. The MRE technique was implemented from scratch at the WBIC which led to a lot of developments both in hardware and software and one step further was taken towards reaching the ethics approval that is mandatory to use the technique in clinical practice. However, as expected there are still a lot of improvements that must be made before this happens. Future work that would be required may be divided in four main steps:

- (1) Improvement of the piezoelectric hardware in order to make it more user-friendly
  - a. Replacement of the liver wood paddle to improve wave propagation into the liver;
  - b. Adaptation of the lever on the piezoelectric device for brain set-up enabling a higher degree of precision and power: a higher lever will increase the vibration in the brain and the waves will be less attenuated in the skull;
  - c. Replacement of the high voltage amplifier by a low voltage amplifier due to ethical issues.
- (2) Improvement of the pneumatic set-up
  - a. Replacement of the subwoofer with a more powerful one;
  - b. Implementation and testing of the new passive actuator described in section 3.2.2.1.
- (3) Implementation of a different rheometric technique with no frequency limitations to test the phantoms, and possibly real soft tissue (such as brain or liver samples), to compare the results with the results obtained with MRE.
- (4) Validation and comparison of the MRE results with FEMs

Concerning topic 4 (above mentioned), in this project, FE modelling has been used to study different parameters that affect the MRE process and consequently the results

obtained. To do that, FE models that mimic an MRE scan image were created and the parameters were changed systematically and the propagation of the waves in the tissue was analysed. However, one important step of the MRE process is the introduction of the images in the inversion algorithm enabling the computation of the shear modulus. Therefore, one interesting development would be to introduce the models created by the FE modelling (fake MRE images with specific parameters known a priori) in the inversion algorithm and to compare the shear modulus obtained for these images with the experimental MRE images. This process would enable a more accurate validation of the inversion algorithms and it would enable inference about the actual accuracy and precision of this new diagnostic technique. Fig. 5.1 shows a schematic diagram of this process.

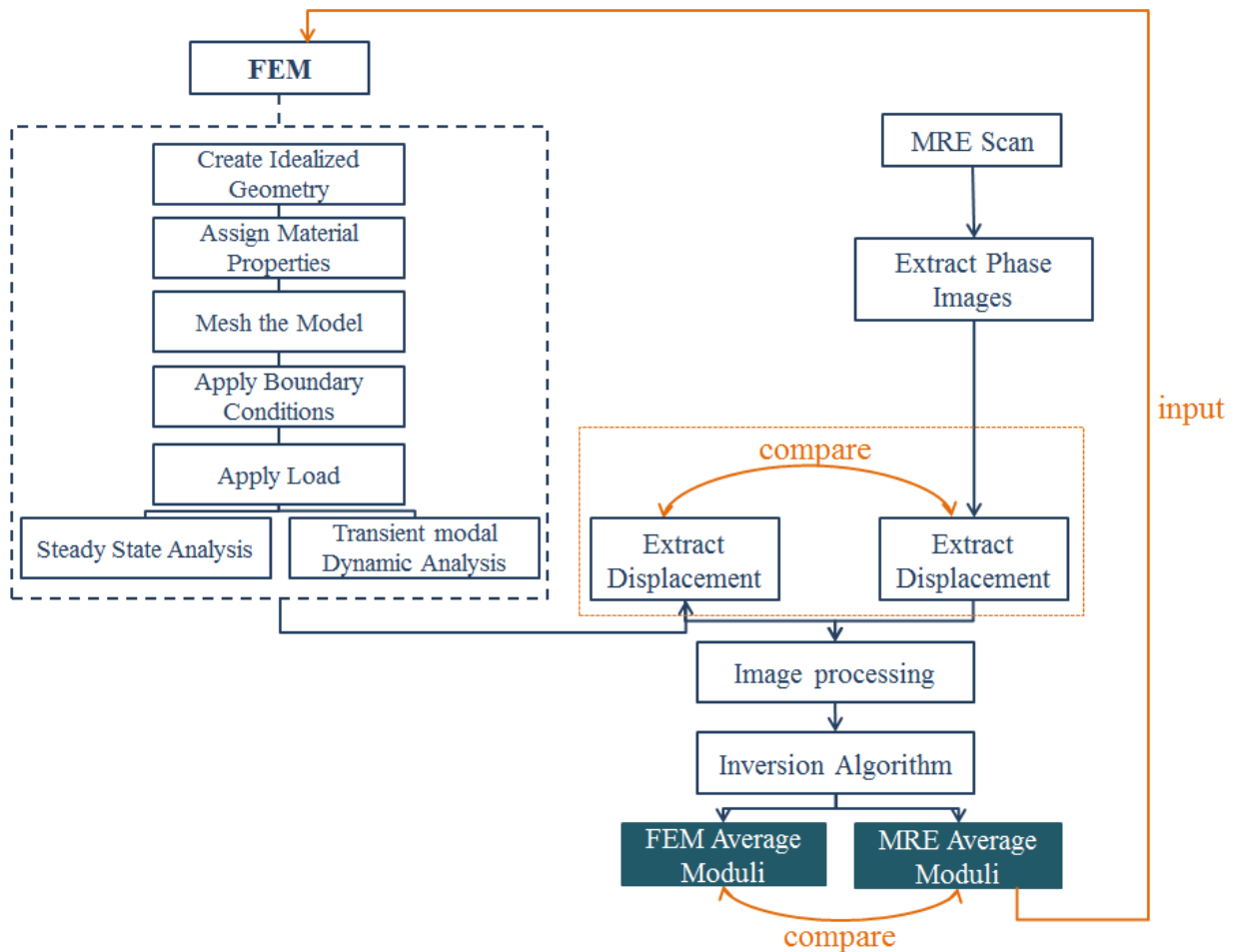


**Fig. 5.1** Schematic diagram of the process of MRE validation using FEMs: Images created with FE modeling mimicking MRE images are introduced in the inversion algorithm and the resulting shear modulus is compared with the shear modulus obtained for comparable images obtained experimentally with MRE. The values must be the same or very similar.

**Chapter 5 – Conclusion and Final Remarks**

In conclusion, before MRE can become a reliable diagnostic technique, a large number of improvements and tests must be performed, and a systematic investigation of all the parameters that influence the MRE results must be carried out to overcome the current limitations of the technique. Recent progress in MRE, including the specific contribution of the current project, suggests that the ultimate goal of translating MRE into clinical practice as a robust, useful and generally accepted tool is within reach.





## References

- [1] R. Muthupillai, P. J. Rossman, D. J. Lomas, J. F. Greenleaf, S. J. Riederer and R. L. Ehman, "Magnetic Resonance Imaging of Transverse Acoustic Strain Waves," vol. 36, pp. 266 - 274, 18 February 1996.
- [2] J. Braun, G. Buntkowsky, J. Bernarding, T. Tolxdorff and I. Sack, "Simulation and analysis of magnetic resonance elastography wave images using coupled harmonic oscillators and Gaussian local frequency estimation," *Magnetic Resonance Imaging*, vol. 19, pp. 703-713, 8 April 2001.
- [3] Y. C. Fung, *Biomechanics: Mechanical Properties of Living Tissues*, New York USA: Springer, 1993.
- [4] D. Klatt, C. Friedrich, Y. Korth, R. Vogt, J. Braun and I. Sack, "Viscoelastic properties of liver measured by oscillatory rheometry and multifrequency magnetic resonance elastography," *Biorheology*, vol. 47, pp. 133-41, 25 January 2010.
- [5] K. J. Parker, L. Gao, R. M. Lerner and S. F. Levinson, "Techniques for Elastic Imaging: A review," *IEE Engineering in Medicine and Biology*, pp. 52-59, November/December 1996.
- [6] L. Huwart and B. E. van Beers, "MR elastography," *Gastroentérol Clin Bio*, vol. 32, pp. 68-72, 21 May 2008.
- [7] A. S. Khalil, R. C. Chan, A. H. Chau and M. R. Mofrad, "Tissue elasticity estimation with optical coherence elastography: toward mechanical characterization of in vivo soft tissue," *Ann Biomed Eng*, vol. 33, pp. 1631-9, November 2005.
- [8] R. Muthupillai, D. J. Lomas, P. J. Rossman, J. F. Greenleaf, A. Manduca and R. L. Ehman, "Magnetic Resonance Elastography by Direct Visualization of Propagating Acoustic Strain Waves," *Science*, vol. 269, pp. 1854 - 1857, 29 September 1995.
- [9] M. Doyley and J. Weaver, "Magnetic Resonance Elastography: Experimental Validation and Performance Optimization".
- [10] A. Manduca, T. E. Oliphant, M. A. Dresner, J. L. Mahowald, S. A. Kruse, E.

## References

- Amromin, J. P. Felmlee, J. F. Greeleaf and R. L. Ehman, "Magnetic resonance elastography: Non-invasive mapping of tissue elasticity," *Medical Image Analysis*, vol. 5, pp. 237-254, 2000.
- [11] M. Doyley, "Model-based elastography: a survey of approaches to the inverse elasticity problem," *Physics in Medicine and Biology*, vol. 57, pp. 35-73, 1 August 2012.
- [12] Z. T. H. Tse, H. Janssen, A. Hamed, M. Ristic, I. Young and M. Lamperth, "Magnetic resonance elastograph hardware design: a survey," *Journal of Engineering in Medicine*, vol. 223, pp. 497 - 514, 5 January 2009.
- [13] R. M. Lerner, S. R. Huang and K. J. Parker, "Sonoelasticity" images derived from ultrasound signals in mechanically vibrated tissues," *Ultrasound in Medicine and Biology*, vol. 16, pp. 231-239, 1989.
- [14] C. J. Lewa and J. D. de Certaines , "MR Imaging of Viscoelastic Properties.," *Magnetic Resonance Imaging*, vol. 5, pp. 242 - 244, 1995.
- [15] E. Park and A. M. Maniatty, "Shear Modulus Reconstruction in Dynamic Elastography: Time Harmonic Case," *Physics in Medicine and Biology*, vol. 51, p. 3697-3721, 2006.
- [16] A. P. Sarvazyan, "A New approach to Remote Ultrasonic Evaluation of Viscoelastic Properties of Tissues for Diagnostics and Healing Monitoring," in *22nd International Symposium on: Ultrasonic Imaging and Tissue Characterization*, Landsdowne, Virginia, 1995.
- [17] P. McCracken, A. Manduca, J. P. Felmlee and R. L. Ehman, "Transient MR Elastography: Modeling Traumatic Brain Injury," in *Medical Image Computing and Computer-Assisted Intervention*, 2004.
- [18] R. Souchon , R. Salomir , O. Beuf , L. Milot , D. Grenier , D. Lyonnet , J. Y. Chapelon and O. Rouviere , "Transient MR Elastography (t-MRE) using Ultrasound Radiation Force: Theory, Safety, and Initial Experiments in Vitro," *Magnetic Resonance in Medicine*, vol. 60, pp. 871 - 881, 2008.

## References

- [19] A. Kolipaka, K. P. McGee, A. Manduca, . N. Anavekar, R. L. Ehman and P. A. Araoz, “In vivo Assessment of MR Elastography-Derived Effective End-Diastolic Myocardial Stiffness under Different Loading Conditions,” *Magnetic Resonance Imaging*, vol. 33, pp. 1224 - 1228, 1 May 2012.
- [20] S. A. Kruse, G. H. Rose, K. J. Glaser, A. Manduca, J. P. Felmlee, C. R. Jack Jr. and R. L. Ehman, “Magnetic Resonance Elastography of the Brain,” *neuroimage*, vol. 39, pp. 231 - 237, 10 August 2007.
- [21] I. Sack , J. Rump , T. Elgeti , A. Samani and J. Braun , “MR elastography of the human heart: noninvasive assessment of myocardial elasticity changes by shear wave amplitude variations.,” *Magnetic Resonance in Medicine*, vol. 61, pp. 668 - 677, March 2009.
- [22] M. Haghpanahi and H. A. Naeeni, “Investigation of Viscoelastic Properties of Human Liver Tissue Using MR Elastography and FE Modeling,” in *Iranian Conference of Biomedical Engineering*, Tehran, Iran, 2010.
- [23] L. Huwart, C. Sempoux, N. Salameh, J. Jamart, L. Annet, R. Sinkus, F. Peeters, L. C. t. Beek, Y. Horsmans and B. E. V. Beers, “Liver Fibrosis: Noninvasive Assessment with MR Elastography versus Aspartate Aminotransferase to-Platelet Ratio Index,” *Gastrointestinal Imaging*, vol. 245, pp. 458 - 466, 3 April 2007.
- [24] C. Lee , J. F. Glockner , K. J. Glaser , . M. Yin and J. M. Gloor , “MR elastography in renal transplant patients and correlation with renal allograft biopsy: a feasibility study.,” *Acad. Radiology*, vol. 19, pp. 834 - 841, July 2012.
- [25] M. A. Dresner, G. H. Rose , P. J. Rossman , R. Muthupillai , A. Manduca and R. L. Ehman , “Magnetic Resonance Elastography of Skeletal Muscle.,” *Magnetic Resonance Imaging*, vol. 13, no. 12, pp. 269 - 276, 2001.
- [26] S. Timoshenko and J. N. Goodier, *Theory of Elasticity*, McGraw-Hill, Ed., New York: Engineering Societies Monographs, 1951.
- [27] F. J. Lockett, *Nonlinear Viscoelastic Solids*, Academic Press, 1972.
- [28] R. A. Schapery, “A Method of Viscoelastic Stress Analysis Using Elastic Solutions,”

## References

- Journal of the Franklin Institute*, vol. 279, pp. 268 - 289, 1965.
- [29] W. T. Read, "Stress Analysis for Compressive Viscoelastic Materials," *Journal of Applied Physics*, vol. 21, 1950.
- [30] T. Oida , A. Amano and T. Matsuda, "Magnetic Resonance Elastography: in vivo Measurements of Elasticity for Human Tissue," in *12th International Conference on Informatics Research for Development of Knowledge Society Infrastructure*, Kyoto, 2004.
- [31] H. Schiessel, R. Metzler, A. Blumen and T. F. Nonnenmacher, "Generalized Viscoelastic models: their fractionalequations with solutions," *Journal of Physics A: Math*, vol. 28, pp. 6567-6584, 10 October 2011.
- [32] R. Muthupillai and R. L. Ehman, "Magnetic Resonance Elastography," *Nature*, vol. 2, 5 May 1996.
- [33] I. Sack, B. Beierbach, U. Hamhaber and D. Klatt, "Non-invasive measurement of brain viscoelasticity using magnetic resonance elastography," *NMR in Biomedicine*, pp. 37-41, 2007.
- [34] J. . A. Talwalkar, M. Yin, J. L. Fidler, S. O. Sanderson, P. S. Kamath and R. L. Ehman, "Magnetic Resonance Imaging of Hepatic Fibrosis:Emerging Clinical Applications," *Hepatology*, vol. 47, pp. 332 - 342, 8 August 2007.
- [35] D. Klatt, U. Hamhaber, P. Asbach, J. Braun and I. Sack, "Noninvasive assessment of the rheological behavior of human organs using multifrequency MR elastography: a study of brain and liver viscoelasticity," *Physics in Medicine and Biology*, vol. 52, pp. 7281-7294, 2007.
- [36] P. Asbach, D. Klatt, U. Hamhaber, J. Braun, R. Somasundaram, B. Hamm and I. Sack, "Assessment of Liver Viscoelasticity Using Multifrequency MR Elastography," *Magnetic Resonance in Medicine*, vol. 60, pp. 373 - 379, 22 January 2008.
- [37] C. J. Lewa, M. Roth, L. Nicol, J. M. Franconi and J. D. Certaines, "A new fast and unsynchronized method for MRI of Viscoelastic Properties of SoftTissues,"

## References

- Magnetic Resonance Imaging*, vol. 12, pp. 784 - 789, 2000.
- [38] J. Bishop, A. Samani, J. Sciarretta and D. B. Plewes, "Two-dimensional MR Elastography with Linear Inversion Reconstruction: Methodology and Noise Analysis," *Physics in Medicine and Biology*, vol. 45, no. 8, pp. 2081 - 2091, 2000.
- [39] D. Plewes, C. Luginbuhl, C. Macgowan and I. Sack, "An Inductive Method to Measure Mechanical Excitation Spectra for MRI Elastography," *Magnetic Resonance Engineering*, vol. 21, pp. 32 - 39, 28 September 2003.
- [40] J. Braun, K. Braun and I. Sack, "Electromagnetic Actuator for Generating Variably Oriented Shear Waves in MR Elastography," *Magnetic Resonance in Medicine*, vol. 50, pp. 220 - 222, 14 February 2003.
- [41] K. Uffman and M. E. Ladd, "Actuation Systems for MR Elastography: Design and Applications," *IEEE Engineering in Medicine and Biology Magazine*, May/June 2008.
- [42] K. Uffmann, C. Abicht, W. Grote, H. H. Quick and M. E. LADD, "Design of an MR-Compatible Piezoelectric Actuator for MR Elastography," *Magnetic Resonance Engineering*, vol. 15 (4), pp. 239 - 254, 11 September 2002.
- [43] M. M. Doyley, J. B. Weaver, E. W. Van Houten, F. E. Kennedy and K. D. Paulsen, "Thresholds for Detecting and Characterizing Focal Lesions Using Steady-state MR Elastography," *Med. Physics*, vol. 30, no. 4, pp. 495 - 504, 2003.
- [44] M. A. Bernstein, K. F. King and X. J. Zhou, *Handbook of MRI Pulse Sequences*, Rochester: Elsevier, 2004.
- [45] S. Hirsch, "Documentation of the MREEPI Sequence," Berlin, 2012.
- [46] L. Ying, Z.-P. Liang, D. C. Munson, R. Koetter and B. J. Frey, "Unwrapping of MR Phase Images Using a Markov Random Field Model," *IEEE Transactions on Medical Imaging*, vol. 25, pp. 128 - 136, January 2006.
- [47] T. J. Flynn, "Phase Unwrapping Using Discontinuity Optimization," *IEEE*, no. 0-7803-4403-0, pp. 80 - 82, 1998.

## References

- [48] A. Manduca, D. S. Lake, S. A. Kruse and R. L. Ehman, "Spatio-temporal Directional Filtering for Improved Inversion of MR Elastography Images," *Medical Image Analysis*, vol. 7, pp. 465 - 473, 2003.
- [49] T. E. Oliphant, A. Manduca, R. L. Ehman and J. F. Greenleaf, "Complex-Valued Stiffness Reconstruction for Magnetic Resonance Elastography by Algebraic Inversion of the Differential Equation," *Magnetic Resonance in Medicine*, vol. 45, p. 299–310, 11 September 2000.
- [50] S. Papazoglou, U. Hamhaber, J. Braun and I. Sack, "Algebraic Helmholtz Inversion in Planar Magnetic Resonance Elastography," *Physics in Medicine and Biology*, vol. 53, p. 3147–3158, 2008.
- [51] Q. Chen, S. I. Ringleb, A. Manduca, R. L. Ehman and K.-N. An, "A Finite Element Model for Analyzing Shear Wave Propagation Observed in Magnetic Resonance Elastography," *Journal of Biomechanics*, vol. 38, pp. 2198 - 2103, 24 September 2004.
- [52] E. E. V. Houten, M. I. Miga, J. B. Weaver, F. E. Kennedy and K. D. Paulsen, "Three-Dimensional Subzone-Based Reconstruction Algorithm for MR Elastography," *Magnetic Resonance in Medicine*, vol. 45, pp. 827 - 837, 16 November 2000.
- [53] H. A. Naeeni and M. Haghpanahi, "Viscoelastic Modeling of Brain MRE Data Using FE Method," *World Academy of Science, Engineering and Technology*, vol. 54, pp. 726-29, 2009.
- [54] K. J. Glaser, A. Manduca and R. L. Ehman, "Review of MR Elastography Applications and Recent Developments," *Journal of Magnetic Resonance Imaging*, vol. 36, no. 4, pp. 757 -774, 2012.
- [55] Y. K. Mariappan, K. J. Glaser and R. L. Ehman, "Magnetic Resonance Elastography: a Review," *Clinical Anatomy*, vol. 23, pp. 497 - 511, 2010.
- [56] D. Klatt, P. Asbach, J. Rump, S. Papazoglou, R. Somasundaram, J. Modrow, J. Braun and I. Sack, "In Vivo Determination of Hepatic Stiffness Using Steady-State Free Precession Magnetic Resonance Elastography," *Investigative Radiology*, vol. 41

## References

- , pp. 841 - 848, 12 December 2006.
- [57] M. Yin, J. Chen, K. J. Glaser, J. A. Talwalkar and R. L. Ehman, “Abdominal Magnetic Resonance Elastography,” *Magnetic Resonance Imaging*, vol. 20, pp. 79 - 87, 2009.
- [58] M. Yin, J. Chen, K. J. Glaser, J. A. Talwalkar and R. L. Ehman, “Abdominal MR Elastography,” *Top Magnetic Resonance Imaging*, vol. 20 , pp. 79 - 87, 31 March 2011.
- [59] J. A. Talwalkar, M. Yin, S. Venkatesh, P. J. Rossman, R. C. Grimm, A. Manduca, A. Romano, P. S. Kamath and R. L. Ehman, “Feasibility of in vivo MR Elastographic Splenic Stiffness Measurements in the Assessment of Portal Hypertension,” *Roentgenol*, vol. 193, pp. 122 - 127, 2009.
- [60] F. B. Freimann, K. J. Streitberger and D. Klatt, “Alteration of Brain Viscoelasticity after Shunt Treatment in Normal Pressure Hydrocephalus.,” *Neuroradiology*, 2011.
- [61] J. Wuerfel, P. Friedemann, B. Beierbach, U. Hamhaber, D. Klatt, S. Papazoglou, F. Zipp, P. Martus, J. Braun and I. Sack, “MR-elastography Reveals Degradation of Tissue Integrity in Multiple Sclerosis,” *Neuroimage*, vol. 49, pp. 2520 - 2525, 2010.
- [62] K. J. Streitberger, E. Wiener and J. Hoffmann, “In Vivo Viscoelastic Properties of the Brain in Normal Pressure Hydrocephalus,” *NMR*, vol. 24, pp. 385 - 392, 2011.
- [63] I. Sack, B. Beierbach, U. Hamhaber, D. Klatt, P. Martus, S. Papazoglou and J. Braun, “The impact of aging of aging and gender on brain viscoelasticity,” *Neuroimaging*, vol. 46, pp. 652 - 657, 2009.
- [64] T. Elgeti, . M. Laule, N. Kaufels, . J. Schnorr, . B. Hamm, A. Samani, . J. Braun and I. Sack, “Cardiac MR Elastography: Comparison with left ventricular pressure measurement,” *Journal of Cardiovascular Magnetic Resonance*, vol. 11, no. 1, 2009.
- [65] I. Sack, J. Bernarding and J. Braun, “Analysis of wave patterns in MR elastography of skeletal muscle using,” *Magnetic Resonance Imaging*, vol. 20, pp. 95 - 104, 2002.
- [66] CGC Instruments, *Programmable Digital Waveform Generator for High-Voltage Power Amplifiers*, CGC Instruments, 2011.

## References

- [67] CGC Instruments, “High-Voltage Amplifier with Programmable Digital Waveform Generator for Driving Piezo Actors,” CGC Instruments, Hübschmannstr.
- [68] R. L. Ehman, P. J. Rossman, T. C. Hulshizer and M. A. Dresner, “Pressure Activated Driver for Magnetic Resonance Elastography”. US Patent US 7,034,534 B2, 25 April 2006.
- [69] R. L. Ehman and P. J. Rossman, “Active Acoustic Driver for Magnetic Resonance Elastography”. US Patent US 2010/0005892 A1, 14 January 2010.
- [70] L. Mannelli, E. Godfrey , M. J. Graves , A. J. Patterson , P. Beddy , D. Bowden , I. Joubert , A. N. Priest and D. J. Lomas , “Magnetic resonance elastography: feasibility of liver stiffness measurements in healthy volunteers at 3T.,” *Clinical Radiology*, vol. 67, pp. 258 - 262, 2012.
- [71] L. Mannelli , . E. Godfrey, . I. Joubert, A. J. Patterson , M. J. Graves , F. A. Gallagher and D. J. Lomas , “MR elastography: Spleen stiffness measurements in healthy volunteers--preliminary experience.,” *AJR Am J Roentgenol*, vol. 195, pp. 387 - 392, 2010.
- [72] P. Latta, M. L. Gruwel, P. Debergue, B. Matwi, U. N. Sbotto-Frankensteen and B. Tomanek, “Convertible Pneumatic Actuator for Magnetic Resonance Elastography of the Brain,” *Magnetic Resonance Imaging*, vol. 29, pp. 147 - 152, 13 July 2010.
- [73] R. C. Coffin, “Repairable electromagnetic linear motor for loudspeakers and the like”. US Patent 6778677, 17 August 2004.
- [74] C. Drive, “Co Drive Technology,” 11 December 2004. [Online]. Available: <http://www.codrive.com/tech.htm>. [Accessed 2 October 2012].
- [75] W.-H. Huang, W.-R. Cai, C.-z. Zeng, X. Liu, Y.-C. Chung, L.-J. Zhang and H.-R. Zheng, “MR Elastography Pneumatic Driver Design and its Function Evaluation,” in *International Conference on Biomedical Engineering and Informatics*, TBD Shanghai, China, 2011.
- [76] W. Cai, H. Wang, W. Huang, Y.-C. Chung, L. Zhang, C. Zou and H. Zheng, “Performance Evaluation of A Prototype Pneumatic Driver for MR Elastography by



## References

- MR Elastography,” in *International Conference on Biomedical Engineering and Informatics*, TBD Shanghai, China, 2011.
- [77] J. G. T. Ribeiro and J. T. P. d. Castro, “New Improvements in the Digital Double Integration Filtering Method to Measure Displacements using Accelerometers,” in *Society for Experimental Mechanics*, 2001.
- [78] J. G. T. Ribeiro and J. T. d. Castro, “Filtering in Frequency Domain to Avoid Time Aliasing,” in *Society for Experimental Mechanics*, Orlando, Florida, USA, 2002.
- [79] L. D. Slifka, “An Accelerometer Based Approach to Measuring Displacement of a Vehicle Body,” Dearborn, 2004.
- [80] J. G. T. Ribeiro and J. T. d. Castro, “Using the FFT - DDI Method to Measure Displacements with Piezoelectric, Resistive and ICP Accelerometers,” in *Society for Experimental Mechanics*, 2003.
- [81] J. G. T. Ribeiro, “Time Aliasing Induced Errors in Digital Double Integration,” in *IPEN*, 2000.
- [82] J. Braun, G. Buntkowsky, J. Bernarding, T. Tolxdorff and I. Sack, “Simulation and Analysis of Magnetic Resonance Elastography Wave Images Using Coupled Harmonic Oscillators and Gaussian Local Frequency Estimation,” *Magnetic Resonance Imaging*, vol. 19, pp. 703 - 713, 8 April 2001.
- [83] Q. Chen, S. Bensamoun, J. R. Basford, J. M. Thompson and K.-N. An, “Identification and Quantification of Myofascial Taut Bands with Magnetic Resonance Elastography,” *Physical Medicine and Rehabilitation*, vol. 88, pp. 1658 - 1660, 2007.
- [84] U. Hamhaber, F. A. Grieshaber, J. H. Nagel and U. Klose, “Comparison of Quantitative Shear Wave MR-Elastography With Mechanical Compression Tests,” *Magnetic Resonance in Medicine*, vol. 49, pp. 71 - 77, 5 August 2002.
- [85] Q. Chen, S. I. Ringleb, A. Manduca, R. L. Ehman and K.-N. An, “Differential Effects of Pre-Tension on Shear Wave Propagation in Elastic Media with Different Boundary Conditions as Measured by Magnetic Resonance Elastography and Finite

## References

- Element Modeling,” *Journal of Biomechanics*, vol. 39, pp. 1428 - 1434, 8 April 2005.
- [86] J. Sciarretta, J. Bishop, A. Samani and D. B. Plewes, “MR Validation of Soft Tissue Deformation as Modeled by Non Linear Finite Element Analysis,” in *ISMRM*, Ontario, Canada, 1999.
- [87] L. E. J. Thomas-Seale, D. Klatt, P. Pankaj, N. Roberts, N. Roberts , I. Sack and P. R. Hoskins, “A Simulation of the Magnetic Resonance Elastography Steady State Wave Response through Idealised Atherosclerotic Plaques,” *International Journal of Computer Science*, vol. 38, 2011.
- [88] L. E. J. Thomas-Seale, P. Pankaj, N. Roberts and P. R. Hoskins, “Computational Modelling of Magnetic Resonance Elastography Shear Wave Behaviour through Atherosclerotic Plaque with Disease Development,” in *World Congress on Engineering*, London, UK, 2011.
- [89] Q. Chen, S. I. Ringleb, T. Hulshizer and K.-N. An, “Identification of the Testing Parameters in High Frequency Dynamic Shear Measurement on Agarose Gels,” *Journal of Biomechanics*, vol. 38, pp. 259 - 263, 15 May 2004.
- [90] T. Kaster, I. Sack and A. Samani, “Measurement of the Hyperelastic Properties of Ex Vivo Brain Tissue Slices,” *Journal of Biomechanics*, vol. 44, pp. 1158 - 1163, 18 January 2011.
- [91] J. Vappou, E. Breton, P. Choquet, C. Goetz, R. Willinger and A. Constantinesco, “Magnetic Resonance Elastography Compared with Rotational Rheometry for in Vitro Brain Tissue Viscoelasticity Measurement,” in *ESMRMB*, Berlin, 2007.
- [92] P. V. Bayly , P. G. Massouros , E. Christoforou , A. Sabet and G. M. Genin , “Magnetic resonance measurement of transient shear wave propagation in a viscoelastic gel cylinder,” *Mechanical Phys. Solids*, vol. 56, pp. 2036 - 2049, 2008.
- [93] M. Hrapko , J. A. van Dommelen , G. W. Peters and J. S. Wismans , “Characterisation of the mechanical behaviour of brain tissue in compression and shear,” *Biorheology*, vol. 45, p. 663–676, 2008.

## References

- [94] R. J. Okamoto, E. H. Clayton and P. V. Bayly, “Viscoelastic Properties of Soft Gels: a Comparison of Magnetic Resonance Elastography and Dynamic Shear Testing in the Shear Wave Regime,” *Physics in Medicine and Biology*, vol. 56, pp. 6379 - 6400, 7 October 2011.
- [95] S. I. Ringleb, Q. Chen, A. Manduca, R. L. Ehman and K.-N. An, “Quantitative Shear Wave Magnetic Resonance Elastography: Comparison to a Dynamic Shear Material Test,” *Magnetic Resonance in Medicine*, vol. 53, pp. 1197 - 1201, May 2005.
- [96] E. L. Madsen , . G. R. Frank, M. A. Hobson , . S. Lin-Gibson, T. J. Hall and J. Jiang , “Instrument for determining the complex shear modulus of soft-tissue-like materials from 10 to 300 Hz,” *Physics in Medicine and Biology*, vol. 53, p. 5313–5342, 2008.
- [97] H. A. Barnes and J. M. Maia, “Rheometry,” in *Rheology - voll*, Cleveland, OH, Encyclopedia of Life Support Systems (EOLSS).



# **APPENDIX**



## APPENDIX

### APPENDIX A – PIEZOELECTRIC STACK SPECIFICATIONS

#### PICA Stack Piezo Actuators

HIGH FORCES, HIGH DISPLACEMENT, FLEXIBLE PRODUCTION



##### P-007 – P-056

- Travel ranges to 300  $\mu\text{m}$
- High load capacity
- Force generation up to 80 kN
- Extreme reliability:  $>10^8$  cycles
- Microsecond response
- Sub-nanometer resolution
- Large choice of designs

##### Stacked piezo linear actuator

Operating voltage 0 to 1000 V. Long lifetime without derating. High specific displacement. High forces. Operating temperature range -20 to 85°C

##### Available options

- SGS sensors for positional stability
- PZT ceramic material
- Operating voltage range, displacement, layer thickness
- Load capacity, force generation
- Geometric shapes: Round, rectangular
- Mechanical interfaces: Flat, spherical, metal, ceramic, glass, sapphire, etc.
- Integrated piezoelectric detector layers
- Special high / low temperature versions, temperature sensor
- Non-magnetic versions
- Extra-tight length tolerances

##### Fields of application

Research and industry. For high-load positioning, precision mechanics / -machining, switches



Custom actuator with special end piece and applied SGS sensors. The protective polymer layer can be dyed in different colors. Standard versions are delivered with stranded wires and are covered in black

##### Suitable drivers

E-464 PICA Piezo Driver  
E-481 PICA High-performance Piezo Driver / Controller  
E-470 • E-472 • E-421 PICA Controller

© Physik-Instrumente (PI) GmbH & Co. KG 2012. Subject to change without notice. Latest releases available at [www.pi.ws](http://www.pi.ws). 12/04/24.0

[WWW.PICERAMIC.COM](http://WWW.PICERAMIC.COM)

## APPENDIX

PI

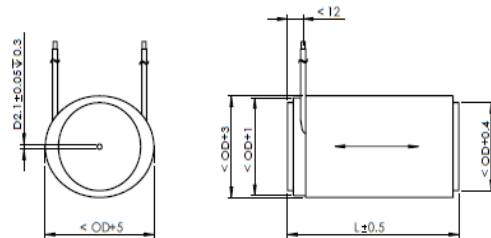
Order number	Displacement (0–1000 V) [μm] -10/+20%	Diameter OD [mm]	Length L [mm] ±0,5	Blocking force (0–1000 V) [N]	Stiffness [N/μm]	Capacitance [nF] ±20%	Resonant frequency [kHz]
P-007.00	5	7	8	650	130	11	126
P-007.10	15	7	17	850	59	33	59
P-007.20	30	7	29	1000	35	64	36
P-007.40	60	7	54	1150	19	130	20
P-010.00	5	10	8	1400	270	21	126
P-010.10	15	10	17	1800	120	64	59
P-010.20	30	10	30	2100	71	130	35
P-010.40	60	10	56	2200	38	260	20
P-010.80	120	10	107	2400	20	510	10
P-016.10	15	16	17	4600	320	180	59
P-016.20	30	16	29	5500	190	340	36
P-016.40	60	16	54	6000	100	680	20
P-016.80	120	16	101	6500	54	1300	11
P-016.90	180	16	150	6500	36	2000	7
P-025.10	15	25	18	11000	740	400	56
P-025.20	30	25	30	13000	440	820	35
P-025.40	60	25	53	15000	250	1700	21
P-025.80	120	25	101	16000	130	3400	11
P-025.90	180	25	149	16000	89	5100	7
P-025.150	250	25	204	16000	65	7100	5
P-025.200	300	25	244	16000	54	8500	5
P-035.10	15	35	20	20000	1300	700	51
P-035.20	30	35	32	24000	810	1600	33
P-035.40	60	35	57	28000	460	3300	19
P-035.80	120	35	104	30000	250	6700	11
P-035.90	180	35	153	31000	170	10000	7
P-045.20	30	45	33	39000	1300	2800	32
P-045.40	60	45	58	44000	740	5700	19
P-045.80	120	45	105	49000	410	11000	10
P-045.90	180	45	154	50000	280	17000	7
P-050.20	30	50	33	48000	1600	3400	32
P-050.40	60	50	58	55000	910	7000	19
P-050.80	120	50	105	60000	500	14000	10
P-050.90	180	50	154	61000	340	22000	7
P-056.20	30	56	33	60000	2000	4300	32
P-056.40	60	56	58	66000	1100	8900	19
P-056.80	120	56	105	76000	630	18000	10
P-056.90	180	56	154	78000	430	27000	7

Piezo ceramic type: PIC 151.  
Standard electrical interfaces:  
PTFE-insulated wire leads,  
100 mm, AWG 24 (Ø 1.15 mm).  
Recommended preload for  
dynamic operation: 15 MPa.

Maximum preload for constant force:  
30 MPa.  
Resonant frequency at  $1 V_{pp}$  unloaded,  
free on both sides. The value is halved  
for unilateral damping.  
Capacitance at  $1 V_{pp}$ , 1 kHz, RT.

Operating voltage: 0 to 1000 V.  
Operating temperature range: -20  
to 85°C.  
Standard mechanical interfaces: Steel  
plates, 0.5 to 2 mm thick (depends on  
model).

Outer surfaces: Polyolefin shrink  
sleeving, black. Custom designs  
or different specifications on  
request.



PICA Stack, dimensions in mm. L, OD see data table

PIEZOTECHNOLOGY



## APPENDIX

### APPENDIX B – COMMERCIAL ACCELEROMETER SPECIFICATIONS



#### STEVAL-MKI006V1

MEMS 3-axis -  $\pm 2g/\pm 8g$  digital output low power linear accelerometer evaluation board based on LIS302DL

Data Brief

#### Features

- Graphical user interface
- USB connector
- Control switches
- MEMS sensor
- LED indicators
- ST7-USB microcontroller

#### Description

The STEVAL-MKI006V1 is an evaluation kit designed to provide the user with a complete, ready-to-use platform for evaluation of the LIS302DL, a low power 3-axis linear accelerometer with digital output. The device includes a sensing element and an IC interface capable of translating information from the sensing element into a measured signal that can be used for external applications.

In addition to the MEMS sensor, the evaluation board utilizes an ST7-USB microcontroller which functions as a bridge between the sensor and the PC, on which it is possible to use the graphical user interface (GUI) included with the kit or dedicated software routines for customized applications.



STEVAL-MKI006V1

## 1 Board schematic

**Figure 1. Scheme**

